37

Performance Analysis of Subaperture Processing Using a Large Aperture Planar Towed Array

by

Jennifer Anne Watson

Submitted to the Department of Ocean Engineering/WHOI
Department of Applied Ocean Science and Engineering
in partial fulfillment of the requirements for the degree of

Doctor of Philosophy

at the

MASSACHUSETTS INSTITUTE OF TECHNOLOGY

February 2004

Author .....
Department of Ocean Engineering/WHOI Department of Applied Ocean Science and Engineering
December 3, 2003

Certified by.....
Arthur B. Baggeroer
Ford Professor of Electrical and Ocean Engineering, ONR/CNO Chair
Thesis Supervisor

Accepted by....
Mark Grosenbaugh
Chairman, Joint Committee for Applied Ocean Science and Engineering

Performance Analysis of Subaperture Processing Using a Large Aperture Planar Towed Array

by

Jennifer Anne Watson

Submitted to the Department of Ocean Engineering/WHOI Department of Applied Ocean Science and Engineering
on December 3, 2003, in partial fulfillment of the
requirements for the degree of
Doctor of Philosophy

Abstract

In recent years the focus of passive detection and localization of submarines has moved from the deep ocean into the littoral regions. The problem of passive detection in these regions is complicated by strong multipath propagation with high transmission loss. Large aperture planar arrays have the potential to improve detection performance due to their high resolution and high gain, but are suceptible to two main performance degradation mechanisms: limited spatial coherence of signals and nonstationarity of high bearing rate interference sources common in littoral regions of strategic importance. This thesis presents subarray processing as a method of improving passive detection performance using such large arrays.

This thesis develops statistical models for the detection performance of three adaptive, sample-covariance-based subarray processing algorithms which incorporate the effects of limited spatial coherence as well as finite snapshot support. The performance of the optimum processor conditioned on known data covariances is derived as well for comparison.

These models are then used to compare subarray algorithms and partitioning schemes in a variety of interference environments using plane wave and matched-field propagation models. The analysis shows a tradeoff between the required adaptive degrees of freedom, snapshot support, and adaptive resolution. This thesis shows that for both plane-wave and matched-field processing, the Conventional-Then-Adaptive (CTA) algorithm optimizes this tradeoff most efficiently.

Finally, a comparison of the CTA algorithm to beam-space adaptive processing shows that for moderate beam coverage, the subarray algorithm performs as well as or superior to the adaptive beamspace algorithm.

Thesis Supervisor: Arthur B. Baggeroer
Title: Ford Professor of Electrical and Ocean Engineering, ONR/CNO Chair

Acknowledgments

I would like to take this opportunity to thank the many people who have helped me along the path to this degree. First I would like to thank Lisa Zurk and Jim Ward for encouraging me to pursue this degree and for introducing me to the field of sonar signal processing. Your feedback and encouragement over the past five years has been invalueable. I thank the members of the Advanced Sensor Techniques Group at Lincoln Laboratory, especially Brian Tracey, Nigel Lee, Bill Payne and Steve Kogon. You have been my sounding boards as I worked through the details of this thesis research and helped me develop an appreciation for the challenges of data-driven passive sonar. You have been invalueable colleagues and great friends. I also thank Keith Forsythe and my defense coach Larry Horowitz for helping me with the preparation for my thesis defense. I sincerely appreciate your time and assistance. I also express my gratitude Lincoln Laboratory and the Lincoln Scholars Committee for funding this research.

I would like to thank the past and present members of the Ocean Acoustics Group at MIT. Especially Andrea Kraay, Peter Daly, Wen Xu, Josh Wilson, Joe Edwards, Yi-san Lai, Michele Zanolin, and Irena Viljovic. Your friendship has helped make my time at MIT a positive experience.

I am deeply grateful for the guidance of my committee members, Prof. Henrik Schmidt, Dr. James Preisig, and Dr. Christ Richmond. Jim, you have lent a fresh perspective on this research, and your thoughtful questions and suggestions have certainly improved the quality of this thesis. Christ, I sincerely thank you for taking the time to work through the statistical analysis with me. Your patience and consideration is greatly appreciated.

I would like to express gratitude to my advisor Prof. Baggeroer for his patience and guidance over the course of this endeavor. You have continually challenged me, you have taught me, and through your understanding and example, you have helped me to maintain a healthy perspective thoughout this journey. I am grateful.

I thank my family and friends for their encouragement along the way. I extend my

deepest thanks to my parents John and Gail Munro and my brother John. Mom and Dadd, your encouragement throughout my entire life has made me who I am today. You have always believed in me, and you have always challenged me to be the best I can be. I thank you both and I love you always.

Finally, I cannot adequately express my thanks and appreciation to my husband, Michael, and my son, Joseph. Mike, you have been such a source of strength for me. I am eternally grateful for your pep talks, for your patience, and for your understanding. And most of all for believing I could do this even when I doubted myself. I thank you most sincerely. And Joey, you gave me the motivation to get down the home stretch. I love you both with all my heart. Thank you.

This work was sponsored by the Air Force under Air Force Contract F19628-00-C-0002. Opinions, interpretations, conclusions, and recommendations are those of the authors and are not necessarily endorsed by theUnited States Government.

To Michael and Joey

Contents

List of Figures

List of Tables

Chapter 1

Introduction

In recent years the focus of passive detection and localization of submarines has moved from deep waters to littoral regions. The strategic importance of coastal areas has increased the operational significance of very quiet submarines which emit signatures far lower than those of merchant surface ships. The challenging propagation environment presented by coastal regions coupled with the high density of merchant ship interference create a challenge to the passive detection problem. This thesis examines subaperture processing applied to large aperture arrays as a method of improving detection performance in high-interference, shallow water environments with coherence and snapshot limitations. This chapter begins with the motivation for large aperture arrays and subaperture processing in section 1.1. It then presents the goals and contributions of this thesis in section 1.2 . This chapter concludes with an outline of the remaining chapters in section 1.3.

1.1 Motivation

Passive detection in littoral regions is more challenging than in the traditional deep-water operational environments for two main reasons. First, the acoustic propagation environment in coastal regions (water depths 100-400m) leads to more complex propagation and higher transmission loss than in deep water (1000+m water depths). Second, coastal regions of interest contain high densities of passenger, merchant, and

fishing vessels. This clutter creates a non-stationary, high interference environment, impeding the detection of quiet submerged targets.

Shallow water propagation environments are characterized by "downward-refracting" sound speed profiles in which the speed of propagation for a sound wave is slowest near the sea floor, causing sound waves to refract toward the bottom. This results in two phenomena. First, the propagating acoustic wave will lose energy selectively into the sea floor with each reflection, resulting in high transmission loss between the source and receiver. Second, since the bottom is not smooth, the reflections result in coherent and incoherent multipath propagation. This propagation is further complicated by unpredictable variability in the water column which ultimately leads to signal decorrelation.

The second challenge to passive detection in littoral regions is the high density of merchant ships. These merchant ships are generally much louder than submerged targets of interest, with average radiated source levels of merchant ships exceeding those of WWII-era submarines by 15-25 dB re $\mu Pa/Hz$ [1]. These ships prevent detection of quiet targets through both main-lobe and sidelobe jamming.

One method for overcoming these environmental and interference-related challenges to passive detection is the use of large aperture arrays coupled with interference rejection techniques known as adaptive algorithms. Large apertures have the potential for high resolution, reducing the likelihood that a target and interference source occupy the same resolution cell. The large number of sensors provides high gain and high levels of adaptivity which help mitigate the effects of transmission loss and jamming respectively. Though large aperture arrays hold the potential for performance improvement, they come with their own challenges. First, the costs associated with developing such an architecture are immense. There is, however, a similar technology which has been developed commercially whose architecture may meet the needs of the passive sonar community.

The seismic community has developed large aperture, multi-line planar towed arrays for use in oil exploration. These arrays are currently used as the receiving array for active seismic systems searching for oil deposits beneath the sea floor. This array

architecture, also has the potential for improving passive detection and localization for anti-submarine warfare (ASW). These arrays are designed to be much larger than any USN system, upward of 20 km long, and span a width of up to 1km, containing thousands of sensors. They are also designed to be towed at depths of 10m-100m. Such a large aperture provides a potential for a projected vertical aperture which is beneficial to resolving acoustic targets in both range and depth using a technique known as Matched Field Processing (MFP). Finally, these arrays are designed to operate at frequencies below 100 Hz, the band in which many submarine signatures lie.

There are, however, two main obstacles, aside from development costs, to processing large aperture arrays. The first is the fact that the ocean waveguide propagation environment contains phenomena such as internal waves and volume inhomogeneities which lead to spatial decorrelation of a signal in the waveguide [2], [3], and [4]. Therefore, targets and/or interference signals may not be coherent across the full array aperture, thus limiting resolution and coherent gain of an array. Experimental measurements estimate that sources in shallow water have spatial coherence lengths on the order of 20-40 wavelengths [4], [5], much smaller than the seismic array's aperture.

The second challenge to passive detection using large arrays comes from the fact that propagation environments are inherently non-stationary. Since large arrays have small resolution cells, interfering surface ships may transit several resolution cells during an observation period. This becomes a major challenge to adaptive processing known as "snapshot deficiency". The adaptive algorithms of interest to this thesis, as will be detailed in Chapters 3 and 4, rely on forming an adaptive weight vector which is a function of the inverse of the ensemble covariance matrix. In practice, this matrix is unknown, and must be estimated from snapshots of the data. This estimation requires at least as many independent snapshots of data as sensors in the array for the estimated covariance matrix to be full rank, and hence its inverse to exist. Further, in order to reduce the performance degradation associated with poor estimation, it is necessary to use 2-3 times the number of snapshots as dimension of the matrix to be inverted [6], [7]. It is implicitly assumed in the algorithms that the

data is stationary over this observation period. Therefore, the more snapshots needed, the longer the required observation period. In practice, interference environments will not remain stationary over sufficient observation intervals.

While large aperture arrays can be beneficial to passive detection in the littoral region, limited spatial coherence and finite snapshot support pose new challenges. This thesis studies the technique known as subaperture processing as a method to overcome these two challenges particular to large arrays. By breaking the array into pieces which are, themselves, more tolerant to degradation mechanisms, one may achieve improved detection performance. Arrays may be partitioned into sections over which signals are spatially coherent, helping to mitigate coherence issues. Also, adaptive processing may be applied within subarrays or across beamformed subarray outputs, reducing the rank of the estimated covariance matrix to the number of sensors in a subarray or the number of subarrays respectively, and hence reducing the required snapshot support.

Subaperture processing has appeared in the literature in the context of both seismic arrays [8], radar systems, and acoustic arrays [9], [10], [11], and [12] among others. Cox [9] proposed subarray processing as a vehicle to approximate computationally intrusive matched field processing using plane wave models. Lee [10] examined subarray processing as a method of reducing the rank, therefore requisite snapshot support, of adaptive algorithms. While subarray processing has been used extensively, there has been no statistical detection performance analysis of such processors. Further, there has been no comprehensive study of the effects of limited spatial coherence and snapshot support on detection performance. The contribution of this thesis, as detailed in the following section, fills this gap.

1.2 Goals of Thesis

This thesis research conducts a performance analysis of the statistical detection performance of subaperture processing of large aperture planar towed arrays for quiet target detection. Large aperture arrays as well as large aperture subarray processing

has been studied in the past in geo-physical and land-based seismic systems. The geophysical community has used large arrays of geophones or seismometers to detect events such as earthquakes, for example. Acoustic arrays have also been used to detect nuclear detonations as part of systems to detect violations of nuclear test ban treaties [13], [14]. Subaperture processing of these acoustic arrays was studied as well. As recently as 1998, subaperture processing schemes have been applied to these land-based, stationary geophysical arrays [15]. Water-based acoustic systems of hydrophones have also been used as part of active sonar systems for geophysical exploration, the application of seismic planar hydrophone arrays to passive detection and localization of sources in the water column is largely unexplored. Planar towed arrays of extremely limited extent have been applied to the problem of passive detection and localization in a few cases, but large apertures have not been studied extensively in this context. Large arrays have been alluded to in simulations in many publications [4], [16], and [17] for example, but even in those cases the arrays were linear and of less than 150 sensors, and often designed for frequencies above 100 Hz. This thesis details the passive detection performance of large aperture planar towed arrays using subarray algorithms. It focuses on the following issues:

1. Performance improvement of subaperture algorithms vis a vis full-array conventional and MVDR processing
2. Subaperture structure vs. snapshot support
3. Subaperture structure vs. target and interference coherence
4. Trade-off between the required adaptive resolution and required snapshot support.

A number of issues arise which are particular to large aperture arrays. The intended application of such detection is in littoral environments, in which discrete interference tends to be the dominant noise source. As such, three issues come to the forefront. First, signals tend to decorrelate spatially in the littoral environment. The scale of the decorrelation may differ for nearby sources of interest and interference.

Second, as these interference and sources of interest may be at relatively close range, they tend to be high bearing-rate targets. As such, stationarity becomes a second dominant factor. Finally, sources of interest often lie in the near field of these large apertures. This results in significant curvature of the wavefront across the array which is not well-modeled by a plane wave.

This thesis first develops a statistical model for the detection performance of several subarray processing algorithms using the power estimate as the detection statistic in a likelihood-ratio-test (LRT) formulation. This requires a derivation of the *pdf* of the power estimates from each of the subarray algorithms. The model developed in this thesis accounts for the performance degradations of poor snapshot support and limited spatial coherence. This model is then applied to several examples ranging from very simple cases of plane wave processing a linear array to matched field processing of a planar towed array. Through this, analytical guidelines for array partitioning and processing algorithms in the challenging littoral environment are derived.

There are three adaptive subarray processing algorithms analyzed in this thesis. These three algorithms are two stage processing algorithms in which one type of beamforming is applied within a subarray and a second is used to combine subarrays to form a power estimate. Since this power estimate is used in a likelihood-ratio test to determine detection performance, the *pdf* of each subarray power estimation algorithm is needed.

The first algorithm is the conventional-then-adaptive (CTA) algorithm in which conventional beamforming is used within each subarray and then the subarray outputs are combined adaptively to form a power estimate [8], [9]. The statistics of this algorithm are straightforward to derive in a coherent signal environment, but have not appeared in the literature, and are subsequently generalized to account for the snapshot and coherence issues.

The second algorithm is the adaptive-incoherent (AI) algorithm. In this algorithm, adaptive beamforming is applied to each subarray and their individual power estimates are combined incoherently. The challenge to the statistical analysis of this

algorithm is that the power estimates are inherently correlated. An effective degree-of-freedom approach is taken and results in a valid statistical model for the range of problems of interest to this thesis.

Finally, the statistics of the adaptive-then-conventional (ATC) algorithm are derived. In this algorithm, each subarray is beamformed adaptively and the subarray beam outputs are combined conventionally. The statistics of this algorithm are derived analytically and, ultimately through approximation, the first and second moments of the power estimate, and then invoke a central-limit-theorem argument to derive the statistics of the resulting power estimate.

Once the statistics are derived, the CFAR detection performance as a function of subarray configuration is compared to the fully-coherent conventional (non-adaptive) processor as well as the optimum, clairvoyant processor in which it is assumed that the ensemble covariance matrix is known and not estimated from the data. The three algorithms are compared in terms of their detection performance in both plane-wave and MFP examples.

This work leverages off of previous work in statistical array processing, particularly the work of Capon and Goodman [7], Kelly and Forsythe [18], Steinhardt [19], and Richmond [20]. This thesis extends their analysis to the problem of subarray processing in a coherence-limited, snapshot starved environment. The performance of these algorithms as a function of subarray partitions are examined analytically and through simulations for a variety of propagation and interference environments. The organization of this thesis is presented in the following section.

1.3 Thesis Organization

This thesis is broken into six chapters, the first being this introduction. Chapter 2 provides a description of the seismic arrays used in this thesis, as well as a discussion of array resolution in the context of three propagation models. It begins with a description of the seismic exploration arrays used as the array model for this thesis. This is followed by a description of the plane wave, wavefront-curvature, and normal

mode propagation models. Array resolution is examined in the context of each model. Finally, a model for signal coherence is presented as well as motivation for adaptive processing.

Chapter three presents adaptive and subarray processing algorithms. It begins with a brief survey of the history of adaptive processing and its influence on the passive sonar problem. An overview of full-array adaptive techniques is included. The chapter continues with a discussion of the major challenges to adaptive processing and a presentation of several *ad hoc* algorithms developed to handle these challenges. The chapter concludes with a description of adaptive subarray algorithms examined in this thesis. They form the basis for the statistical analysis to follow.

Chapter 4 develops a statistical analysis of adaptive subarray processing. It begins with a survey of previous work in statistics of array processing algorithms, particularly the work of Capon and Goodman [7], Kelly [18], Steinhardt [6], and Richmond [20]. The new results presented in this thesis leverage off of this previous work. Also included is a presentation of the standard binary detection problem in a likelihood ratio formulation. This chapter then presents a statistical model for the detection performance of the optimum processor using the ensemble covariance matrix. A model for the *pdf* of the power estimate formed from each subarray algorithm is then derived. These statistical models are all validated via simulations.

Chapter 5 uses the statistical model developed in Chapter 4 to examine the effects of coherence and snapshot support on the detection performance of adaptive subarray algorithms. First the separate effects of target and interferer coherence are presented using a single line array with a plane wave propagation model. These effects are studied in the context of all three adaptive subarray algorithms with a single target and single interferer, and subarray partitioning strategy is examined. Section 5.2 then applies the analysis of Chapter 4 to an interference-dominated environment, again using a plane wave propagation model. This leads to insight into the trade-off between resolution and adaptivity, and several conclusions regarding subarray algorithm selection. Section 5.3 examines algorithm performance and array design for MFP using both linear and planar arrays. Finally the performance of adaptive

subarray processing is compared to adaptive beamspace processing, a commonly used algorithm in practice. It is shown that in a high interference environment with a fixed snapshot support, an optimal subarray configuration out-performs even a 7-beam algorithm.

This thesis concludes with a summary in Chapter 6. The contributions of this thesis, the derivation of *pdfs* for subarray processing algorithms, and the relationship between array coherence and optimum subarray partitions and snapshot support are recapped. A range of areas for future work is also provided.

Chapter 2

Large Aperture Arrays and Spatial Resolution

This thesis examines the passive detection performance of large aperture arrays in shallow water, interference dominated environments. An important component of the detection performance is an array's spatial resolution, or its ability to discriminate two closely-spaced sources of energy. If an array's resolution is poor, an interferer may lie within the same resolution cell as a quiet target, hence making it impossible to detect the target. This is known as mainlobe-jamming. Alternatively, if an array has high resolution, the array's response to the quiet target is sufficiently different from its response to a spatially separate interferer to permit detection.

Several factors determine an array processor's resolution. First, the physical geometry of the array plays a central role in array resolution. Second, the propagation model used in the array processor impacts the resolution capability as well. Finally, adaptive algorithms may be used to further enhance an array's resolution capability. In practical scenarios, however, physical phenomena such as limited spatial coherence, poor environmental information, and nonstationarity degrade resolution.

This chapter presents a description of propagation models and deterministic resolution capability of large aperture arrays, laying the foundation for the physics behind passive detection in shallow water environments. The chapter begins with a description of seismic systems and the geometry of the arrays modeled in this thesis. This is

followed by a description of three propagation models commonly used in ocean acoustics, namely the plane wave model, the wavefront curvature model, and the normal mode full-field model. Spatial resolution in terms of array geometry and each propagation model is presented as well. This lends insight into subaperture partitioning strategies discussed in Chapter 5. This chapter continues with a discussion of resolution degradation mechanisms. Particular attention is given to spatial decorrelation and a model is presented. Finally, a brief discussion motivating adaptive processing is provided.

2.1 Seismic Arrays

Several systems have been developed by the seismic community to search for oil beneath the sea floor. The technology has matured to the point where ships are capable of towing a variety of planar array configurations. Western Geophysical has the capability of towing a maximum of 20 streamers (horizontal line arrays or HLAs) of 4000 sensors each [21]. They may also tow as many as 10 streamers each 8 km in length. The largest tow to date was performed by PGS with 16 streamers and a total length of 72km in the water [22]. The company CGG may routinely tow up to 16 streamers each containing 960 channels spanning 8km each [23]. While the capacity of these systems may exceed the demands of most passive acoustic applications, a more typical configuration could serve nicely. Current passive USN systems consist of single line arrays towed behind a submarine. The length of these lines is limited in order to maintain maneuverability of the vessel. In contrast, the seismic arrays are towed from commercial vessels designed specifically to handle such large systems. While not operational, these exploration systems provide a vehicle for examining acoustic propagation and the limits of passive detection and localization while eliminating the costs of design and test of an experimental system. By leveraging off of commercially designed and tested technology, research and development costs for such large aperture seismic systems may be drastically decreased. Figure 2.1 shows an aerial photograph of a vessel towing a seismic exploration system [22]. Each streamer can

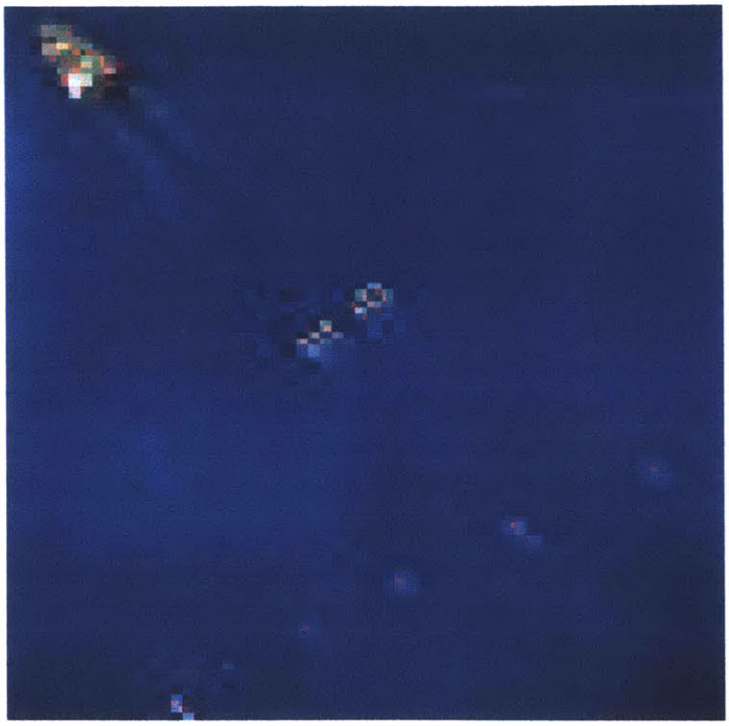

Figure 2-1: Aerial photograph of a seismic exploration system towed behind a vessel.

be seen attached to a winch behind the ship. Also visible in the photograph are a series of air-gun arrays used as the active sources in the seismic system. The actual hydrophone array follows the active section beneath the ocean surface.

Ocean seismic systems are active systems consisting of a series of air guns or other acoustic sources forming a transmit array, and a large horizontal planar towed array of receivers. The portion of the array visible in Figure 2.1 is the airgun array and spreaders used to position the streamers. The receiving hydrophones are typically towed at a depth of near 10m, and are not visible in this photograph. It is this receive array which is of interest to the passive detection problem. Seismic systems operate primarily in the time domain with the receivers recording the signal from the source after reflections from the ocean-sea floor interface, as well as any layers beneath the sea floor. These returns are used to identify the sub-bathymetry of the ocean floor, and detect the presence of phenomena such as oil deposits.

This thesis seeks to use the advantages afforded by the large aperture of the receive

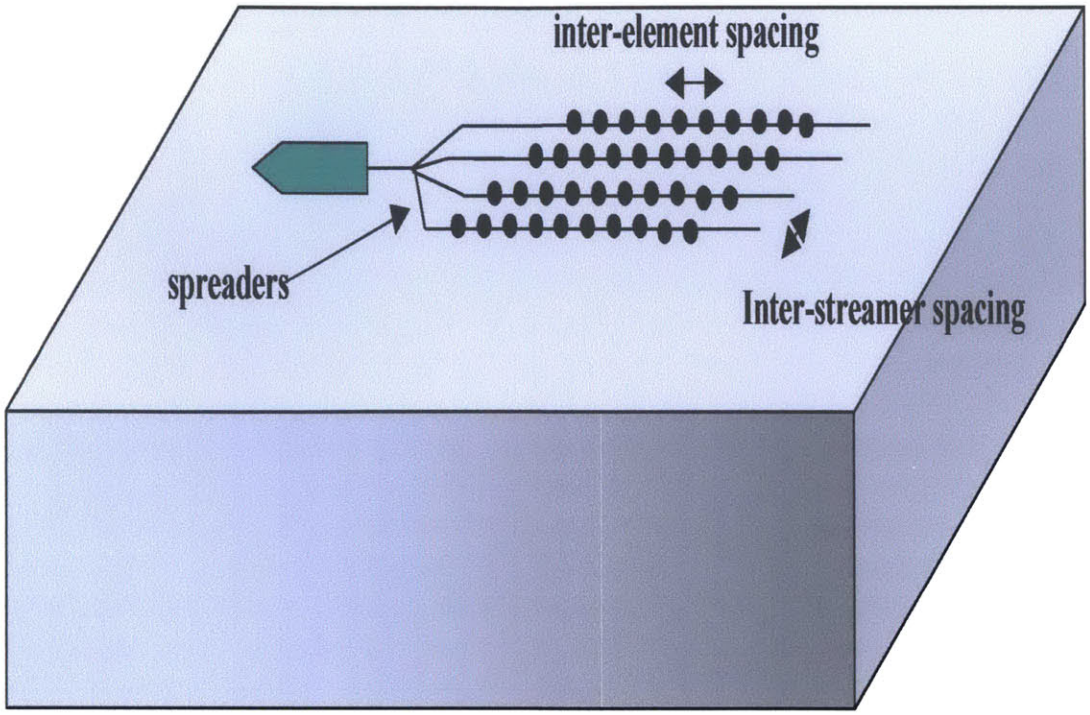

Figure 2-2: Drawing of a seismic system with spreaders shown to separate streamers.

arrays in the seismic system for passive detection by essentially turning the source off. The arrays are modular, and hence can be implemented in various length and breadth combinations. A typical configuration would consist of anywhere from 4 to 12 streamers each on the order of 4km in length. Streamers can be spaced anywhere from 50-100m and span up to 1.3 km across. These streamers are designed to receive frequencies as low as about 10Hz and as high as 500-1000Hz. Typically the arrays are towed at shallow water depths as part of the active system so that surface reflection can be time-gated from the received signal. The arrays are capable of being towed, however, at depths of up to 100m.

Figure 2.2 shows a drawing of such a seismic system. In this thesis, parameters such as inter-element spacing, inter-streamer spacing and number of streamers as well as the number of elements per streamer will be provided for several examples. Note also that the array is towed from a system of spreaders which maintain inter-streamers spacing. These spreaders are an additional source of flow noise.

Such large planar apertures have many advantages over single-line horizontal arrays. At angles near broadside, a linear array is unable to distinguish the vertical arrival angles of dispersive acoustic propagation. It is only near endfire that such an array is able to exploit these characteristics of the signals. A planar array improves this important capability. As will be seen in section 2.2, range and depth resolution of acoustic arrays in the ocean environment is best when an array is vertical, spanning a considerable portion of the water column creating a vertical line array (VLA). Horizontal Line Arrays (HLA), however, possess some of the same benefits of VLAs when the target is oriented endfire to, or in line with, the array's axis. In the case of a planar array, these benefits are extended to scan angles off-endfire as well. An explanation of the resolution based on propagation physics leading to this phenomena appears in the following sections.

2.2 Propagation Models and Array Resolution

This thesis focuses on narrow band frequency domain processing of signals incident upon an array. In all cases, it is assumed that the complex signals incident on the array have been conditioned and then Fourier transformed into the frequency domain. All beamforming and array processing is performed on a narrow-band basis, *i.e.* on a single frequency bin.

The most general form of beamforming, also referred to as conventional processing, simply correlates the data received by the array with a spatial replica based on a model of a hypothesized target. This replica is referred to as the replica vector or steering vector, and may be a function of the target's range, bearing, and depth relative to the array's coordinate system. If the correlation and received power are high, it is assumed that there is a signal present, and if the correlation is low, it is assumed that there is no signal fitting the model present. The fidelity of the propagation model is, therefore, an essential part of array processing. There are several types of array processing algorithms presented in this thesis, and all algorithms require a model for the propagating signals incident upon the array.

There are three models commonly used in passive sonar; the plane wave model, the wavefront-curvature model, and the full-field model. As will be seen in the following subsections, the plane wave model is the simplest, yet provides for array resolution in angle only (azimuth and/or elevation). The wavefront curvature model is more complicated than the plane wave model, yet provides capability for range resolution by an array in addition to angular resolution. Finally, the full-field model can provide range, depth, and bearing resolution, yet is the most complicated of the three. This section presents the propagation physics behind each model and the resolution capability of a large aperture array using each of the three models.

2.2.1 Plane Wave Model

Propagation Model

Most beamforming applications in radar as well as many in sonar are based on a plane-wave propagation model. Signals incident on an array of sensors are assumed to be in the form of waves emanating from point sources at infinite range, hence having planar equi-phase fronts in the direction perpendicular to the propagation direction. This approximation is valid for many deep water acoustic environments in which sound speed variations are very slight leading to line-of-sight propagation. While sources are never at an infinite range to the array, this approximation is valid when a source is in the far-field of the array. In literature, the far field range is any range greater than $2L_{AP}^2/\lambda$, the Fresnel distance, where L_{AP} is the length of the array aperture and λ is the wavelength of the signal in the propagation medium. This wavelength depends upon both frequency and slowness of the propagating ray or mode.

The Green's function for a sensor's response at location $\mathbf{r_i}$ to a point source in free space at location $\mathbf{r_0}$ is

$$g(\mathbf{r_i}|\mathbf{r_0}) = \frac{exp(ik_o|\mathbf{r_0} - \mathbf{r_i}|)}{R} \tag{2.1}$$

where R is the distance between source and receiver and the wavenumber, $k_o = \frac{2\pi}{\lambda}$. As the distance R becomes large, approximating a source at long range, the exponential

term can be simplified to include only the first term in a binomial expansion. The collection of responses to sensors across the array form a replica vector for a source at the spatial location denoted by $\mathbf{r_o}$. Processing using a plane wave model assumes that propagation is in free space, therefore, no boundaries are present, and depth has no reference. Further, the plane wave approximation assumes that the target is at infinite range, leaving the replica to depend only on the spatial angle between the source and array. For a plane wave propagation model, the steering vector accounts for the ratio of depth to range only through elevation angle resolution when using planar arrays. A second quantity used often in this thesis is the wavenumber. It indicates the direction of a propagating wave, and is denoted by $\mathbf{k}$. It is important to note that $\mathbf{k}$ is a vector quantity. We also denote the locations of the sensors in an array with respect to the center of the array as $\mathbf{r_i}$. Using these quantities, the resulting steering vector for a plane wave propagating with a wave-vector $\mathbf{k_o}$ is then a column vector whose elements are

$$v_i = [\exp(i\mathbf{k_o}^T\mathbf{r_i})]. \tag{2.2}$$

In Cartesian coordinates, the wavenumber can be expressed in terms of the free-space wavenumber k_o and the azimuthal and elevation angles relative to the array's coordinate system, ϕ and θ respectively.

$$\mathbf{k_o} = \begin{bmatrix} k_o sin(\phi)cos(\theta) \\ k_o cos(\phi)cos(\theta) \\ k_o sin(\theta) \end{bmatrix} \tag{2.3}$$

The plane wave model is the simplest model, illustrated in Figure 2.3, and is commonly used in radar applications as well as in deep-water ocean acoustic applications when the acoustic signals have very little interaction with the ocean surface and bottom.

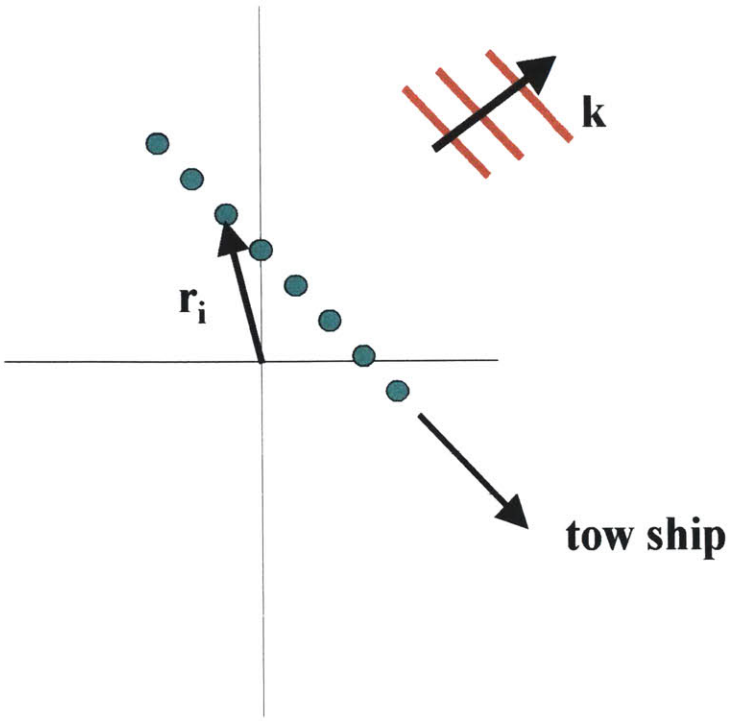

Figure 2-3: Plane wave propagation.

Array Resolution

Since the plane wave model is independent of range and incorporates no boundaries, the only method of discriminating between the replica vector corresponding to different sources is through differences in hypothesized angle. Using classical array theory it can be shown that the azimuthal resolution (*i.e.* the array beamwidth) of a linear, equally-spaced array is given by

$$\theta_{HP} \approx \frac{\lambda}{L_{AP}} \tag{2.4}$$

near broadside and

$$\theta_{HP} \approx \sqrt{\frac{\lambda}{2L_{AP}}} \tag{2.5}$$

near endfire where, again, L_{AP} is the length of the array aperture. Figure 2.4 shows the resolution of a single line, 240-element array (3000m in length) steered to broadside at 50 Hz. The resolution of this array is about 0.6-deg. A linear array, however,

has ambiguities in bearing. For example, consider a linear array oriented along the y-axis. The spatial location vector of each sensor, $\mathbf{r_i}$ contains a non-zero component only in the y-dimension. Therefore, the replica vector will only depend upon the cosine of the hypothesized target azimuth. As a result, a target hypothesized to be at +30-deg fromt he array's axis in azimuth has the same replica vector as a target hypothesized to be at -30-deg azimuth. This ambiguous region forms a "cone of ambiguity" about the linear array, and results from the rotational symmetry of the model. Planar arrays, however, break this symmetry and allow for "left-right" discrimination.

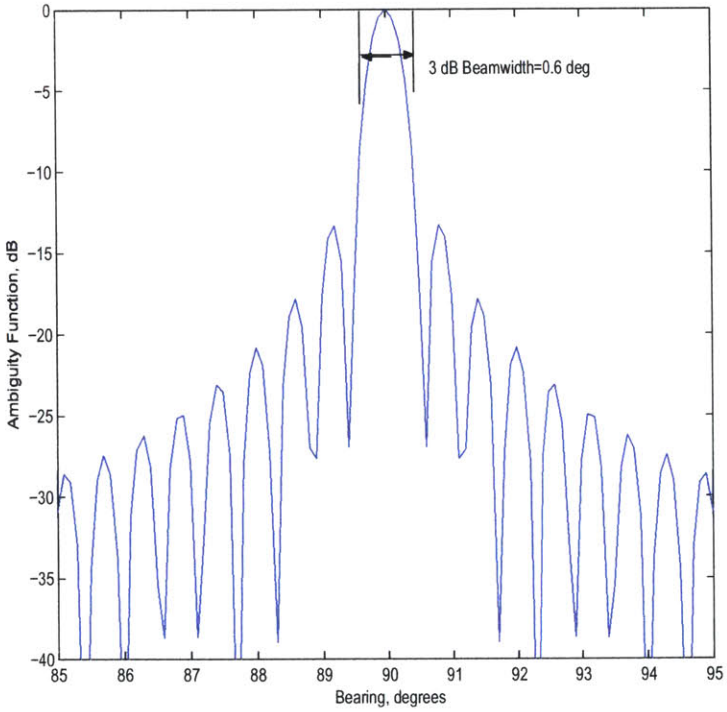

Figure 2-4: Resolution in bearing of a 3000m array of 240 sensors at 50 Hz steered to broadside using a plane wave propagation.

While the propagation model for a plane wave is very simple, it does not account for near-field effects of acoustic propagation. The model assumes that the hypothesized target range is essentially infinite. This approximation is valid when targets are beyond the Fresnel distance. The Fresnel distance for a 3km array at 60 Hz, however, is 360 km. Target detection ranges of interest are on the order of tens of km rather

than hundreds of km. Therefore, use of the plane waves to model acoustic propagation from near-field targets will result in mismatch losses. The wavefront-curvature model helps mitigate these losses.

2.2.2 Wavefront Curvature Model

Propagation Model

In the ocean the speed of propagation for an acoustic wave is far lower than that of an electromagnetic wave in air (1500m/s as opposed to $3x10^8$). Therefore, the far-field range, $R_{ff} = 2L_{AP}^2/\lambda = 2L_{AP}^2 f/c$, is considerably larger for sonar applications than most electromagnetic applications such as radar or cellular communications, as it depends on frequency (or wavelength) and propagation speed. For an acoustic source at 60 Hz in an ocean environment received by a 3 km long array, the source must be 360 km from the array to be considered a far-field source. But in a communications application, a 2 GHz signal for a cellular phone received by a 7.5 cm antenna is in the antenna's far field at a range of 3.75m. In order to account for a target lying in the Fresnel region (*i.e.* inside the far-field range), a method known as wavefront curvature is often employed.

Wavefront curvature refers to a model for the propagation of acoustic waves in which the curvature of the "spherical" wave emanating from the source ismore precisely modeled as illustrated in Figure 2.4. This results in a range-dependent quadratic equation for the propagation.

In the plane wave case, the exponential term in the Green's function was approximated by a first order binomial series. In the wavefront curvature model, a quadratic term in phase must be maintained in order to more accurately capture the curvature of the wavefront. Therefore, the replica vector becomes a quadratic function of sensor location and target range [24].

$$v_i = [\exp(i(\mathbf{k_o}^T\mathbf{r_i} - [k_o^2R^2 - (\mathbf{k_o}^T\mathbf{r_i})^2]/(2R))] \tag{2.6}$$

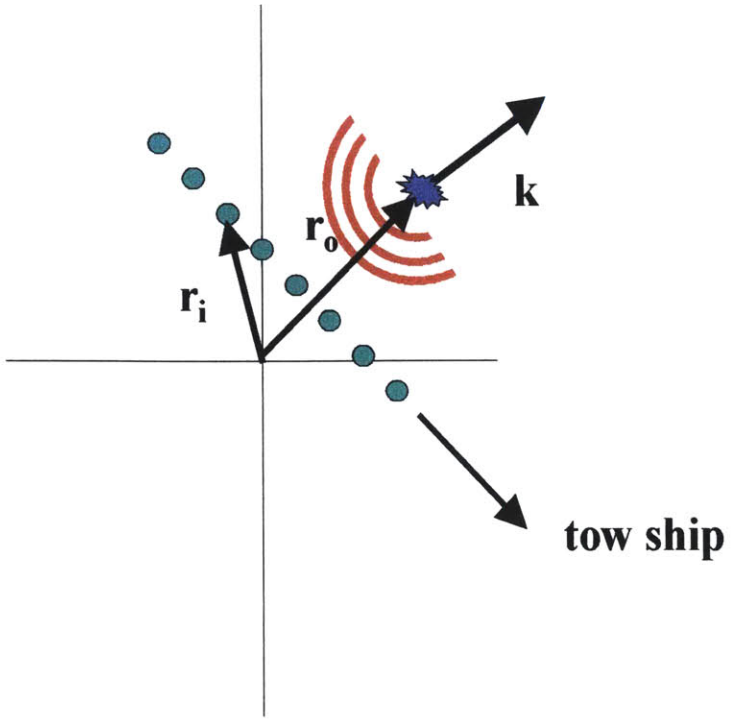

Figure 2-5: Wavefront Curvature propagation model.

Array Resolution

Wavefront curvature modeling is used in holography for acoustic imaging [25], as well as for detection of acoustic signals using large arrays. The wavefront curvature model again incorporates azimuth and bearing information, allowing resolution in angle commensurate with that achieved with a plane wave model. The added complexity of the wavefront-curvature model, however, allows for range resolution.

Range resolution is then approximated as [25], [26]

$$\Delta R = \frac{\lambda}{8}\left(\frac{R}{L_{proj}}\right)^2 \tag{2.7}$$

where L_{proj} is the projected aperture transverse to the hypothesized target direction. Range resolution clearly depends upon the range of the hypothesized target. Wavefronts from targets close to the array have more curvature, and hence smaller range resolution, than those far from the array. Range resolution is also best when

the target is oriented broadside to the array since its projected aperture is equal to its physical aperture. As a hypothesized target bearing veers from broadside, there is a smaller projected aperture with with to sense the wavefront's curvature. In the limit as the target approaches endfire, there is essentially no range resolution, or an infinite range resolution cell in the case of a linear array. A planar array, however, does have a projected aperture transverse to an endfire target, and hence may provide some range resolution. For the planar arrays of interest to this thesis, however, the breadth of the planar arrays is far smaller than the length of the arrays, and wavefront curvature will yield range resolution cells at endfire which are too large to be of practical significance.

Figure 2.6 demonstrates the degradation in range resolution as the focus range increases. The plot on the left is the ambiguity function of a 3000m linear array steered to 3km, broadside. The ambiguity function is the magnitude squared of the correlation of the array response to the target and the array response to the a target at a hypothesised location. The plot on the right is the ambiguity function of the same array focused at 6km. The resolution cell has increased by a factor of 4 when the focus range has doubled.

Many of the targets of interest lie within the near-field of the arrays studied in this thesis, yet they are typically far enough from the array to yield range resolution cells which are too large to benefit detection performance using conventional processing. Further, the wavefront curvature model, while accounting for target range, still approximates the environment as free space. The model does not account for the interaction of acoustic waves with the ocean surface or seafloor. This again leads to mismatch loss. This motivates the need for a full-field model and the technique known as Matched Field Processing.

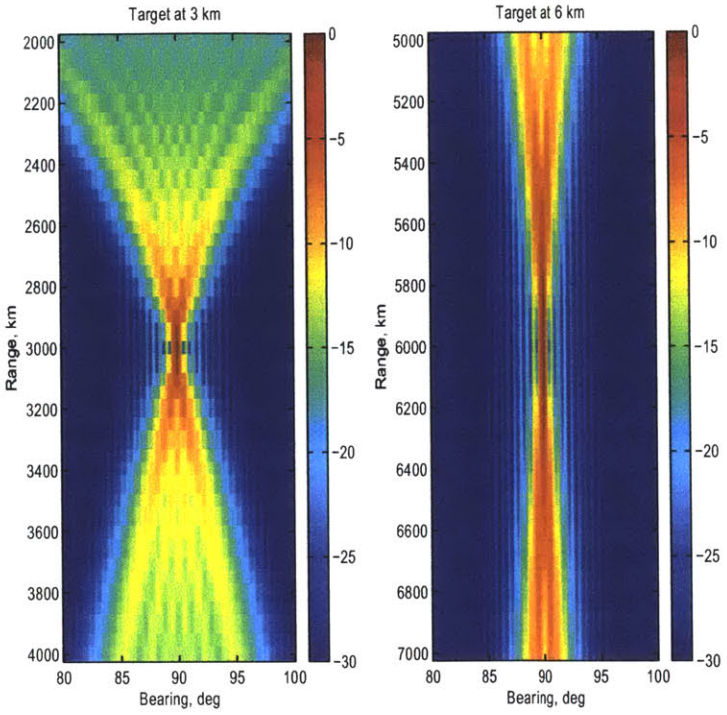

Figure 2-6: WFC resolution using a 3000m array focused at 3km (L) and 6km (R) and 90-deg bearing.

2.2.3 Matched Field Processing

Propagation Model

Both plane wave and wavefront curvature models lead to target resolution in azimuth, and wavefront curvature for large arrays and nearby targets may lead to range resolution as well. Both of these models rely on the frequency and sound speed of the signal of interest and the environment respectively. No other environmental properties are incorporated in these models. When acoustic waves have little interaction with ocean waveguide boundaries, this approximation is reasonable. In shallow water acoustic propagation, however, sound waves have significant interaction with the ocean surface and sea bottom. Source and receivers are usually separated by a distance much greater than the water depth, and signals will reflect from the bottom and the surface of the ocean waveguide many times between the two points. In addition, the sound speed at the top of a shallow water column is often faster than at the bottom

of the water column, causing downward refraction of the acoustic waves. This increases bottom interaction. As a result, a more complete, full-field model for acoustic propagation is needed to accurately represent signals of interest.

Matched Field Processing (MFP) is the method of array processing in which the replica vector is computed using a full-field model for acoustic propagation. The method of source localization in an acoustic waveguide known as Matched Field Processing (MFP) dates back to the early 1970s [26]. MFP steering vectors include the effects of deterministic multipath propagation resulting from interaction with the ocean surface and sea bed. This multipath may be exploited to resolve a target in azimuth, range, and depth. MFP, however, relies on accurate knowledge of the ocean environment. Parameters such as sound-speed, bathymetry, and bottom composition all have a strong impact on the acoustic propagation model. As such, these parameters also impact the range and depth resolution potential of an array in an ocean waveguide.

There are several full-field models in the literature used to describe acoustic propagation in an ocean waveguide. Ray theory is often applied to deep-water environments when refraction due to sound velocity profile (SVP) variations is dominant. While equally valid in shallow water, the interactions with the sea surface and sea floor cause increased computational burden. Parabolic equation and wavenumber integration methods are often used to describe propagation in range-dependent environments. This thesis uses a normal mode propagation model to describe propagation in range-independent, horizontally-stratified, axisymmetric ocean waveguides. The remainder of this section describes the normal mode propagation model and the array resolution capability using such a model.

The wave equation for the pressure field in a vertically stratified, axi-symmetric waveguide due to a point source is given by the Helmholtz equation in two dimensions [27].

$$\frac{1}{r}\frac{d}{dr}(r\frac{dp}{dr}) + \rho(z)\frac{d}{dz}(\frac{1}{\rho}\frac{dp}{dz}) + \frac{\omega^2}{c^2(z)}p = \delta(r)\frac{\delta(z-z_s)}{2\pi r} \tag{2.8}$$

After applying separation of variables, and recognizing this to be a modified

Sturm-Liouville problem, the solution can be written in terms of eigenfunctions and eigenvalues. This results in the normal mode equation which approximates acoustic field at any point by the sum of all propagating modes. This is an approximation, as it neglects the evanescent field. The evanescent field, however, decays rapidly as target range increases. For the problems of interest in this thesis, the array is far enough from the source for the evanescent field to be neglected, allowing for validity of the normal mode approximation. The resulting normal mode expression for the pressure field is given by

$$p(r, z_s, z_r) = \frac{i}{\rho(z_s)\sqrt{(8\pi)}} \sum_{m=1}^{M} \Psi_m(z_s)\Psi_m(z_r)\frac{\exp ik_m r}{\sqrt{k_m r}} \tag{2.9}$$

where Ψ_m are the mode excitation coefficients, k_m are the modal wavenumbers, z_s and z_r are the source and receiver depths and r is the range between source and receiver. Most often, in practice, the normalization term outside the summation is neglected and the pressure field is expressed in terms of a pressure field 1m from the source.

The normal mode propagation model can be interpreted as a superposition of propagating plane waves, each with its own horizontal wavenumber. As such, azimuthal resolution can be determined as in a plane wave model. The horizontal wavenumber spread is generally small enough, that azimuthal resolution can be approximated to be the same as that attained using a plane wave model. The real benefit of MFP, however, comes from the array's ability to resolve targets in range and depth as well by exploiting the multipath propagation structure. Depth resolution may be determined through mode sampling, and range resolution may be determined through both mode sampling and wavefront curvature. The remainder of this section describes the physics behind this resolution capability. For the purposed of this discussion, it is assumed that the signals of interest are perfectly coherent, and the ocean environment is perfectly known. In practice, this is not the case, and this leads to resolution degradation as well as signal gain degradation. That is the subject of section 2.3.

Range and Depth Resolution

The normal mode model may be interpreted as a superposition of propagating plane waves, each with its own horizontal wavenumber. When summing modes at different ranges and depths, the modes will interfere constructively at some locations and destructively at others. An important feature is that the phase response of the array is a non-linear function not only of target bearing, but of source range and depth as well. Hence, by correlating the received data with a normal mode model of a signal of interest, one will obtain excellent correlation if the signal is actually emanating from the prescribed point, and poor correlation if not.

Figure 2.7 demonstrates the multipath propagation represented by the normal mode model. Each trace indicates the propagation path of a plane wave propagating with a different horizontal wavenumber. The magnitude and phase response to a propagating signal is non-linear across the array, and will clearly change as the hypothesized source range and/or depth changes since the array will sample the modes differently. Resolution resulting from sampling these interference patterns is referred to as "mode sampling resolution". It is important to note that this coherent multipath structure exists even when a source is in the far field of the array. The majority of matched field processing literature has focused on vertical line arrays (VLAs) as tools for source ranging [28]. A vertical array, if it spans a significant portion of the water column, is best able to sample modal interference patterns, hence providing the ability to determine target range and depth. This thesis, however, focuses on performance of single HLAs as well as large planar arrays of HLAs.

Horizontal line arrays, when using MFP, are able to provide some ranging capability from mode sampling when a target is oriented endfire to, or in line with the array axis. In this target orientation, the array is able to sample the modal interference patterns and, if the array is sufficient in length, able to yield the same range resolution capability as a fully-spanning VLA [17]. As a source moves off of endfire, however, the ability of an array to resolve the multipath structure degrades due to the cone-angle ambiguity of a linear array. In the limit of a target oriented broadside

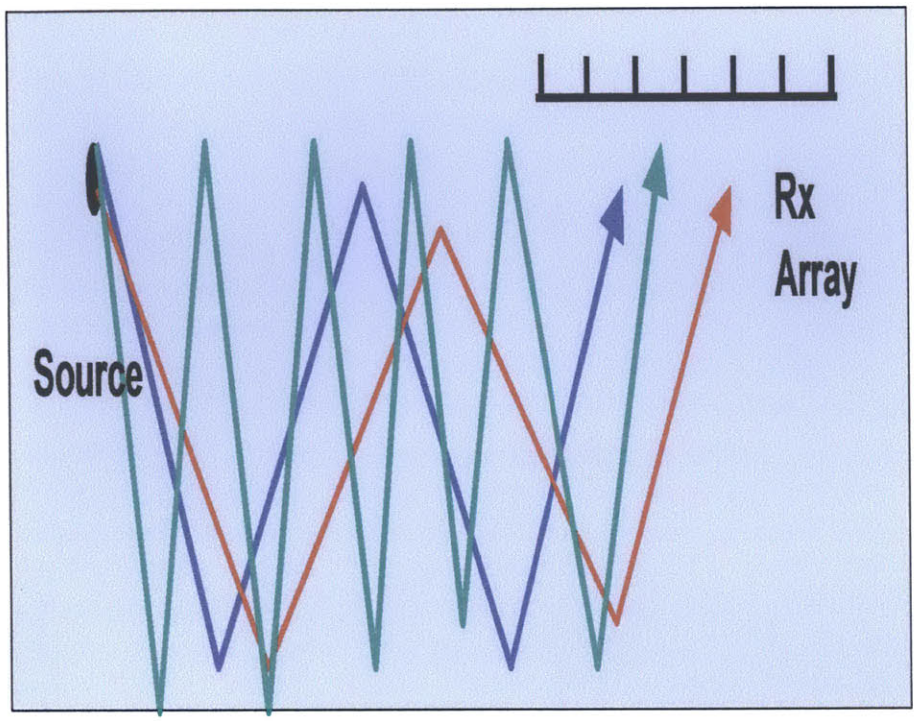

Figure 2-7: Shallow water acoustic modal propagation model.

to a linear HLA, the array is unable to resolve vertical arrival angles of the different modes due to the cone-angle ambiguity, and hence all range/depth resolution from mode sampling is lost.

Recall, however, that the MFP steering vector is a function of range. Therefore, the effects of wavefront curvature are inherently present in MFP. MFP not only accounts for the multipath structure of the propagation, but also the wavefront curvature of each mode. Also recall that the best range resolution using the wavefront-curvature propagation model occurred for targets oriented broadside to a long HLA. So, while a horizontal line array may not be able to resolve the multipath structure of the propagation from a broadside source, MFP is able to provide some ranging capability by exploiting the inherent wavefront curvature built into MFP. To summarize, array processign using MFP leads to ranging capability by exploiting two phenomena; multipath structure of incident fields, and the curvature of tehse multipath wavefronts. The best range resolution is btained through multipath sampling,

thus range resolution is best for a target oriented endfire to the array, yet some range resolution is still available for nearby targets when a source is oriented near broadside due to wavefront curvature effects.

Some quantitative approximations for resolution have appeared in the literature. With the exception of bearing resolution, which was derived in the context of free-space propagation and linear, equally-spaced line arrays, these approximations have been developed in the context of a fully-spanning VLA [29]. Presented here are modified approximations based on HLAs [17], [30]. Using MFP, one may approximate azimuthal resolution very closely by using a plane wave approximation as given in equations 2.4 and 2.5. Range resolution can be approximated by examining the modal structure as well as the array's ability to resolve these modes. Literature has provided the following approximations:

$$\Delta R \approx \frac{2\pi}{\Delta k_{max}} = \frac{\lambda \Delta c_{max}}{c} \tag{2.10}$$

where Δk_{max} is the maximum modal wavenumber separation and Δc_{max} is the corresponding difference in slowness, *i.e.* the spread of the signal. The modal range resolution is often approximated as the difference between the lowest and highest order modes supported by the waveguide that encounter low attenuation, and is a good approximation for a vertical array spanning the water column.

For a horizontal line array, modal resolution only occurs at angles away from broadside. At broadside, the array has no vertical resolution, and all modes appear to arrive at the same angle. Off broadside, an array has vertical resolution due to its projected aperture. The number of resolvable modes, and hence, range resolution, is a function of the size (and resolution) of the array. This projected aperture can be used to determine the maximum wavenumber separation which is resolvable by the array. This can be done in a few steps. First, based on the source bearing, determine the projected aperture in the direction endfire to the target. Second, determine the endfire beamwidth of an array with that projected aperture. Third, determine the highest order mode whose arrival angle is within an endfire beamwidth. If multiple modes

have arrival angles within the endfire beam, the array will not be able to distinguish them and sample their interference. This is k_{min}. Next, find the highest order mode which has not been lost to mode-stripping at the desired range. This is k_{max}. The range resolution can then be approximated as above using $\Delta k_{max} = k_{max} - k_{min}$. This approximation has not appeared in the literature, but agrees reasonably well with simulations.

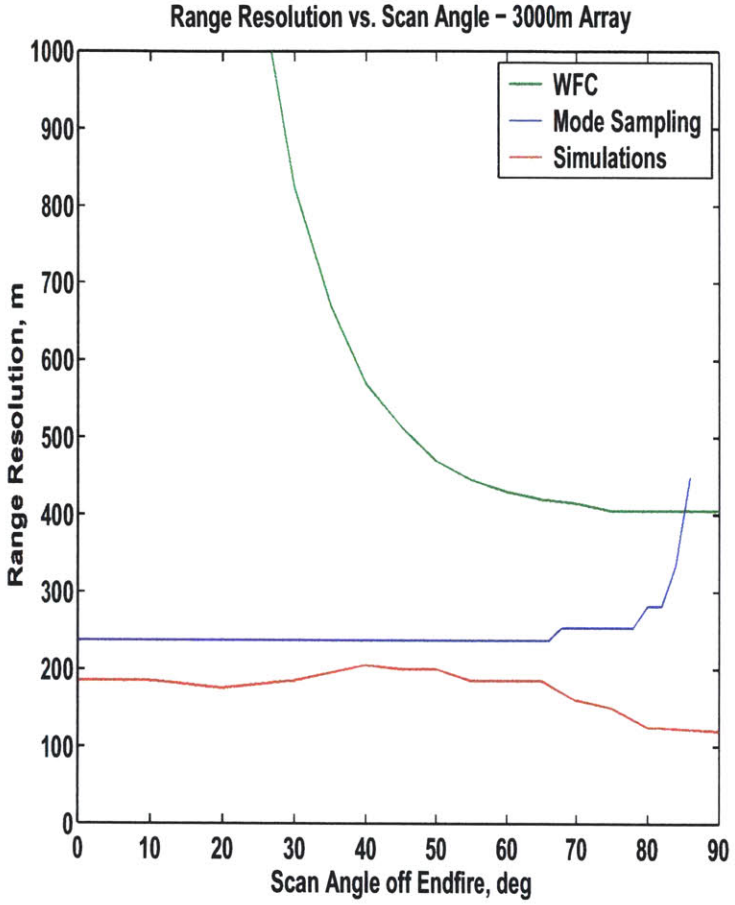

Figure 2-8: Range resolution of a 3km seismic array vs scan angle from simulation using KRAKEN-generated MFP replica vector (red) an approximations using wavefront curvature alone (green) and modal sampling alone (blue).

As shown in section 2.2.2, wavefront curvature also allows limited ranging in the near field [24], [31], [25], and [26], and, when coupled with MFP, can achieve significant range resolution at close ranges. As mentioned earlier, wavefront curvature ranging takes advantage of the fact that waves incident on the array are not planar in

structure, but rather cylindrical or spherical. If a source lies inside the Fresnel range of the array, which most targets will for the case of a large aperture array, the curvature of the wavefront can be significant. With the combination of wavefront curvature modeling and MFP, the array samples different curvature for different propagating modes, improving range resolution. An example of this effect for the case of a single line, 3 km long seismic array and target at 3 km is shown in Figure 2.8. This plot shows the predicted range resolution due to a wavefront curvature propagation model alone in green, the predicted resolution due to modal interference sampling alone in blue, and the simulated range resolution using Matched Field Processing with replica vectors generated using the KRAKEN normal mode code as a function of scan angle. This improved range resolution diminishes, however, as target range increases.

These approximations for deterministic range resolution agree relatively well with simulations. These are not expected to be exact, but only to provide the general behavior and assist in array design, and particularly subarray design. It has been shown that to achieve maximum resolution provided by modal interference, an array must be able to resolve the maximum contributing modes. The resolvable modes can be determined by sampling theory or, more accurately, by examining mode correlation matrix for a specific environment and a specific array [17], [30]. Further, when examining a planar array, subarrays should be chosen to exploit this modal sampling along both axes of the array. This gives the best resolution in all directions. This is discussed in Chapter 5.

In summary, range resolution capability arises from an arrays ability to sample modal interference patterns and wavefront curvature. When using an HLA, modal interference range and depth resolution is best for targets near endfire. Wavefront curvature ranging is strongest for targets near broadside.

Thus far, resolution has been discussed in in the context of linear arrays. The use of planar arrays, however, can extend resolution capability. It has been shown above that the best resolution of an array occurs when a source is located endfire to an array, and degrades as the source bearing moves away from endfire. A planar array creates a situation such that the array has some projected aperture toward which the

source is endfire. With a planar array, the axial symmetry of a linear array is broken hence reducing the "cone-angle" ambiguityand providing better multipath resolution at broadside angles. The range resolution will still depend upon source bearing since the array is much longer than it is wide (streamers are about 3km+ long and span a cross-range of about 1km). The density of sensor in the cross-dimension is typically smaller than along the length of the array as well since the number of streamers is limited. These planar arrays do provide significant improvements, however.

Further, by adding multiple streamers, the azimuthal symmetry of the array is broken. As a result, the array is now able to distinguish sources on its right from sources on its left. This improves resolution significantly, especially in an interference-dominated environment.

Figures 2.9 and 2.10 demonstrate two advantages of using planar arrays in MFP, namely right/left ambiguity rejection and improved range resolution. Figure 2.9 shows the CMFP ambiguity function as a function of bearing for a single line array (blue) and a 20-streamer array (red). The streamers are 3000m in length containing 240 sensors each. The streamers in the planar array are spaced 25m apart. The focus range is 30km, broadside. Clearly the planar array removes the right/left ambiguity seen by the single line. The sidelobes are also greatly reduced using the planar array. The mainlobe beamwidth, however, is essentially unchanged. Figure 2.10 shows the ambiguity function vs. range of both a single line and a planar (20-line) array. The range resolution of the planar array is superior to that of the single line because of its mode-sampling capability. Both arrays have the same length, and hence the same wavefront-curvature capability, but only the planar array provides additional mode sampling.

Clearly, large HLAs provide significant advantages in resolution. Not only does this improved resolution assist in target localization, but it also provides increased interference rejection. Ambiguity surfaces generated through MFP have high "sidelobes" or extraneous peaks. This leads to an increased presence of an unwanted interference signal at a given target location. One way to mitigate these high sidelobes is through adaptive processing. In adaptive processing, the beamforming weights are

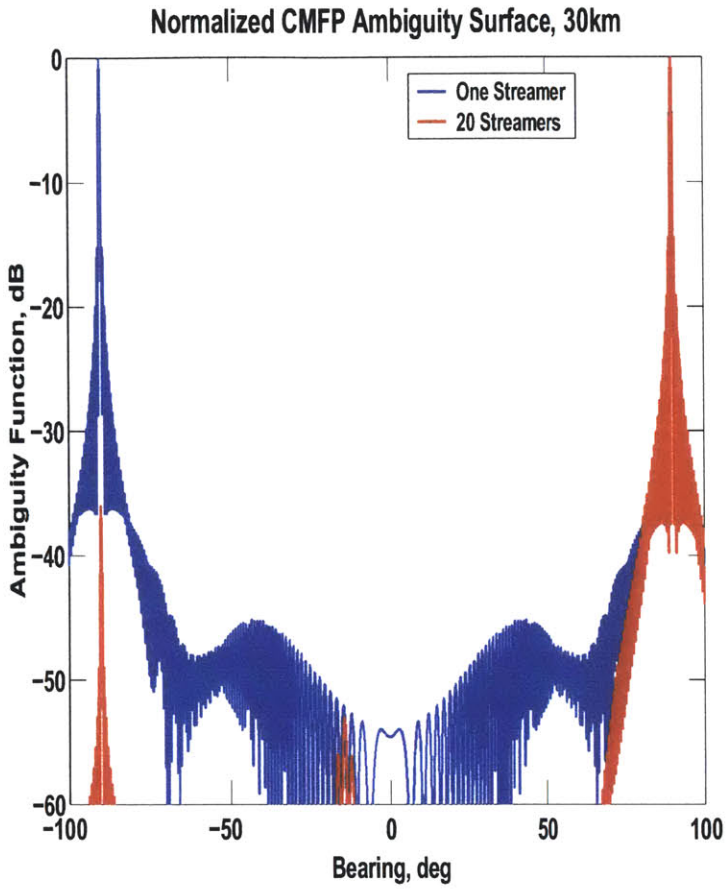

Figure 2-9: Bearing resolution of a single streamer and a 20-streamer planar array showing the R/L ambiguity improvement.

derived from the data itself, *i.e.* adapted, to the environment at hand. Several adaptive processing algorithms as they apply to subarray processing will be discussed in Chapter 3.

2.3 Coherence Degradation and Large Arrays

The array processing methods studied in this thesis rely on correlating some function of a propagation model-based replica vector with the observed data. The performance of the processor, therefore, depends on the fidelity of the propagation model. In practice, the true propagation environment, and hence the true replica vector are not known exactly. This results in a difference between the true array response and

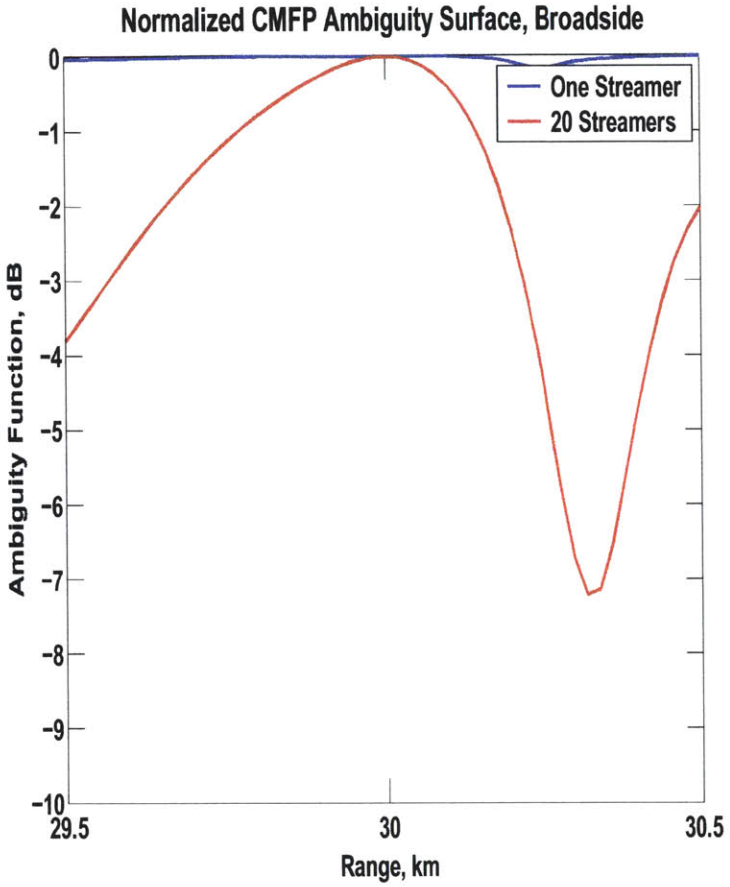

Figure 2-10: Range resolution of a single streamer and a 20-streamer planar array showing the improved range resolution due to modal sampling.

the replica vector. These errors are generally termed mismatch. There are three predominant sources of mismatch:

1. Environmental Mismatch - a result of poor knowledge of the sound velocity profile, bathymetry, basement composition, or other environmental assumptions made in the propagation model.

2. Nonstationarity - target and array motion lead to a replica vector which is time-varying over the observation interval leading to errors when the environment is assumed to be stationary.

3. Coherence Degradation - scattering from a rough sea surface, a rough sea floor,

or inhomogeneities in the water column result in decorrelation of a signal along the array.

Environmental mismatch is very difficult to avoid. Several processing techniques have been developed to reduce a processor's sensitivity to such mismatch [9], [32], and they will be discussed in Chapter 3. Nonstationarity is particularly troublesome to large aperture arrays with high resolution in the presence of moving interference [16]. Subarray processing provides some robustness to this source of mismatch, and this is discussed in more detail in Chapter 3. Finally, coherence degradation is also more troublesome for large aperture arrays. As mentioned earlier, spatial coherence lengths in shallow water are estimated to be on the order of 20-40 wavelengths, yet the arrays of interest are on the order of 100 wavelengths long. Spatial coherence is the topic of this section.

There are two types of signal decorrelation; spatial and temporal. Temporal decorrelation results from non-stationary environments or targets with high Doppler. This affects the duration over which averaging can be performed as well as the sample support available for adaptive processing. Spatial decorrelation manifests itself as a mismatch between the assumed and actual wavenumber spectrum leading to a loss of signal gain. While gross mismatch may occur when one assumes inaccurate sound speed or bathymetry profiles in the model, that is generally treated as a separate issue known as environmental uncertainty or environmental mismatch. The mismatch leading to coherence degradation typically results from random range dependent aspects of the propagation environment which cannot be modeled efficiently. The effects of scattering from rough sea surface or bottom and rapid range dependence cannot be predicted by reasonable amounts of modeling. Additionally, in regions of high current, internal waves and mixing can cause the water to become non-homogeneous, also leading to this spatial decorrelation. Volume inhomogeneities such as air bubbles from breaking waves as well as sea life can also contribute as well. Marine life obstructing the propagation between the source and a portion of the array is another example of a mechanism for this sort of coherence loss. As a result signals often have a finite spatial coherence length [2], [3], [4], *i.e.* a length scale over which volume

inhomogeneities cause little performance degradation. The actual values of spatial coherence lengths are very difficult to measure, and lead to a range of experimental values, and a variety of models for predicting array performance through simulation [2], [3], [4], [33]. Spatial coherence is particularly difficult to measure experimentally in shallow water environments. Deterministic multipath propagation, as calculable from a complete propagation model, leads to unequal amplitudes and nonlinear phase responses across the array. In order to obtain accurate estimates of coherence, one must be able to separate the deterministic multipath effects from the random decorrelation effects. Most often coherence lengths are estimated using sources broadside to an array. The array gain is measured, and from that measurement, the length of the coherent aperture leading to the measured array gain is computed, providing the coherence estimate [2].

This thesis does not focus on the determination of a coherence length, but rather the effects of limited coherence on array processing for quiet signal detection. As such, it is important to model the effects of coherence rather than the mechanisms causing it. There are several models used in practice for these effects [3], [33]. For simplicity, an simple exponential model from the literature is used [3], and modified to incorporate planar towed arrays. It is easiest to explain the model in terms of signal covariance matrices.

The analyses in this thesis assume that acoustic sources are represented by complex Gaussian random processes with mean zero and variance equal to the source strength. Under this assumption, a signal received at the array in the presence of white noise is given by the Nx1 vector $\mathbf{x}$. If the signal is perfectly coherent, the covariance matrix of this data is then given by

$$K = E\left[\mathbf{x}\mathbf{x}^{\mathbf{H}}\right] = \sigma_s \mathbf{v}\mathbf{v}^{\mathbf{H}} + \sigma_{\mathbf{n}}\mathbf{I}. \tag{2.11}$$

When the signal has limited spatial coherence, sensors separated by great distances are less correlated than those close together. In the limit of two sensors becoming completely decorrelated, *i.e.* independent, their expected value of their correlation

goes to zero. The effects of limited spatial coherence therefore, are well modeled by an attenuation of the off-diagonal terms of the covariance matrix. The model used here generates a coherence matrix, denoted by C. This matrix has elements c_{ij} given by [3],[4]

$$c_{ij} = \exp(-\frac{|r_j - r_i|}{L_c}) \tag{2.12}$$

where $|r_j - r_i|$ is the separation between sensors i and j, and L_c is the coherence length of the signal. This model defines the coherence length as the distance between sensors at which the correlation between their received signals drops to 1/e. The coherence-degraded asymptotic covariance matrix is then given by

$$[\tilde{K}] = C. * K \tag{2.13}$$

where '.*' indicates element by element multiplication of the terms in the matrices. This exponential model leads to tractable analytic expressions for array gain as a function of the number of sensors in an array for a linear, equally spaced array in white noise [3].

Since spatial decorrelation is generally a result of propagation through inhomogeneities, or scattering from rough surfaces, it is intuitive that the coherence will depend on both the range of the source as well as its bearing. For example, interference sources are typically much farther from the array than a target of interest in the weak-signal, interference-dominated case. Noise from such interferers will typically experience greater decorrelation than nearby sources. Also, a signal endfire to an array will typically experience less spatial decorrelation than a signal broadside to an array since in the endfire case, the path between the signal and each sensor will have passed through the same water mass. In an effort to incorporate this into the coherence model, the elements of the coherence matrix are modified from equation 2.12 to be

$$c_{ij} = \exp(-\frac{\Delta_{ij}}{L_c}) \tag{2.14}$$

with Δ_{ij} being the projection of the vector connecting sensor i to sensor j in the direction transverse to the source propagation direction. Therefore, a source at endfire is virtually coherent across the array, and a broadside source will experience greatest decorrelation.

It is important to note that the coherence model used in this thesis does not model the mechanism for the spatial decorrelation, but rather the effect of the decorrelation on the observed data. Further, this model preserves the power in the received signal. Since an individual sensor is perfectly correlated with itself, the trace of the covariance matrix is unchanged. As such, the correlation appears in the covariance matrix of the data samples, and fits nicely into the adaptive processing schemes studied later in this thesis.

The seismic arrays of interest are on the order of 120 wavelengths along the length dimension and about 20 wavelengths along the cross-dimension. Clearly, spatial coherence becomes a concern. As a signal decorrelates, the array's ability to resolve two closely spaced signals degrades as well since only a portion of the coherent aperture is available for processing. Further, the white noise gain is reduced. Therefore, much can be gained in terms of detection performance by breaking the array into sub-apertures (subarrays) over which the signal is coherent.

2.4 Motivation for Adaptive Processing

This chapter has provided an overview of propagation models, and introduced Matched Field Processing. Large aperture arrays hold the potential for increased performance in detection and localization of targets, particularly when coupled with MFP. However, most signals of interest are substantially more quiet than loud merchant ships cluttering the observation environment. This results in high power from unwanted interference leaking through "sidelobes" into the observation cell in which a quiet target lies. Additionally, Matched Field Processing, while assisting in 3D resolution capability, has much higher sidelobes than those obtained through plane wave processing. In both cases, the sidelobe leakage from interferers quite often hampers

detection efforts. The most common solution to this problem is what is known as adaptive processing.

Adaptive processing uses the observed data to adapt the weights used in the beamforming stage to reject energy from all directions other than the one of interest. Adaptive processing, while computationally more intensive than conventional processing, can drastically enhance performance. There are several types of adaptive processing, many of which are described in Chapter 3.

There are, however, several challenges to adaptive processing. These fall into three main categories:

1. snapshot support

2. steering vector mismatch

3. degrees of freedom and array resolution relative to interference dimensionality

All methods of adaptive processing studied here rely on the inverse of the data covariance matrix. In practice, the ensemble covariance matrix is unknown, and hence must be estimated from the data. As it is the inverse of the data covariance which is needed, the covariance estimate must be full rank, implying that there must be at least as many data snapshots used in estimating the covariance as there are sensors. In reality, stable estimates require 2-3 times as many snapshots as sensors for good detection performance. When processing such a large aperture array, the required snapshot support becomes unreasonable. When mismatch is present, adaptive algorithms encounter target self-nulling in which the processor mistakes the target of interest for interference since the data is mismatched to the replica vector. Finally, adaptive processors have a finite number of degrees of freedom. Therefore, only a finite interference subspace can be removed. Spatial coherence limitations also impact adaptive processing performance. In a perfect coherence environment, a single signal corresponds to a single eigenvector in a covariance matrix. As the signal decorrelates, however, it tends to span multiple eigenvectors. The problem of ridding an environment of an interferer then becomes not only a problem of nulling a single dimension,

but rather an interference subspace. An array has a finite number of degrees of freedom to be used in interference rejection. Therefore, interference rejection becomes more difficult as interference decorrelates.

Adaptive processing is often needed to improve detection performance, particularly in interference-dominated environments. As will be shown through the remainder of this thesis, adaptive subarray processing helps mitigate these challenges to adaptive processing. The following chapters explore the issues of adaptive subarray processing and subarray partitioning strategy both analytically and through simulation.

Chapter 3

Adaptive Subarray Processing Algorithms

Chapter 2 presented an overview of propagation models and a discussion of array resolution using each model. This discussion was in the context of conventional, *i.e.* non-adaptive processing. It is evident, however, in Figures 2.4, 2.6, and 2.10 that such processing has high sidelobes. The sidelobe level in bearing of an untapered conventional processor is 13.6 dB below the peak, and, with MFP, sidelobes in range can be less than 2 dB below the peak. These high sidelobes can lead to high leakage of interference power into a target resolution cell from other spatial locations. In this thesis, detection is performed using a likelihood ratio test of power estimates on a resolution-cell by resolution-cell basis. Therefore, in high interference environments, sidelobe leakage can mask quiet targets and hamper detection performance. Several techniques have been developed in the literature to mitigate sidelobe leakage and are generally termed adaptive techniques.

This chapter begins with a brief presentation of the notation used in this thesis as well as the signal model and framework for the detection problem. It continues with an overview of several adaptive techniques for full-array processing. It follows with a presentation of the challenges of adaptively processing large aperture towed arrays, motivating the need for subarray processing. It then presents further motivation for subarray processing in coherence-limited environment as an interpretation of the

optimum processor. Finally, three commonly-used adaptive subarray algorithms are presented. These algorithms are the focus of the statistical analysis presented in Chapter 4.

3.1 Notation

The remainder of this thesis will involve a considerable amount of notation, as these algorithms are discussed. For clarity, some of the notation used frequently is provided for reference. First, vectors will be noted as boldface lowercase letter. Matrices will be denoted by capital letters. A few capital letters, however, are reserved. The number of sensors in an array is denoted by N, the number of snapshots used in calculations is denoted by L, and the number of subarrays is given by M.

$\mathbf{x}^l$ data snapshot vector indexed by l

X snapshot matrix

$\mathbf{v}$ steering vector

$\mathbf{w}$ weight vector

K covariance matrix, markings distinguish different stages of processing

y power estimates

3.2 Signal Models

Before a detailed analysis begins, it is useful to present the data model used in this thesis. As mentioned earlier, all data is modeled in the frequency domain, and all processing is performed on a narrow-band basis.

A standard practice [26] is to model a signal incident upon an array as a random source propagating through a deterministic channel. In addition to a signal of interest, there is noise present corrupting the measurement. Two types of noise are modeled in this analysis; discrete noise resulting from loud surface ships, also referred to as clutter, and white noise which is uncorrelated from sensor to sensor, often a result of

acoustic energy generated by the flow of water past the sensors on the array. Ocean acoustic noise also contains a diffuse component, for example noise generated by wind hitting the ocean surface as modeled by Kuperman and Ingenito [40]. The problem of interest in this thesis is detection in an interference dominated environment. As a result, the diffuse wind noise is much less a contributing factor, and will be neglected from the data model. The analysis method presented here, however, is equally valid for cases which include diffuse noise.

Under Hypothesis 1, the model for a received data snapshot is given by

$$\mathbf{x} = b\mathbf{v} + \sum_{i=1}^{Nints} s_i \mathbf{d}_i + \mathbf{w} \tag{3.1}$$

and under Hypothesis 0 a snapshot is given by

$$\mathbf{x} = \sum_{i=1}^{Nints} s_i \mathbf{d}_i + \mathbf{w} \tag{3.2}$$

where N_{ints} is the number of interferers in the environment. The vectors $\mathbf{v}$ and $\mathbf{d}$ are deterministic steering vectors representing the array response to a source or interferer. The scalar quantities b and s are the random source and interferer excitations, and are assumed to be complex Gaussian random variables. Finally, the vector $\mathbf{w}$ represents the uncorrelated component of the noise and is a Gaussian random vector. Further, the random signal source is assumed to be uncorrelated with the random interference sources which are also taken to be independent of each other. The white noise is uncorrelated with the discrete source terms as well. Hence, these snapshots are modeled as Gaussian random vectors, and independent from one snapshot to the next.

All sources and noise are assumed to be zero mean, hence the snapshots are zero mean. Since the data is modeled as a complex, Gaussian random vector, the only remaining quantity needed to completely characterize their statistics is then, the covariance matrix of the snapshots. The snapshots covariances are denoted K_1 for snapshots under the "signal present" hypothesis and K_0 for snapshots under the

"signal absent" hypothesis. They are given by

$$K_1 = \sigma_s^2 \mathbf{v}\mathbf{v}^H + \sum_{i=1}^{Nints} \sigma_{I,i}^2 \mathbf{d}_i \mathbf{d}_i^H + \sigma_n^2 I \tag{3.3}$$

and

$$K_0 = \sum_{i=1}^{Nints} \sigma_{I,i}^2 \mathbf{d}_i \mathbf{d}_i^H + \sigma_n^2 I \tag{3.4}$$

respectively with the *pdf* of the snapshot then given by

$$p_{x|H_i}(\mathbf{x}|H_i) = \frac{1}{\pi^N |K_i|} e^{-\mathbf{x}^H K_i^{-1} \mathbf{x}} \tag{3.5}$$

It should also be noted that the analysis to this point has assumed that the vectors $\mathbf{v}$ and $\mathbf{d}$ are generalized array response to sources at fixed, hypothesized source locations. In reality, the array response vectors are functions of many different parameters such as bearing, range, and perhaps, for MFP, depth and environmental parameters. These parameters could be treated as nuisance parameters in a generalized likelihood ratio test formulation, but for the purposes of the analyses in this thesis, these parameters are assumed to be known. Plane wave, wavefront-curvature, or full-wave propagation models may be used without loss of generality. Also, the quantities σ_s^2, $\sigma_{I,i}^2$, and σ_n^2 represent the element-level target, interference, and white-noise power levels, respectively.

At this point it is useful to alter the data model to incorporate the effects of limited spatial coherence. The model used in this thesis is taken from [3] and was detailed in Chapter 2. Recall that coherence effects are incorporated modifying the covariance matrices. With this simple modification, the covariance matrices are now given by

$$K_1 = \sigma_s^2 \left(\mathbf{v}\mathbf{v}^H\right) .* C_{sig} + \sum_{i=1}^{Nints} \sigma_{I,i}^2 \left(\mathbf{d}_i \mathbf{d}_i^H\right) .* C_{int,i} + \sigma_n^2 I \tag{3.6}$$

and

$$K_0 = \sum_{i=1}^{Nints} \sigma_{Ii}^2 \left(\mathbf{d}_i \mathbf{d}_i^H\right) .* C_{int,i} + \sigma_n^2 I \tag{3.7}$$

The terms C_{sig} and $C_{int,i}$ are the signal and interference coherence matrices. In summary, the snapshots are complex normal random vectors with zero mean and covariance K_i where i=0,1 indicates the hypothesis upon which the snapshot is conditioned.

3.3 Detection Framework

The problem of detecting a target in the presence of noise has been studied extensively in the past. Many volumes have been written on the subject, one of which [41] is particularly complete. A common framework for the detection problem is known as binary Likelihood Ratio Test (LRT), is used in this thesis.

The binary LRT is a framework for testing two hypotheses about the received data, namely, the presence or absence of the signal of interest in the measurements. The LRT determines which hypothesis is statistically more likely to be true. Hence, signals received at the array either have a target signal present (Hypothesis 1) or absent (Hypothesis 0). It is important to note at this point that the analysis presented here is established as a binary hypothesis test. In doing this, one has selected a fixed spatial location one wishes to test for target presence. This analysis does not directly address the localization issue. The idea is that localization would be performed by repeating this analysis in many different spatial locations, and comparing results. This analysis is for the detection stage only, and does not assess the sidelobe ambiguities of the localization problem.

The likelihood ratio test forms the ratio of probability density functions of the observations conditioned on each hypothesis shown in equation 3.xx where η is the selected threshold and Λ is the likelihood statistic. This ratio is then compared to a threshold to determine which hypothesis is most probably correct. In this thesis, the threshold is set using a Neyman-Pearson criterion specifying a fixed probability of false alarm.

$$\Lambda = \frac{p_{y|H_1}(\mathbf{y}|H_1)}{p_{y|H_0}(\mathbf{y}|H_0)} \gtrless \eta \tag{3.8}$$

This thesis will use a modified form of the LRT by taking the natural logarithm of both sides creating the log-likelihood ratio test, which is very helpful when dealing with Gaussian observations. The LRT is also simplified such that only observation-dependent terms are on the left hand side of equation and all deterministic terms are absorbed into the threshold. This work will refer to the sufficient statistic of the LRT (i.e. a function of data-dependent terms) as l for simplicity.

The LRT and Log-LRT both lead to two important performance metrics. These are the probability of a correct detection (P_d) and the probability of a false alarm (P_f). These are defined as

$$P_d = \int_{\eta}^{\infty} p_{l|H_1}(l|H_1)dl \tag{3.9}$$

$$P_f = \int_{\eta}^{\infty} p_{l|H_0}(l|H_0)dl \tag{3.10}$$

These two metrics are used in concert to assess the performance of algorithms in this thesis. The metric used herein to compare and assess performance of various algorithms is the constant probability of false alarm (P_F) detection probability. This is the probability of correctly declaring a target present given a constant (and low) probability of declaring a false alarm. Therefore the threshold is chosen to yield the desired probability of false alarm, and the probability of detection P_d is given by equation 3.9.

3.4 Adaptive Array Processing Algorithms

This section provides a survey of adaptive processing techniques common in the literature. Adaptive array processing is used in this thesis as a parameter estimation technique, in which directional power of the signals incident upon an array (*i.e.* bearing, range, power, etc) is estimated. The adaptive algorithms under consideration here all focus on estimating the power incident on an array from a source at a specified spatial location. As will be shown later in this chapter, this power estimate is

then used as the "data" in a binary hypothesis test for detection. These adaptive algorithms, therefore, try to discern only the power emanating from one spatial resolution cell, and reject interference from other resolution cells. The subarray processing algorithms studied in this thesis are all derived from this collection of algorithms.

Most array processing algorithms involve computing a set of complex coefficients, or weights, which, when applied to the signals received on each element of the array (data vector), leads to coherent addition of signals coming from a desired "look" direction. This weight vector is a spatial filter which, when applied to the data, yields a power estimate for a source emanating from that point. This estimate is then used in a post-processing algorithm to detect, and possibly localize, that signal. The accuracy of the power estimate has a big impact on the post-processing. As seen in Chapter 2, Matched Field Processing uses a more complex propagation model rather than a plane wave assumption to determine these weights. Typically, in MFP, a different set of weights is computed for each range, bearing, and depth cell, and the results are used to form an ambiguity surface. The target location estimate is then considered the point of local maximum power. Aside from the signal modeling, the algorithms are identical for plane-wave processing or environmentally-based processing. The crux of the problem lies in the appropriate choice of weights.

All forms of processing follow the same general block diagram shown in Figure 3.1. As mentioned in Chapter 2, the analyses in this thesis work with data snapshots which have already been transformed from the time series to frequency domain at the element level. Processing will then be performed on a narrow-band (or single frequency-bin) basis. A weight vector is then computed according to the desired algorithm. This section begins by examining the conventional, or non-adaptive, processor as a baseline. This is followed by two classes of adaptive algorithms; constrained optimization methods and eigen-filtering methods.

3.4.1 Conventional Processing

The most basic form of array processing is known as conventional processing. In this algorithm, the processor determines the amount of energy in a particular look-

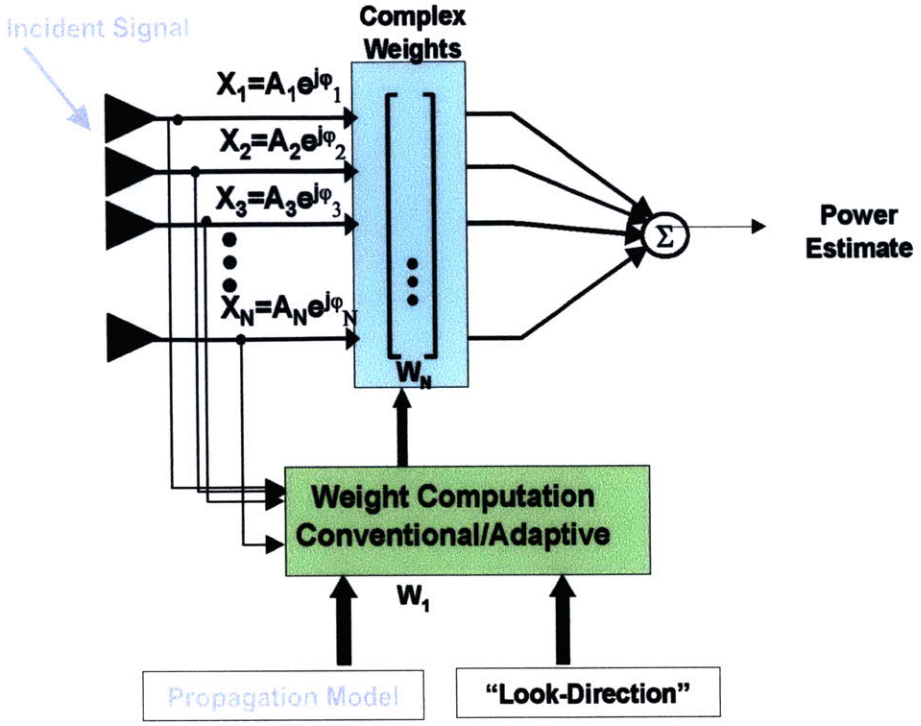

Figure 3-1: Generalized block diagram for processing stream.

direction by essentially using a matched filter. The matched filter is simply the Hermitian transpose of the replica vector normalized by the number of sensors. This provides an undistorted response of the array to a signal at a particular direction. However, this method takes no steps to suppress leakage of spatially distinct signals through sidelobes. The algorithm is expressed as follows. Conventional processing can be applied on a snapshot by snapshot basis or to an ensemble covariance matrix, as shown in the equations below.

$$\mathbf{w_{cbf}} = \frac{1}{\mathbf{N}}\mathbf{v}(\mathbf{k_T}) \tag{3.11}$$

$$y = \frac{1}{L}\sum_{l=1}^{L} |\mathbf{w_{cbf}^H x^l}|^2 \tag{3.12}$$

or

$$y = \frac{1}{L}\mathbf{w_{cbf}^H X X^H w_{cbf}} \tag{3.13}$$

In this formulation, $\mathbf{v}$ is the replica vector, also known as a steering vector. It is, as described in Chapter 2, a function of the source parameters such as frequency and spatial location. N is the number of sensors in the array, and L is the number of snapshots. This work focuses on cell-by-cell detection rather than spatial parameter estimation. Therefore, the replica vector is computed for the hypothesized source location. The detection is then repeated for alternate spatial locations as desired.

Since this algorithm does not depend upon inverting the covariance matrix, it is fast, simple, and commonly used. The high sidelobes inherent in MFP, however, lead to particular difficulty in interference rejection with conventional processing. Tapers may be applied to reduce sidelobes in plane wave models, but such tapers are empirical for MFP, thus motivating the need for adaptive processing.

3.4.2 Minimum Variance Methods

A large portion of adaptive beamformers is based on optimizing a function of the weight vector over the weights while constraining it in some way. Perhaps one of the simplest and commonly used of these is the Minimum Variance Distortionless Response (MVDR) algorithm, often referred to as Capon's Maximum Likelihood Method [31], [34]. This is formally cast as an optimization problem and, from this, many extensions have been developed. Many other adaptive algorithms appear in the literature [34]. The MVDR algorithm and its variants are the most relevant to this thesis, and are presented here as the basis for the subarray analysis to follow.

MVDR minimizes the output power of the beamformer subject to the constraint that there be unit gain in the direction of interest. The weight vector and steering vectors are functions of the hypothesized target direction, $\mathbf{k_T}$, but that explicit notation is suppressed for convenience. Mathematically, this can be stated as

$$\min(\mathbf{w_{mv}^H K w_{mv}}) \tag{3.14}$$

subject to

$$\mathbf{w_{mv}^H v} = \mathbf{1}. \tag{3.15}$$

Using Lagrange multipliers and matrix differentiation, the solution for the weights is given by

$$\mathbf{w_{mv}} = \frac{\mathbf{K^{-1}v}}{\mathbf{v^H K^{-1} v}} \tag{3.16}$$

and the output power is given by

$$y_{mv} = \mathbf{w_{mv}^H K w_{mv}} = (\mathbf{v^H K^{-1} v})^{-1} \tag{3.17}$$

Note that this relies on inversion of the covariance matrix. In practical situations, the true data covariance matrix is not known a priori, and the implementation of MVDR becomes more challenging. In most practical cases a quantity known as the sample covariance matrix is used in stead. This will be discussed in section 3.5.

There are several variations to the MVDR algorithm. One such variation is known as a multiple constraint method. In this case, the constraint matrix imposed on the optimization problem is not only the unity gain constraint, but also other constraints that shape the beam response. For example, if it is known that interference is arriving from a particular direction (*i.e.* a surface ship with location known from radar data), constraints can be added forcing the the beam pattern to place a null in that direction. The number of constraints that may be imposed is related to the degrees of freedom of the array. Constraints may also be specified so as to limit the first and second derivatives of the beam response. Numerous variations of the method have been implemented and reported in the literature [34].

Yet another variant of MVDR involves the use of soft constraints. One approach to improve interference rejection is to minimize the distortion of the desired response of the beamformer over a desired angular sector [35]. This results in a quadratic constraint on the weight vector. This can be used to several purposes. First, it can improve interference rejection, and secondly, it can reduce self-nulling due to slight errors in the steering vector. MVDR is a very high-resolution beamformer with a very narrow main beam, especially in high SNR environments. When the adaptivity is stressed either through a lack of array resolution or insufficient degrees of freedom, it leads to pattern distortions and high sensitivity. This has a strong impact on

subarray algorithms and subarray configurations which will be seen in Chapter 5.

Another optimization-based algorithm is known as the Generalized Sidelobe Canceller (GSC). A thorough description of the algorithm can be found in [31], and a performance analysis is given in [20]. The GSC algorithm is formulated as an optimization problem with a constrained optimization and an unconstrained optimization, The GSC seeks to remove sidelobe interference while preserving all signal in the target direction. Essentially, the power estimate is formed by subtracting a filtered beam response from a conventional beam response in the direction of the target. The unconstrained portion of the optimization determines the adaptive part of the weight chosen to minimize the beam response over the adaptive portion of the weight. The result is an algorithm which removes interference while preserving main beam characteristics.

While MVDR and its associated variants are often implemented at the element level, it is often useful to perform adaptive beamforming in beam space with beams pointed differently in a cluster [9], [34]. This has analogies, as will be seen later, to subarray processing. In this method, the element-level data is projected onto a set of beams. A new covariance matrix is formed using the complex projections onto beam-space, and adaptive processing is applied to beam data. This often reduces the dimensionality of the problem by applying MVDR to a reduced degrees-of-freedom problem which can be computationally more efficient. One of the subarray algorithms to follow is essentially identical, except that the transformation is to subarray outputs steered to the same direction rather than beam outputs steered to different directions. One advantage to performing MVDR in beam space rather than subarray space is that there may be fewer beams of interest than subarrays. This, then, leads to fewer required snapshots. The drawback to beamspace processing is that locations of loud interference are not always known, leading to a poor beam selection, and poor nulling of interference sources. A comparison of beamspace MVDR and subarray-space MVDR appears in Chapter 5.

It is instructive to look at the MVDR algorithm in terms of the eigen-structure of

the covariance matrix. The inverse of the data covariance matrix can be expressed as

$$K^{-1} = \sum_{i=1}^{N} \frac{1}{\lambda} \phi_i \phi_i^{\mathbf{H}} \tag{3.18}$$

where ϕ_i are eigenvectors and λ are their associated eigenvalues. If the steering vector is aligned with one eigenvector, its projection onto that eigenvector is approximately 1, and the output power of the beamformer is approximated by the associated eigenvalue. It is important to note that small eigenvalues have a large contribution to the inverse covariance matrix. Therefore, in forming the sample covariance matrix, it is important to have enough snapshots such that the small eigenvalues are well estimated lest there be high errors in the adaptive weight. This and other challenges to adaptive processing as well as *ad hoc* algorithms to compensate for them are discussed in section 3.5.

3.5 Challenges to Adaptive Processing

Adaptive processing, also known as high-resolution processing, improve resolution by rejecting interference. All of these algorithms rely, in one way or another, on inverting a covariance matrix. In most practical situations, the true covariance matrix of the data is unknown. Therefore, it is common for the sample covariance matrix (SCM) to be used. This is the Maximum-Likelihood (ML) estimate for unstructured covariance estimation when snapshots are assumed gaussian random variables. Adaptive algorithms are subject to two main challenges: snapshot support and target self-nulling due to mismatch errors. This section details these two issues and presents several *ad hoc* algorithms which have been developed to compensate for them.

3.5.1 Sample Covariance Rank and Stationarity

The analysis in this thesis models frequency-domain data snapshots across the array as complex Gaussian random vectors. It is further assumed that snapshots of data have been chosen such that they are independent. Under that assumption, the SCM is simply the sum of the outer products of data snapshots. In order for a SCM to

have an inverse, it must have full rank. Therefore, the number of independent snapshots comprising that SCM must be at least as large as the number of entries in the individual snapshot (usually the number of array elements). The sample covariance matrix is thus defined as

$$\hat{K} = \frac{1}{L} X X^H \tag{3.19}$$

where X is the matrix of data snapshots acquired in time. One drawback to this method is that if the covariance matrix is poorly estimated, the target may appear noise-like, and hence be susceptible to self-nulling.

A second assumption inherent in most adaptive algorithms is that the covariance matrix does not change over the observation interval during which the SCM is estimated. That means that targets and interference must remain within a single resolution cell of the array during the observation. This is a considerable challenge to passive sonar processing, particularly in littoral regions. Environments of interest are quite often littered with high-bearing rate merchant ships which pose as interferers. When processing large arrays with high resolution, this can be troublesome [16]. This is illustrated in Figure 3.2. If one assumes the smallest resolution cell is in azimuth, and that the target is moving radially, the time a target spends in a resolution cell is given by

$$\Delta T \approx \frac{1}{L_{ap}\dot{\phi}} \tag{3.20}$$

where $\dot{\phi}$ is the bearing rate of the target and L_{ap} is the length of the aperture. The bandwidth over which averaging can be done without incurring significant phase errors (*i.e.* FFT bandwidth) is

$$B \approx \frac{1}{8T_{Trans}} \tag{3.21}$$

where T_{Trans} is the maximum time it takes a wave to propagate along the length of the array. The time per snapshot is then 1/B, and the available snapshots is then given by

$$L = B\Delta T \approx \frac{f}{8\dot{\phi}}(\frac{\lambda}{L_{ap}})_2 \tag{3.22}$$

As arrays get very large, the number of available snapshots gets very small.

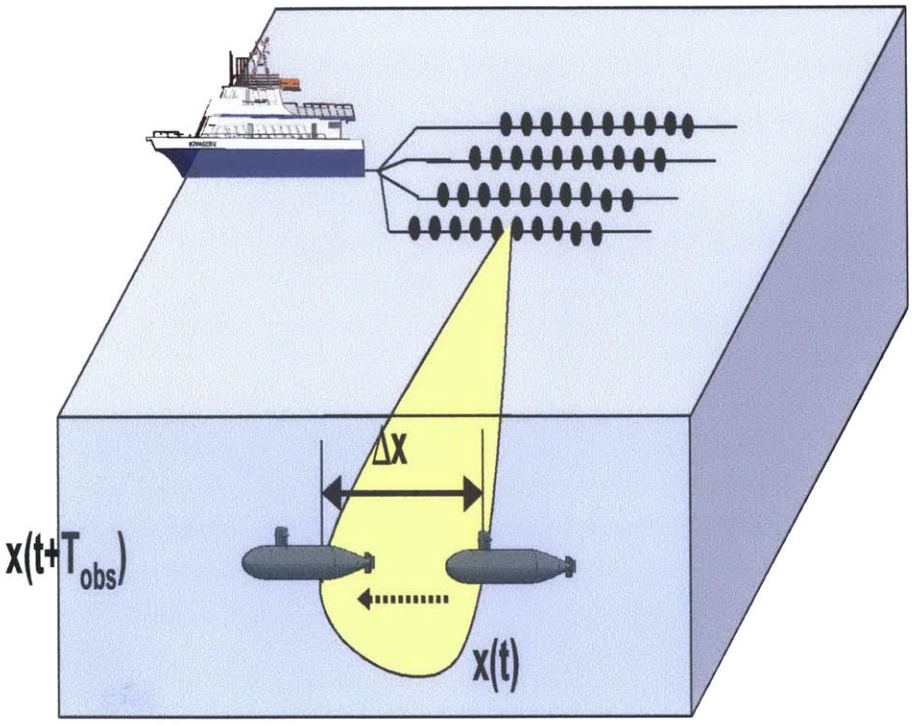

Figure 3-2: There is a finite time during which a target will remain within a single resolution cell of the array.

3.5.2 Mismatch

A further complication of adaptive processing is the issue of mismatch. Chapter 2 presented several models for acoustic propagation in the ocean environment. It has been assumed, until now, that the propagation is known perfectly. That is not the case, however, in practice. It is clear that in a shallow-water propagation environment the plane wave model is not an accurate reflection of propagation. Therefore, when the plane wave model is used, an adaptive processor tries, to some extent, to reject the signal of interest because it is not perfectly matched with the steering vector chosen. Further, it is very difficult to accurately estimate all of the environmental parameters needed for the normal mode model. There may be errors in the sound velocity profile or bottom composition leading to steering vectors which are mismatched to the true propagation, again leading to target self-nulling. Figures 3.3 and 3.4 show an example of the effects of this mismatch. Figure 3.3 shows two sound velocity profiles, the true SVP in blue and "assumed" SVP in red. Figure 3.4 shows the resulting ambiguity surfaces when MVDR is employed with the true SVP used for the data in both plots. The left plot uses the true SVP in computing the weight vectors, and the right hand side shows the surface using the assumed (incorrect) SVP. The target is located at 5 km from the array, at 30-degrees and 100m depth. There is also a surface interferer located at 31-degrees in bearing and a depth of 5m. A single streamer was used in this calculation, and the average element-level SNR is 2 dB. The mismatched SVP results in a loss in the power estimate as a result of self-nulling, and an obscuring of the target of interest from the interferer. For two-dimensional arrays, mismatch is an even greater problem since propagation both along the array's length and across streamers must be known.

Target self-nulling is particularly troublesome for passive sonar because the target of interest is in the data. In active systems, one often has "target-free" training data which may be used to form the adaptive weights. As a result, none of the adaptivity is used to null a mismatched signal because the signal is not present in the data. In passive sonar, however, there is no opportunity for target-free data.

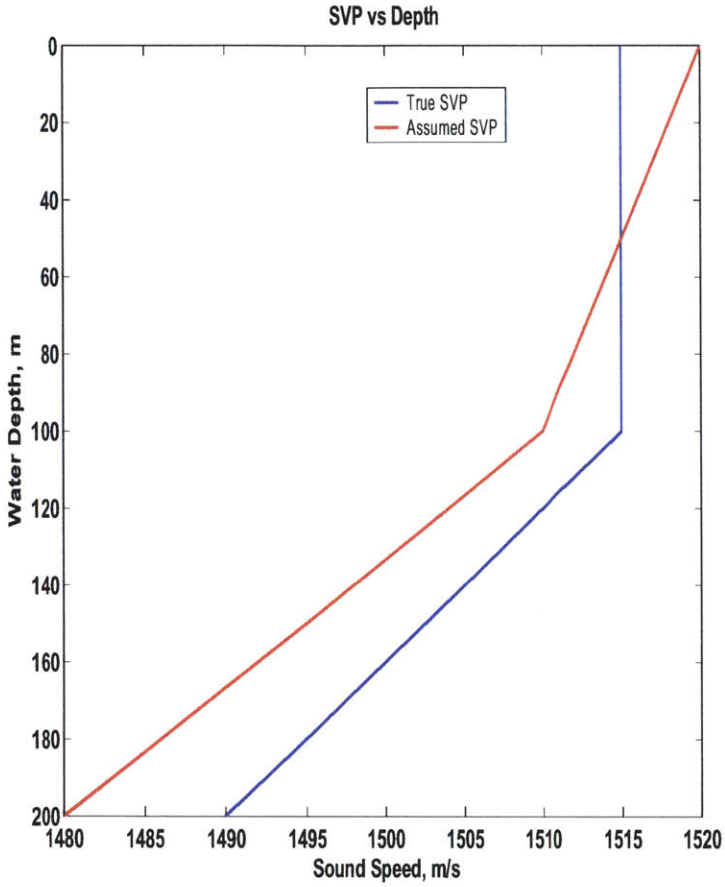

Figure 3-3: True and assumed sound velocity profiles. The water column is 200m in depth.

The problem of self-nulling resulting from target-in-training has the potential to cause even more problems in a low-coherence environment. The MVDR algorithm enforces the unit gain constraint in a single spatial direction, assuming no target decorrelation. When the target spectrum is spread in wavenumber space as a result of decorrelation, the target spectrum is no longer fully "protected" by the unit-gain constraint. This effect will be seen later in Chapter 5.

3.5.3 Ad Hoc Algorithms

Passive sonar processing is very often faced with the challenge of performing adaptive processing in environments where there is limited environmental information [32],

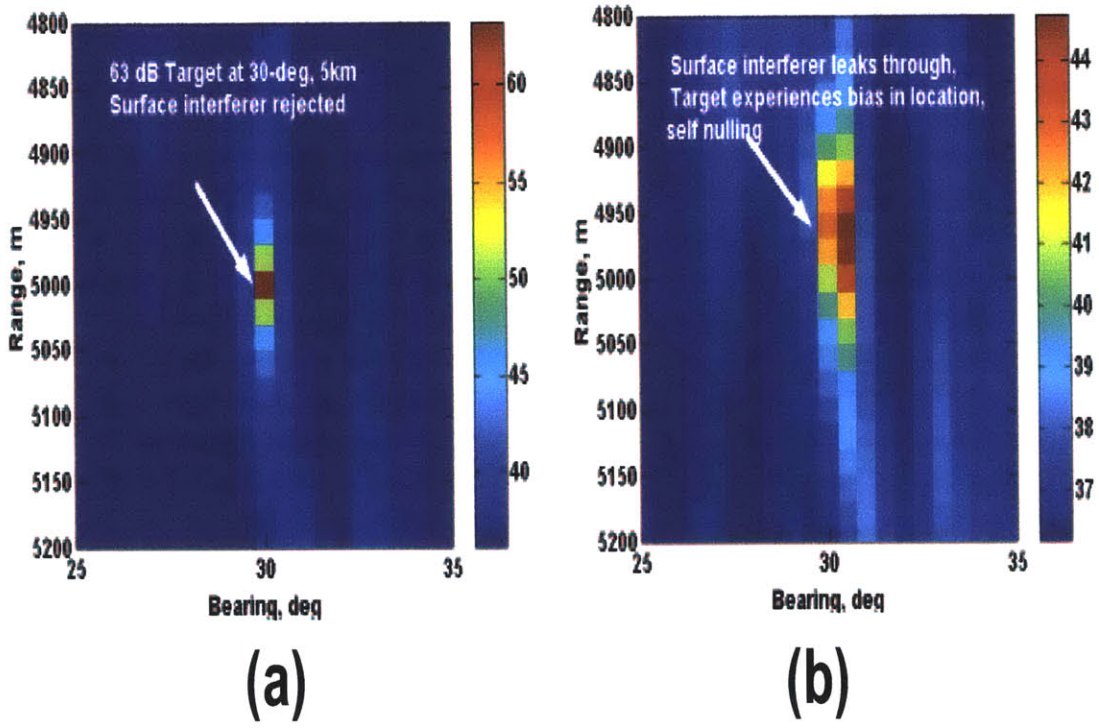

Figure 3-4: Ambiguity surfaces generated using the true SVP (L) and the assumed SVP (R). The mismatch in SVP leads to self-nulling and inability to discriminate the target from the surface interferer.

[36], [29]. This comes in the form of poor environmental knowledge which can lead to target self-nulling, and limited snapshot support that leads to the inability to perform adaptive processing, all discussed above. As a result, MVDR and direct MVDR variants relying on sample matrix inversion are nearly impossible to implement. One solution is to reduce the dimensionality of the problem by applying adaptive algorithms in beam space. Even then, implementation can be difficult when preserving resolution of large arrays. To overcome these challenges, several so-called *ad hoc* algorithms have been developed to enable adaptive processing in snapshot-starved or snapshot deficient environments. Additionally, these methods can also reduce the sensitivity of the estimator in terms of mismatch either in look-direction or in signal modeling (*i.e.* environmental uncertainty). This is particularly important for the passive sonar problem since the target of interest is in the data.

Perhaps the simplest work-around is a method known as diagonal loading [32], [36], [37]. This algorithm adds a small number to the diagonal of the sample covariance matrix prior to inversion. The adaptive weights are then computed based on the augmented SCM and applied to the original SCM as shown in the equations below. The diagonal load level is denoted by δ.

$$\tilde{K} = \frac{1}{L} X X^H + \delta I \tag{3.23}$$

$$\mathbf{w_{dl}} = \frac{\tilde{\mathbf{K}}^{-1}\mathbf{v}}{\mathbf{v^H}\tilde{\mathbf{K}}\mathbf{v}} \tag{3.24}$$

By adding diagonal loading, $\tilde{K}$ is full rank and hence, invertible, allowing implementation of MVDR even when data snapshots are limited. The drawback to this method, however, is that the estimator is effectively adding noise to the data in the weight vector computation. This does two things; it creates a bias in the estimator, and it decreases the nulling capability of the algorithm. While poor nulling is bad for interference cancellation, it does reduce self-nulling. Diagonal loading can be applied in other variants of MVDR in exactly the same way, and is used often in practice.

The level of diagonal loading applied to the beamformer is another parameter

in the implementation of the algorithm. Sometimes a constant load level is applied for all look directions. This is referred to as constant diagonal load. Other times, diagonal load level is dependent upon the direction of interest. This implementation is referred to as diagonal loading with a white noise gain constraint [32]. Under the White Noise Gain Constraint (WNGC) the white noise gain of the system is limited to be less than or equal to N, the number of sensors. This results in greater diagonal load level being applied to signal-like responses in the look direction so as to prevent self-nulling, and lower load levels applied to noise-like levels to improve nulling. In any application of diagonal loading there is a trade-off between aggressiveness of nulling and target protection.

Another class of ad hoc algorithms was developed by Owsley and extended in [38], [39], and is known as Dominant Mode Rejection (DMR). In DMR the dominant, or high power components are retained and low-poorly estimated eigenvalues are averaged. Therefore, only dominant modes are saved and used to null interference. Again, this method is based on augmenting the sample covariance matrix. Let

$$\hat{K} = \frac{1}{L} X X^H = \sum_{i=1}^{min(L,N)} \lambda_i \phi_i \phi^H i \tag{3.25}$$

be the sample covariance matrix in its eigenvalue/eigenvector representation. L is the number of snapshots and N is the number of sensors, as is convention. The SCM has $\min(L, N)$ non-zero eigenvalues. In DMR the sample covariance is formed by augmenting the dominant subspace to become

$$\tilde{K} = \sum_{i=1}^{J} \lambda_i \phi_i \phi_i^H + \sum_{i=J+1}^{N} \alpha \phi_i \phi_i^H \tag{3.26}$$

where the J largest eigenvalues and associated eigenvectors are saved, and alpha is the average of the remaining N-J eigenvalues. As in the case of diagonal loading, the weights are computed from this augmented SCM. The question remains as to the choice of "dominant" eigenvalues. In [38] the authors suggest the criterion be set such that eigenvalues which exceed a specified fraction of the power in the matrix are

retained.

DMR can also be formulated [38] to protect against target self-nulling by eliminating eigenvectors with low mismatch to the hypothesized target direction (*i.e.* 3dB) from the adaptive weight computation. This prevents the processor from nulling target-like signals. Finally, diagonal loading can also be applied in conjunction with DMR, either with a constant load level or with a white noise gain constraint to increase robustness.

3.6 Subarray Processing

3.6.1 Motivation for Subarray Processing

The background provided thus far in this thesis has presented several challenges to processing large aperture arrays.

1. Limited spatial coherence of signals is typically much less than the length of large aperture arrays, limiting the aperture over which coherent processing is efficient.

2. Conventional processing allows for high sidelobe leakage in interference-dominated environments, motivating the need for adaptive methods

3. Snapshot support requirements for large arrays are high and snapshot availability is low due to the increased resolution of long arrays of many sensors

4. Mismatch loss either in the propagation model or as a result of coherence degradation leads to target self-nulling and poor detection performance.

The authors in [4] demonstrated that incoherent subarray processing led to detection performance improvement and achieved performance comparable to that of the optimum clairvoyant processor in a coherence-limited environment containing a signal and white noise only. They demonstrated that balancing coherent gain from processing coherent apertures coherently and incoherent apertures noncoherently led

to near optimum performance. So, for the problem of detecting a single signal in white noise in a coherence-limited environment, incoherent subarray processing outperforms full-array processing. In an interference-dominated environment, however, the limited resolution of an incoherent subarray processor may cause detection performance to suffer. The need for adaptive processing becomes emphasized, and snapshot support in covariance estimation becomes the dominant issue. While subarray processing may help mitigate signal gain degradation in an interference-dominated environment, it also offers a method of improving the ratio of snapshots to adaptive degrees of freedom while maintaining performance near optimum as will be shown in Chapter 5. So, for the interference-dominated environment of interest, it is the snapshot support problem which dominates subarray partitioning strategy, while in the case of a signal in white noise, it is the coherence environment which dominates subarray selection.

To further motivate subaperture processing as a technique for overcoming these challenges, it is instructive to examine the optimum processor. As mentioned above, the performance metric used in this thesis is the probability of detection under a constant probability of false alarm (P_f). This probability of detection is determined through a binary likelihood ratio hypothesis test. Likewise, the optimum processor for this detection problem forms a binary likelihood ratio test on the data itself, conditioned on known ensemble covariance matrices. In practice these covariances are not known a priori, but must be estimated from the data. Examining the optimum processor, however, conditioned on known covariances, leads to useful insights.

The optimum processor, as defined here, is that based solely on a LRT applied to the array data snapshots. As seen in section 3.3, the *pdf* of the array snapshots is needed to form the LRT. Since the snapshots are Gaussian, the covariance matrix of the snapshots is needed. In this "optimum" analysis, it is assumed that the true, or clairvoyant, covariance matrices for the data, under each hypothesis, are known. This is clearly a poor assumption for a realistic scenario, yet this analysis will provide a measure of the "best-case" performance.

The formulation begins with the *pdf* of snapshots conditioned on each hypothesis.

$$p_{x|H_1}(\mathbf{x}|H_1) \sim CN(0, K_1) \tag{3.27}$$

and

$$p_{x|H_0}(\mathbf{x}|H_0) \sim CN(0, K_0) \tag{3.28}$$

with the expressions for the complex normal density given by equation 4.5.

In order to implement a likelihood ratio test, it is useful to whiten the data. In that case, the data can be expressed in terms of a set of common eigen-vectors. Whitening is performed by filtering the snapshots with the inverse square root of the covariance K_0. Let $\mathbf{z}$ be the whitened snapshots.

$$\mathbf{z} = K_0^{-\frac{1}{2}}\mathbf{x} \tag{3.29}$$

The conditional *pdfs* of $\mathbf{z}$ are then

$$p_{z|H_1}(\mathbf{z}|H_1) \sim CN(0, \tilde{K}_1) \tag{3.30}$$

and

$$p_{z|H_0}(\mathbf{z}|H_0) \sim CN(0, \tilde{K}_0) \tag{3.31}$$

respectively with

$$\tilde{K}_1 = K_0^{-\frac{1}{2}} K_1 K_0^{-\frac{1}{2}} \tag{3.32}$$

and

$$\tilde{K}_0 = K_0^{-\frac{1}{2}} K_0 K_0^{-\frac{1}{2}} = I. \tag{3.33}$$

A LRT is then constructed using the whitened data, z.

$$\Lambda = \frac{p_{z|H_1}(\mathbf{z}|H_1) >}{p_{z|H_0}(\mathbf{z}|H_0) <} \eta \tag{3.34}$$

Substituting the complex normal *pdf*, the LRT becomes

$$\Lambda = \frac{|\tilde{K}_0|}{|\tilde{K}_1|} e^{-\mathbf{z}^H(\tilde{K}_1^{-1}-\tilde{K}_0^{-1})\mathbf{z}} \underset{<}{\geq} \eta. \tag{3.35}$$

Taking the natural logarithm of both sides and absorbing the deterministic determinant terms into the threshold term we obtain

$$l = \mathbf{z}^H \tilde{K}_0^{-1}\mathbf{z} - \mathbf{z}^H \tilde{K}_1^{-1}\mathbf{z} \underset{<}{\geq} \gamma \tag{3.36}$$

where l is the sufficient statistic. Recognize that $\tilde{K}_0$ is the identity matrix and that $\tilde{K}_1$ is the sum of the identity matrix and a whitened signal covariance matrix. As a signal decorrelates, the off-diagonal terms of $\tilde{K}_1$ diminish. Therefore, as the coherence length decreases, $\tilde{K}_1$ may be approximated by a block-diagonal matrix. This results in the second term in equation 3.36 as an incoherent sum of coherently-processed array sections, indicating that subarray processing in coherence-limited environments is an approximation to the optimum processor. Note also that this processor forms a quadratice term resembling a power estimate ont eh data. That indocates that the power estimate from a subarray processormay be the important "datum" which could then feed into a binary LRT. As will be seen in the next chapter, the *pdfs* for the CTA and AI algorithms are complex chi-squared. The ratio of their *pdfs* under the signal present and signal absent hypotheses depend only on an exponential function with the power estimate as an argument. Therefore, in forming the binary LRT, the detection statistic becomes the power estimate. For consistency, the power estimate is used as the sufficient statistic for all algorithms examined.

In summary, subarray processing is an attractive technique for mitigating the challenges of large array processing for several reasons.

1. Subapertures can be chosen such that signals are coherent over the partitions, allowing efficient coherent processing

2. Adaptive processing can be applied within or across subarrays, thus reducing the dimensionality of the adaptive stage, hence the requisite snapshot support

3. The decreased resolution of an individual subarray may help mitigate target self-nulling

The remainder of this thesis examines the statistical detection performance of three adaptive subarray algorithms; the Conventional-then Adaptive (CTA), the Adaptive-Incoherent (AI), and the Adaptive-then-Conventional (ATC). These algorithms are formulated without any of the robustness techniques outlined in sections 3.1 and 3.2 so that the statistics may be determined without employing numerous Monte Carlo simulations. The analysis to follow leads to several insights as to algorithm selection and subarray partitioning which may then be applied to array design.

The remainder of this chapter is organized as follows. First, a discussion of potential subarray partitioning schemes is presented, and the reasoning behind the choice of non-overlapping configurations is given. Next a brief table of notation used in the analysis to follow is provided. Finally, the CTA, AI, and ATC algorithms are introduced.

3.6.2 Subarray Partitioning Schemes

There are several possibilities for subarray partitioning. Subarrays may be non-overlapping, overlapping, or interleaved. Figure 3.5 shows three such examples of subarray partitioning schemes for a two-streamer array. Each shape represents an element of a subarray.

The non-overlapping configuration is shown in Figure 3.5a. In this case, signals of interest are typically coherent across the subaperture, if chosen appropriately, and, for low-coherence lengths, subarrays may be essentially uncorrelated. This simplifies the statistics of several subarray algorithms. For this reason, the subsequent analysis is limited to non-overlapping subarray configurations. One drawback to this method is that in processing subarrays coherently, one may encounter grating-lobes since the distance between subarray-center to subarray-center may be significant.

The overlapping configuration (Figure 3.5b) results in subarrays which are correlated, at least to some degree, since elements in the array may belong to more than

one subarray. The benefit to an overlapping configuration, however, is that grating lobes resulting from coherent processing of subarrays may be avoided.

Both the non-overlapping and overlapping configurations reduce the effective aperture of a given subarray. The subarray is much smaller than the full array. While this may benefit processing in low coherence environments, it sacrifices resolution when signals are coherent across the full aperture. A third configuration, interleaved subarrays shown in Figure 3.5c, retains the resolution of the full array, but results in grating lobes if there are too many subarrays (elements are spaced several wavelengths apart rather than one-half wavelength). The interleaving approach also leads to subarrays which tend to be correlated which complicates the statistics of the adaptive subarray algorithms. Because of this, the non-overlapping configurations are used in the remainder of this thesis.

3.7 Subarray Algorithms

Three subarray processing algorithms are presented here. The algorithms themselves have appeared in the literature, and have been used in practice. The statistics of these algorithms, however, have not been studied. Furthermore, there has not been a statistical performance analysis of these algorithms implemented using large aperture arrays in a coherence limited environment. The three algorithms are the Conventional-Then-Adaptive (CTA) algorithm, the Adaptive Incoherent (AI) algorithm, and the Adaptive-then-Conventional (ATC) algorithm. These algorithms divide the adaptive degrees of freedom differently, have different resolution capabilities, and require varying amounts of snapshot support.

At this point, it is important to make a distinction between beamformer output and processor output. This thesis refers to beamformer output as the result of the inner product between a weight vector and a data vector. This is a complex, scalar quantity. Processor output is a power estimate. This is the result of pre- and post-multiplying a covariance matrix by a weight vector. The result is a real scalar quantity.

All of the algorithms below begin with a NxL sample data matrix X, the columns

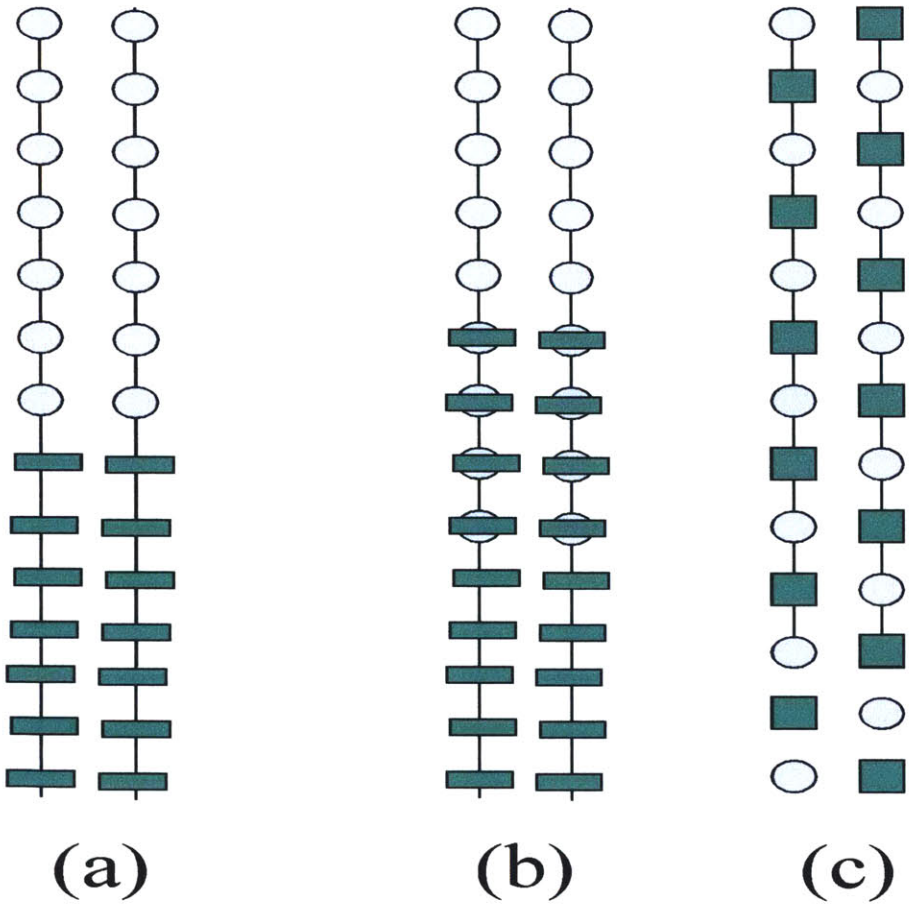

Figure 3-5: Various potential subarray configurations.

of which are data snapshots.

$$X = [\mathbf{x^1 x^2 \cdots x^L}] \tag{3.37}$$

Conventional-Then-Adaptive (CTA) Algorithm

This algorithm is a two-stage hybrid conventional-adaptive algorithm in which conventional weights (CBF or CMFP) are applied to each subarray and each snapshot at the first stage. This transforms the data into a "subarray" data matrix. Then MVDR processing is implemented on this subarray data.

First, the full-array steering vector is partitioned into M subarrays. Each of these vectors are normalized by the number of sensors in the subarray (*i.e.* the length of the subarray steering vector).

$$\mathbf{v} = \begin{bmatrix} \mathbf{v_1} \\ \mathbf{v_2} \\ \vdots \\ \mathbf{v_M} \end{bmatrix} \tag{3.38}$$

These are then arranged into an NxM weight matrix, A, which transforms the element-level data into subarray level data.

$$A = \frac{1}{N/M} \begin{bmatrix} \mathbf{v_1} & \underline{0} & \cdots & \underline{0} \\ \underline{0} & \mathbf{v_2} & \cdots & \underline{0} \\ \vdots & & \ddots & \vdots \\ \underline{0} & \cdots & \underline{0} & \mathbf{v_M} \end{bmatrix} \tag{3.39}$$

A new MxL subarray data matrix, Z, is then formed.

$$Z = A^H X \tag{3.40}$$

This is a new data matrix from which an Mx1 adaptive weight vector is formed. The steering vector used at this stage is a vector of ones since the phase between subarrays has been taken into account in the conventional stage. Note that each subarray is

steered to the same spatial location which is different from the transformation used in beamspace adaptive processing. This issue will be discussed in Chapter 5.

$$\hat{K}_{CTA} = \frac{1}{L} Z Z^H \tag{3.41}$$

and

$$\mathbf{w_{CTA}} = \frac{\hat{\mathbf{K}}_{\mathbf{CTA}}^{-1}\underline{1}}{\underline{1}^{\mathbf{H}}\hat{\mathbf{K}}_{\mathbf{CTA}}^{-1}\underline{1}} \tag{3.42}$$

The resulting power estimate is then

$$y_{CTA} = \mathbf{w}_{\mathbf{CTA}}^{\mathbf{H}}\hat{\mathbf{K}}_{\mathbf{CTA}}\mathbf{w} = (\underline{1}^{\mathbf{H}}\hat{\mathbf{K}}_{\mathbf{CTA}}^{-1}\underline{1})^{-1} \tag{3.43}$$

This algorithm reduces the rank of the sample matrix inversion from N, the number of sensors, to M, the number of subarrays. This drastically reduces the required snapshot support. It does, however, reduce the adaptive degrees of freedom. This results in a trade-off between snapshot support and DOF for nulling interference. One potential drawback of this algorithm is that the adaptive degrees of freedom are also reduced from N to M. In a coherence-limited environment, subarrays may be chosen such that discrete signals are coherent across the aperture. Caution should be used, however, since the adaptive portion of the algorithm operates across sub-apertures, which, in severe coherence environments, could be incoherent. The statistical analysis in Chapter 4 and results in Chapter 5 discuss that impact.

3.7.1 Adaptive Incoherent Algorithm (AI)

The AI algorithm implements the MVDR algorithm on each subarray to form power estimates from each subarray. These power estimates are then averaged, resulting in an overall power estimate. The implementation is described below.

Again, the processor begins with the sample data matrix. This matrix is then

partitioned into N/M x L data matrices for each subarray.

$$X = \begin{bmatrix} X_1 \\ X_2 \\ \vdots \\ X_M \end{bmatrix} \tag{3.44}$$

Similarly the full array steering vector is partitioned into N/M x 1 subarray steering vectors

$$\mathbf{v} = \begin{bmatrix} \mathbf{v_1} \\ \mathbf{v_2} \\ \vdots \\ \mathbf{v_M} \end{bmatrix} \tag{3.45}$$

The subarray sample covariance matrix, K_{ii}, is then formed to generate MVDR power estimate, $y_{MVDR,i}$ from each subarray. The resulting power estimates are then averaged (incoherent averaging).

$$\hat{K}_{ii} = \frac{1}{L} X_i X_i^H \tag{3.46}$$

$$y_{MVDR,i} = (v_i^H \hat{K}_{ii}^{-1} v_i)^{-1} \tag{3.47}$$

$$y_{AI} = \frac{1}{M} \sum_{i=1}^{M} y_{MVDR,i} \tag{3.48}$$

This algorithm reduces the rank of the sample covariance matrices from N to the number of sensors per subarray (N/M). The algorithm does require M sample matrix inversions, however. Since the number of flops required for a matrix inversion is on the order of R^3 where R is the rank of the matrix, the inversion computations are reduced from the order of N^3 to $\frac{N^3}{M^2}$. The greater the number of subarrays the greater the computational savings. The drawback is that the resolution of the processor is reduced to the adaptive resolution of a shorter array (*i.e.* the individual subarray).

By incoherently combining subarray output powers, however, the variance of the noise estimate may be reduced, which could improve detection capability.

3.7.2 Adaptive-Then-Conventional Algorithm (ATC)

The final algorithm in this performance analysis is the ATC algorithm. In this algorithm, MVDR beamforming is applied to each subarray, and the beamformed outputs are combined coherently, *i.e.* using conventional processing. This again reduces the dimensionality of the adaptive stage from N to (N/M) as in the AI algorithm. Further, adaptive processing is applied within a coherent subaperture. If the signals are coherent over more than a subaperture, the conventional processing at the second stage will allow further interference rejection, potentially outperforming the AI algorithm.

The algorithm begins again with the full array sample matrix by partitioning it into N/M x L subarray sample covariance matrices as in the AI algorithm. These are then used to compute adaptive subarray weight vectors. X_i, $\mathbf{v_i}$, and $\hat{K}_{ii}$ are defined above in equations 3.24, 3.25, and 3.26 respectively. Then

$$\mathbf{w_i} = \frac{\hat{\mathbf{K}}_{\mathbf{ii}}^{-1}\mathbf{v_i}}{\mathbf{v_i^H}\hat{\mathbf{K}}_{\mathbf{ii}}^{-1}\mathbf{v_i}} \tag{3.49}$$

These weights are then stacked to form a super-vector and applied to full array sample covariance matrix to obtain the ATC power estimate.

$$\mathbf{w_{ATC}} = \frac{1}{\mathbf{M}}\begin{bmatrix} \mathbf{w_1} \\ \mathbf{w_2} \\ \vdots \\ \mathbf{w_M} \end{bmatrix} \tag{3.50}$$

$$y_{ATC} = \mathbf{w_{ATC}^H}\hat{\mathbf{K}}\mathbf{w_{ATC}} \tag{3.51}$$

Similar to the AI algorithm, the ATC algorithm reduces the rank of the sample matrix inversion as well as the required snapshot support. It does not, however, reduce

the conventional resolution of the array since there is coherent processing of the full aperture. Further, it reduces sidelobes beyond that of AI leading to better interference rejection. As in the case of the CTA algorithm, the algorithm trades adaptivity for snapshot support. The CTA applies adaptivity across subarrays while the ATC applies adaptivity within subarrays. The case, however, when each element is treated as a subarray, the CTA algorithm reduces to the ATC algorithm for one subarray. That is the CTA with M=N is identical to the ATC algorithm when M=1 (and also the AI algorithm for M=1, as this is full array adaptive processing). Similarly the ATC algorithm for the case M=N is equivalent to the CTA algorithm for the case M=1 (*i.e.* Conventional processing of the full array). These limiting cases will be discussed in Chapter 4.

3.8 Summary

This chapter has provided an overview of the challenges associated with adaptive processing as well as common algorithms. Several analytical algorithms have been presented which attempt to mitigate some of the challenges of adaptive array processing via subarray methods. The remaining chapters of this thesis present original work in the performance analysis of these subarray algorithms as well as a study of the the effects of limited coherence and snapshot support on subarray processing. Among the results is a set of guidelines for optimal partitioning for a give set of coherence and snapshot conditions.

There are two main issues which are pervasive throughout the rest of this thesis.

1. Adaptive DOF vs Snapshot support - In an interference field, certain adaptivity is required to null interference, but greater adaptive DOFs require more snapshot support. There is then a trade-off between SCM conditioning at the adaptive stage and adaptivity.

2. Adaptive resolution vs subarray configuration - There is a performance difference between adaptivity spread across a large aperture (across subarrays) and

These issues will be studied in detail in Chapter 5.

It is important to note that the three subarray algorithms presented in this chapter can be used in conjunction with ad hoc methods of section 3.5.3. When implemented in practice, diagonal loading is used particularly often. If rank reduction beyond that provided through subarray partitions is needed, techniques such as DMR may be used as well. Since the focus of this research is to understand the physical significance of the statistics of these algorithms, the algorithms will be analyzed without the used of these *ad hoc* techniques. Algorithm performance with these techniques is left to future work.

Chapter 4

Statistical Analysis of Subarray Algorithms

The first three chapters of this thesis provide an overview of large, 2D-aperture array processing for passive sonar detection. Chapter two showed that large arrays provide high resolution and excellent interference rejection when the propagation environment is well known, particularly when using a full-wave propagation model as with MFP. In a realistic environment, however, there are several performance-degrading mechanisms, several of which are detailed in section 2.3. The remainder of this thesis examines subarray processing as a method of mitigating two predominant problems with passive detection using large arrays:

1. Limited spatial coherence of both signals and interference

2. Limited stationarity intervals leading to finite snapshot support

This chapter derives statistical models for evaluating the detection performance of the subarray processing algorithms presented in Chapter 3. This analysis incorporates the effects of both snapshot support and limited spatial coherence. Performance analysis of these algorithms could be obtained through running many Monte Carlo simulations, yet that approach is both cumbersome and time-consuming. The analysis presented in this chapter employs several simplifying assumptions in order to get

analytical approximations to the performance of subarray processing algorithms which are sufficient for array partitioning guidelines and algorithm selection. Chapter 5 then uses the analyses presented here to gain insight into optimum array partitioning schemes using both plane-wave and full-wave propagation applied to both linear and planar towed arrays.

This chapter is structured as follows. As shown in Chapter 3, the fundamental element of the likelihood ratio test as cast here is the probability density function of the subarray-beamformed power estimate. This chapter begins with a survey of the relevant literature in the statistical analysis of adaptive array processing algorithms. The remainder of this chapter presents a statistical analysis three subarray algorithms:

1. CTA - Conventional on the subarray The Adaptive across subarrays
2. AI - Adaptive on the subarray, Incoherently combine subarrays
3. ATC - Adaptive on the subarray Then Conventional across subarrays

and two baselines

1. Conventional Processor - full array coherent processing, non-adaptive
2. Optimum Processor - uses the data snapshots directly in a LRT assuming the ensemble covariances are known

The analyses presented here incorporate the effects of both signal and interference decorrelation as well as finite snapshot support.

4.1 Previous Work

Equations 3.8-3.10 are conditioned on known data covariance matrices. In general, these covariances are not known a priori. In practice, the maximum likelihood estimate of the covariance matrices, the Sample Covariance Matrix (SCM) is used. While this may seem to be an arbitrary solution to the problem of unknown ensemble covariance matrices, there is an extensive body of work behind it.

Kelly and Forsythe [18] derive an adaptive detection statistic for active radar or sonar using a generalized likelihood ratio test [41]. In their formulation, target-free data is available upon which one may estimate noise statistics. A generalized likelihood ratio test (GLRT) is used when some parameter in the data *pdf* is unknown. In this case the *pdfs* under H_o and H_1 are maximized over the unknown, nuisance parameters. This leads to the data *pdfs* evaluated using the ML estimate of the nuisance parameters in place of the clairvoyant parameters. In this case, the nuisance parameters are the covariance matrices and the signal amplitude. The ML estimate of the ensemble covariance matrix is the sample covariance matrix. The ML of the signal estimate is also shown to be the result of applying the MVDR weight vector based on target-free training data to the data under test.

One challenge to passive sonar, however, is that there is no target-free training data available. The target of interest, if present at all, will appear in all snapshots. As a result, algorithms such as the MVDR have been developed to minimize the variance of the output, i.e. the power, subject to a constraint that the signal of interest passes through undistorted. Again, since the data covariances are unknown, their ML estimates, the SCMs, are used in their place.

Adaptive array processing has been a very active field for the last thirty five years. Over this time, several performance analyses of adaptive array processors have appeared in the literature, both in terms of detection performance and as a parameter estimation problem. This is a broad area of study, so the references here are limited to those which are of particular relevance to the work in this thesis. Many of these performance analyses have been extended to the case of SCM-based algorithms including the effects of finite snapshot support. Further, there have been a number of proposed algorithms which attempt to compensate for the problem of limited spatial coherence of signals. The literature lacks, however, a unified analysis of subarray selection based on these two performance-degrading effects. The thesis seeks to fill that gap.

The adaptive algorithms studied in this thesis are all based on the MVDR algorithm. As mentioned, the true data covariances are seldom known so sample co-

variance matrices are used in their place. The statistics of these sample covariance matrices are then central to the analysis.

Goodman [42] proved that under the assumption that data snapshots are jointly Gaussian random vectors, the elements of the sample covariance matrix (SCM) are jointly complex Wishart distributed. In their landmark paper [7], Capon and Goodman extended this result to prove that the power estimate of the SCM-based MVDR processor has a complex chi-squared distribution with the degrees of freedom related to the number of snapshots and number of sensors. Since the Capon/Goodman work, this result has been derived using alternate formulations with the same result [6].

Subsequently much work has been done to extend this result. Steinhardt [6], [19] showed that the *pdf* of the elements of the MVDR weight vectors are linear transformations of the student's t distribution. Richmond [20] took this work a step further deriving the joint distribution of adaptive maximum-likelihood signal estimates for a multiple-signal case. Further, Richmond derived the *pdf* of many adaptive beamformers under a much broader class of data distributions, relaxing the assumption of Gaussian data. The published work to date, however, relates to full array processing. These analyses have not been applied to subarray processing. The main challenge in deriving statistics of multi-stage adaptive subarray processing algorithms, particularly the AI and ATC algorithms, is that the sample matrix inversions are applied only to certain partitions of the sample covariance matrix, rather than the entire SCM. As a result, the joint statistics of the inverses of correlated Wishart matrices are needed, and, in the case of the ATC algorithm, the joint statistics of both inverses and uninverted Wishart matrices are needed. The later sections of this chapter present methods for handling this analysis.

The analyses which appear later in this chapter leverage heavily off of the work of Capon and Goodman. Therefore, the results of the Capon/Goodman analysis are presented here for completeness.

4.1.1 Capon/Goodman Results

The Capon and Goodman present the statistics of a conventional beamformer. As in Chapter 3, the algorithms begin with a sample data matrix as given in equation 3.37. Similarly the conventional weights are given by

$$\mathbf{w}_c = \frac{1}{N}\mathbf{v}. \tag{4.1}$$

The asymptotic or clairvoyant power estimate is then given by

$$y_c = \mathbf{w}_c^H K \mathbf{w}_c \tag{4.2}$$

where

$$K = E\left[\mathbf{x}\mathbf{x}^H\right] \tag{4.3}$$

is the true or clairvoyant covariance matrix. The SCM based power estimate is then given by

$$\hat{y}_c = \mathbf{w}_c^H \hat{K} \mathbf{w}_c \tag{4.4}$$

where

$$\hat{K} = \frac{1}{L} X X^H \tag{4.5}$$

is the sample covariance matrix.

The linear function below then has a complex chi-square distribution. Note that in this thesis $\chi^2(L)$ refers to the complex chi-square distribution with L degrees of freedom.

$$\frac{L\hat{y}_c}{y_c} \sim \chi^2(L) \tag{4.6}$$

The *pdf* of the power estimate can then be found using derived distributions quite simply. The *pdf* of the SCM-based conventional processor is then given by

$$p_{\hat{y}_c}(\hat{y}) = \frac{\left(\frac{L}{y_c}\right)^L \hat{y}^{L-1} e^{-\frac{\hat{y}L}{y_c}}}{\Gamma(L)} \tag{4.7}$$

This is the pdf of the first benchmark, the conventional beamformer, hence the subscript c.

Capon and Goodman then derived the *pdf* of the MVDR power estimate. The SCM is given by $\hat{K}$ as defined above. The clairvoyant and SCM-based estimates are then given by

$$y_{mvdr} = (\mathbf{v}^H K \mathbf{v})^{-1} \tag{4.8}$$

and

$$\hat{y}_{mvdr} = (\mathbf{v}^H \hat{K} \mathbf{v})^{-1} \tag{4.9}$$

respectively, with $\mathbf{v}$ being the steering vector, per convention. The pdf of linear function shown below of the MVDR power estimate is then given by Capon and Goodman to be

$$\frac{L\hat{y}_{mvdr}}{y_{mvdr}} \sim \chi^2(L - N + 1) \tag{4.10}$$

under the condition that the number of snapshots exceeds the number of sensors in the array. Again, using derived distributions, the pdf of the MVDR power estimate is then given by

$$p_{\hat{y}_{mvdr}}(\hat{y}) = \frac{\left(\frac{L}{y_{mvdr}}\right)^{L-N+1} \hat{y}^{L-N} e^{-\frac{\hat{y}L}{y_{mvdr}}}}{\Gamma(L - N + 1)} \tag{4.11}$$

It should be noted that the power estimate using the SCM is a biased power estimate. If the number of snapshots, L, is less than the number of sensors, N, then the SCM is singular. When L is on the order of N, then there is a high bias and high variance, hence leading to poor detection performance. Subarray processing will reduce the dimensionality of the SCM which must be inverted from N to something less than N (i.e. N/number of subarrays for the ATC algorithm and number of subarrays for the CTA algorithm), improving the detection performance in snapshot-starved environments.

The above results are fundamental to the work of this thesis. First, equation 4.7 is the pdf of the conventional processor. This is the first benchmark, the performance of which all adaptive processors seek to exceed. Second, equations 4.8-4.11 form the foundation of the analysis of the adaptive stage of the subarray algorithms in

this thesis. We continue with the derivation of the second benchmark, the optimum processor.

4.2 Derivation of the Optimum Processor

Recall that the optimum processor, as defined here, is that based solely on a LRT applied to the array data snapshots and is conditioned on known covariances. Again, this is clearly a poor assumption for a realistic scenario but will provide a measure of the "best-case" performance. The beginning of the derivation appeared in Chapter 3 but is repeated here for convenience.

The derivation begins with the pdf of snapshots conditioned on each hypothesis.

$$p_{x|H_1}(\mathbf{x}|H_1) \sim CN(0, K_1) \tag{4.12}$$

and

$$p_{x|H_0}(\mathbf{x}|H_0) \sim CN(0, K_0) \tag{4.13}$$

with the expressions for the complex normal density given by equation 3.5.

The data is then whitened with $\mathbf{z}$ as the whitened snapshots.

$$\mathbf{z} = K_0^{-\frac{1}{2}}\mathbf{x} \tag{4.14}$$

The conditional pdfs of $\mathbf{z}$ are then

$$p_{z|H_1}(\mathbf{z}|H_1) \sim CN(0, \tilde{K}_1) \tag{4.15}$$

and

$$p_{z|H_0}(\mathbf{z}|H_0) \sim CN(0, \tilde{K}_0) \tag{4.16}$$

respectively with

$$\tilde{K}_1 = K_0^{-\frac{1}{2}} K_1 K_0^{-\frac{1}{2}} \tag{4.17}$$

and

$$\tilde{K}_0 = K_0^{-\frac{1}{2}} K_0 K_0^{-\frac{1}{2}} = I. \tag{4.18}$$

A LRT is then constructed using the whitened data, z.

$$\Lambda = \frac{p_{z|H_1}(\mathbf{z}|H_1)}{p_{z|H_0}(\mathbf{z}|H_0)} \underset{<}{\overset{>}{}} \eta \tag{4.19}$$

Substituting the complex normal pdf, the LRT becomes

$$\Lambda = \frac{|\tilde{K}_0|}{|\tilde{K}_1|} e^{-\mathbf{z}^H(\tilde{K}_1^{-1} - \tilde{K}_0^{-1})\mathbf{z}} \underset{<}{\overset{>}{}} \eta. \tag{4.20}$$

Taking the natural logarithm of both sides and absorbing the deterministic determinant terms into the threshold term we obtain

$$l = \mathbf{z}^H(\tilde{K}_0^{-1} - \tilde{K}_1^{-1})\mathbf{z} \underset{<}{\overset{>}{}} \gamma \tag{4.21}$$

where l is the sufficient statistic. This may be further simplified into an expression containing signal components. Recall that $\tilde{K}_0$ is the identity matrix (equation 4.18), and $\tilde{K}_1$ is the identity matrix plus a filtered, signal-only covariance matrix. The filtered signal covariance may be expressed in terms of its singular value decomposition as in [43].

$$\begin{aligned} \tilde{K}_1 &= \tilde{K}_s + I & (4.22) \\ &= U\Lambda U^H + I & (4.23) \end{aligned}$$

The columns of the matrix U are the signal eigenvectors and the matrix Λ is a diagonal matrix of eigenvalues. Therefore, the matrix $\tilde{K}_1^{-1}$ may be expressed in terms of its eigenvectors and eigenvalues.

$$\begin{aligned} \tilde{K}_1^{-1} &= \left(\tilde{K}_s + I\right)^{-1} & (4.24) \\ &= I - U(I + \Lambda^{-1})^{-1} U^H & (4.25) \end{aligned}$$

$$= I - \Sigma_{i=1}^{N} \left(1 + \frac{1}{\lambda_i}\right)^{-1} \phi_i \phi_i^{-1} \tag{4.26}$$

$$\tag{4.27}$$

The detection statistic may then be expressed as

$$l = \mathbf{z}^H (I - I + \sum_{i=1}^{N} (1 + \frac{1}{\lambda_i})^{-1} \phi_i \phi_i^{-1}) \mathbf{z} \tag{4.28}$$

$$= \sum_{i=1}^{N} \frac{\lambda_i}{\lambda_i + 1} \mathbf{z}^H \phi_i \phi_i^H \mathbf{z} \tag{4.29}$$

which is a weighted sum of the projection of the data on each signal eigenvector. This is analogous to a power estimate, as will be used in the performance analysis of the subarray algorithms in the later sections of this chapter.

The probabilities of detection and false alarm are then given by

$$P_d = \int_{\gamma}^{\infty} p_{l|H_1}(l|H_1) dl \tag{4.30}$$

and

$$P_f = \int_{\gamma}^{\infty} p_{l|H_0}(l|H_0) dl. \tag{4.31}$$

It is important to emphasize the assumptions inherent in this derivation thus far. First, these results are conditioned on knowing the ensemble covariances. This derivation is not based on the sample covariance matrices. This has been done so as to obtain a "best case" performance analysis with which to compare SCM based subarray algorithms. Second, this analysis has used the entire array data vector. The LRT implements the optimal processor, and hence I have not limited it by pre-processing the data in a perhaps, suboptimal way. Finally, the pdfs derived thus far have been for a single snapshot. Since snapshots are assumed to be independent, the joint pdf of L snapshots is the product of the pdfs of the individual snapshots. Since the snapshots are further assumed to be identically distributed, the joint pdf becomes that of a single snapshot raised to the L^{th} power. Next, the pdf of the LRT statistic, l, is needed.

Since the *pdf* of l is not immediately clear, it is useful to examine its moment generating function. Define the new detection statistic based on L snapshots the be the new varialble Ll and it moment-generating function is

$$\begin{aligned}
\Phi_{Ll|H_i}(s) &= E\left[e^{sl(\mathbf{z})}|H_i\right]^L && (4.32)\\
&= \left(\int_{-\infty}^{\infty} e^{s\mathbf{z}^H(\tilde{K}_0^{-1}-\tilde{K}_1^{-1})\mathbf{z}} p_{z|H_i}(\mathbf{z}|H_i)d\mathbf{z}\right)^L && (4.33)\\
&= \left(\int_{-\infty}^{\infty} \frac{1}{\pi^N|\tilde{K}_i^{-1}|} e^{-\mathbf{z}^H(\tilde{K}_i^{-1}-s(\tilde{K}_0^{-1}-\tilde{K}_1^{-1}))\mathbf{z}} d\mathbf{z}\right)^L && (4.34)
\end{aligned}$$

This integral is an integral over the complex plane and can be simplified by defining a new matrix Q by its inverse to be

$$Q^{-1} = \tilde{K}_i^{-1} - s(\tilde{K}_0^{-1} - \tilde{K}_1^{-1}). \tag{4.35}$$

Using this, the integral can be re-arranged to look like a ratio of determinants and the integral of a pdf of a complex normal random vector.

$$\begin{aligned}
\Phi_{Ll|H_i}(s) &= \left[\frac{|Q|}{|\tilde{K}_i|}\int_{-\infty}^{\infty} \frac{1}{\pi^N|\tilde{K}_i|} e^{\mathbf{z}^H\mathbf{Q}^{-1}\mathbf{z}} d\mathbf{z}\right] && (4.36)\\
&= \left[|\tilde{K}_i||Q^{-1}|\right]^{-L} && (4.37)\\
&= \left[|\tilde{K}_i(\tilde{K}_i^{-1} - s(\tilde{K}_0^{-1} - \tilde{K}_1^{-1}))|\right]^{-L} && (4.38)\\
&= \left[|I - s(\tilde{K}_i\tilde{K}_0^{-1} - \tilde{K}_i\tilde{K}_1^{-1}))|\right]^{-L} && (4.39)
\end{aligned}$$

Then, substituting $\tilde{K}_0 = I$ the moment generating function can be expressed as

$$\Phi_{Ll|H_i}(s) = \left[|I - s(\tilde{K}_i - \tilde{K}_i\tilde{K}_1^{-1}))|\right]^{-L} \tag{4.40}$$

The resulting conditional moment generating functions are then given by

$$\begin{aligned}
\Phi_{Ll|H_0}(s) &= \left[|I - s(I - \tilde{K}_1^{-1}))|\right]^{-L} && (4.41)\\
\Phi_{Ll|H_1}(s) &= \left[|I - s(\tilde{K}_1 - I))|\right]^{-L} && (4.42)
\end{aligned}$$

This moment generating function, in theory, could be inverted to obtain a pdf for the likelihood ratio statistic. To accomplish this, it is useful to express the determinant of a matrix as the product of its eigenvalues. Also, note that

$$\begin{aligned} \tilde{K}_1 &= K_0^{-\frac{1}{2}} K_1 K_0^{-\frac{1}{2}} && (4.43) \\ &= K_0^{-\frac{1}{2}} (K_s + K_0) K_0^{-\frac{1}{2}} && (4.44) \\ &= K_0^{-\frac{1}{2}} K_s K_0^{-\frac{1}{2}} + I && (4.45) \end{aligned}$$

where K_s is the signal-only covariance matrix, and not necessarily full rank. Hence, the eigenvalues of $\tilde{K}_1$ are then given by

$$\lambda_{1,i} = \lambda_{s,i} + 1 \tag{4.46}$$

with $\lambda_{s,i}$ being the eigenvalues of the whitened signal-only covariance matrix. Using this, the moment generating function of the likelihood ratio statistic conditioned on the null hypothesis is given by

$$\Phi_{Ll|H_0}(s) = \left[\prod_{i=1}^{N} (1 - \frac{s\lambda_{s,i}}{\lambda_{s,i} + 1}) \right]^{-L} \tag{4.47}$$

Note that this representation indicates that the poles of the moment generating function appear to lie in the Right Half Plane, but recall that the transformation to the moment generating function involves e^s rather than e^{-s} as in the Laplace Transform. At this point, it is useful to examine two different cases of signal coherence. When the signal is perfectly coherent, the signal covariance matrix will have a rank of 1. Alternatively, if the signal of interest experiences spatial decorrelation, the rank of the signal covariance matrix (or the signal subspace) will increase, essentially increasing the directional spectrum of the signal. This impacts the derivation of the optimum performance.

Coherent Signal Case

If the signal is perfectly coherent, it will have rank one, and hence, $\lambda_{s,i} = 0$ for $i > 1$. In this case, the moment-generating function of the likelihood ratio statistic is that of a complex chi-squared random variable with L degrees of freedom.

$$\Phi_{Ll|H_0}(s) = \left[1 - \frac{s\lambda_{s,1}}{\lambda_{s,1}+1}\right]^{-L} \tag{4.48}$$

Since this moment-generating function may be inverted analytically, there is an exact solution for the pdf given by

$$\begin{aligned} p_{\mathcal{L}|\mathcal{H}_i}(l|H_0) &= \frac{l^{L-1}e^{-\frac{l}{\lambda_s/(\lambda_s+1)}}}{\left(\frac{\lambda_s}{\lambda_s+1}\right)^L \Gamma(L)}, l > 0 & (4.49)\\ &= 0, l < 0. & (4.50) \end{aligned}$$

Similarly the pdf of the likelihood ratio statistic can be computed for the signal present hypothesis. Expressing equation 4.41 in terms of signal eigenvalues, the moment generating function becomes

$$\Phi_{Ll|H_1}(s) = (1 - s\lambda_s)^{-L} \tag{4.51}$$

leading to the pdf of the likelihood ratio statistic.

$$\begin{aligned} p_{\mathcal{L}|\mathcal{H}_1}(l|H_1) &= \frac{l^{L-1}e^{-\frac{l}{\lambda_s}}}{\lambda_s^L \Gamma(L)}, l > 0 & (4.52)\\ &= 0, l < 0. & (4.53) \end{aligned}$$

The above derivation provides analytical expressions for the probability density function of the likelihood ratio statistic of the optimum processor for the case of a rank one signal and (possibly decorrelated) interference. This analysis assumes that the true covariance matrices of the data are known under both the signal present and signal absent hypotheses. Interference decorrelation impacts the whitening stage of the processor in that the interference subspace becomes spread, potentially whitening

components of the signal which lie within the interference subspace. The chi-squared distribution is very common, tables have been generated computing both its probability density function and its cumulative distribution function (cdf), which is needed for determining error probabilities.

The probabilities of detection and false alarm have been defined in equations (3.9) and (3.10). It is useful to present a practical implementation of these calculations. Software programs, such as MATLAB, contain functions which compute these values rapidly. Using these functions, one may quickly compute the probability of detection for a constant false alarm rate. A MATLAB implementation of this is now presented.

The MATLAB Statistics Toolbox contains a routing $chi2cdf(x,\nu)$ defined as

$$\int_0^x \frac{t^{\frac{\nu-2}{2}}e^{-\frac{t}{2}}}{2^{\frac{\nu}{2}}\Gamma\left(\frac{\nu}{2}\right)}dt \tag{4.54}$$

If one defines

$$\sigma_0^2 = \frac{\lambda_s}{\lambda_s+1} \tag{4.55}$$

$$\frac{l}{\sigma_0^2} = \frac{t}{2} \tag{4.56}$$

then the probability of detection can be expressed as

$$P_f = \int_{\frac{2\delta}{\sigma_0^2}}^{\infty} \frac{t^{LP-1}e^{-t/2}}{2^L\Gamma(L)} \tag{4.57}$$

$$= 1 - chi2cdf\left(\frac{2\delta}{\sigma_0^2}, 2L\right) \tag{4.58}$$

where again, L is the number of snapshots. Using a similar analysis the probability of detection can be expressed as

$$P_d = 1 - chi2cdf\left(\frac{2\delta}{\sigma_1^2}, 2L\right) \tag{4.59}$$

where $\sigma_1^2 = \lambda_s$.

Using these expressions, the probability of detection for a constant false alarm

rate has a simple implementation. MATLAB also contains a function *chi2inv* which is simply the inverse of chi2cdf. If the false alarm rate is denoted by pf then

$$P_d = 1 - chi2cdf\left(\frac{\sigma_0^2}{\sigma_1^2} chi2inv(1-pf, 2L), 2L\right) \tag{4.60}$$

The probability of detection for a constant false alarm rate will be used as a figure of merit for comparing algorithm performance. The best possible performance for a given signal environment and snapshot support is given by this performance when the full array data is used.

Decorrelated Signal

While the above analysis provides very useful results, it is certainly possible that a scenario of interest includes a signal which has experienced some spatial decorrelation. In this case, the statistics become more challenging. The analysis above up through equation 4.49 is general, and still valid for the case of signal decorrelation. It is repeated below for convenience.

$$\Phi_{Ll|H_0}(s) = \left[\prod_{i=1}^{N}(1 - \frac{s\lambda_{s,i}}{\lambda_{s,i}+1})\right]^{-L} \tag{4.61}$$

If the source of interest experiences spatial decorrelation, it is no longer a rank one signal, and hence has more than one non-zero eigenvalue. Further, these eigenvalues may or may not be approximately equal, depending on the level of signal decorrelation. At this point, there are two ways to proceed. First, one could make some simplifying assumptions and attempt to express the moment generating function as that of a chi-squared distribution with a effective number of degrees of freedom. This approach has been used in spectral analysis [44]. A second option is to express the pdf of the LRT statistic as the convolution of several pdfs, each corresponding to a given eigenvalue. This method gives more accurate results than the effective DOF approach, but it requires significant computation. Alternatively, one could seek to find a bound on the performance rather than the exact performance, namely the Chernoff Bound [41], [45]. These three approaches are presented below.

Effective DOF Approach

As the signal decorrelates, the strength of the first eigenvalue decreases and the strength of the second eigenvalue increases, and eventually they become essentially equal. As the signal decorrelates further, a third eigenvalue gradually becomes more significant. In the limit as the signal completely decorrelates, the signal becomes rank N, essentially a "white" noise. Figure 4.1 shows this decorrelation process. The fractional strength of the first 7 eigenvalues of a 240 element signal correlation matrix are plotted vs the log of the coherence length in array lengths.

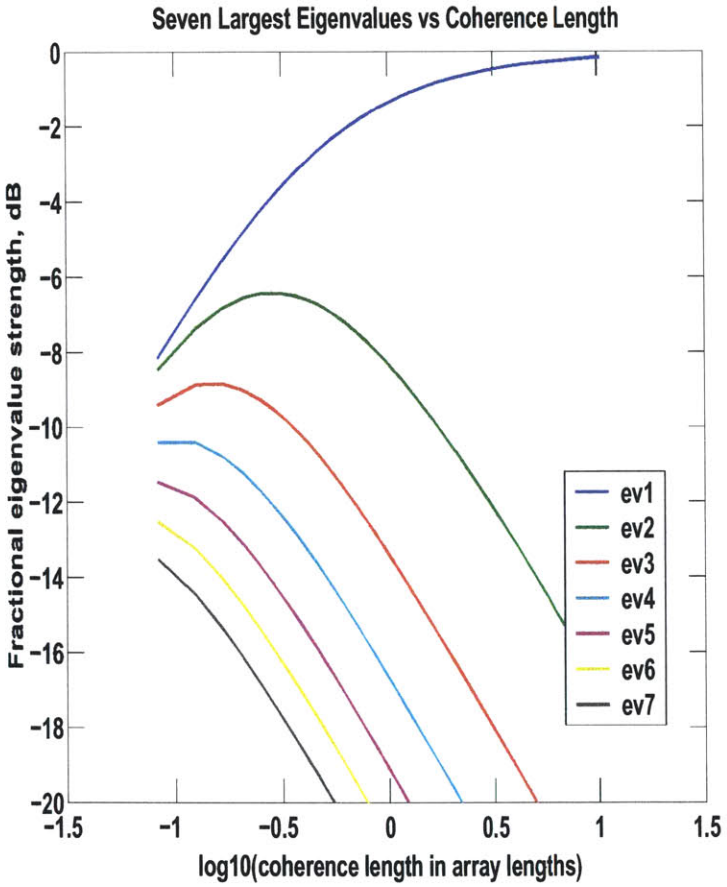

Figure 4-1: Eigenvalues vs coherence length of the signal for the seven largest eigenvalues.

One approach is to approximate the signal as being represented by the dominant P eigenvalues only. Further, one could assume that the dominant eigenvalues are

approximately equal. Then

$$\lambda_{s,i} \approx \lambda_{s,j} = \lambda_s \tag{4.62}$$

$$i \neq j \tag{4.63}$$

$$i,j \leq P \tag{4.64}$$

and hence the moment-generating function is then

$$\Phi_{Ll|H_0}(s) = \left[1 - \frac{s\lambda_s}{\lambda_s + 1}\right]^{-LP} \tag{4.65}$$

Again in this case, the pdf of the likelihood ratio statistic is that of a chi-squared random variable, but in this case, having LP degrees of freedom instead of simply L as before.

$$p_{\mathcal{L}|\mathcal{H}_i}(l|H_0) = \frac{l^{LP-1}e^{-\frac{l}{\lambda_s/(\lambda_s+1)}}}{\left(\frac{\lambda_s}{\lambda_s+1}\right)^{LP}\Gamma(LP)}, l > 0 \tag{4.66}$$

$$= 0, l < 0. \tag{4.67}$$

Similarly the pdf of the likelihood ratio statistic can be computed for the signal present hypothesis.

$$\Phi_{Ll|H_1}(s) = (1 - s\lambda_s)^{-LP} \tag{4.68}$$

leading to the pdf of the likelihood ratio statistic.

$$p_{\mathcal{L}|\mathcal{H}_\infty}(l|H_1) = \frac{l^{LP-1}e^{-\frac{l}{\lambda_s}}}{\lambda_s^{LP}\Gamma(LP)}, l > 0 \tag{4.69}$$

$$= 0, l < 0. \tag{4.70}$$

The question remains as to how to appropriately determine the number P. One common method is to examine the number of "degrees of freedom" (DOF) in the signal covariance matrix. Using the common expression for DOF in terms of eigenvalues is

given by [41]

$$DOF \approx round\left(\frac{(\sum \lambda_i)^2}{\sum(\lambda_i^2)}\right). \tag{4.71}$$

Finally, the eigenvalue must be chosen. Since the P dominant eigenvalues are not exactly equal (as seen in Figure 4.1), their average is used in place of λ_s.

Convolution Approach

The second approach to computing the detection performance when the signal has decorrelated is to work with inversion of the moment-generating function. We saw in the coherent signal analysis that the inversion of the moment-generating function with a single eigenvalue lead to the pdf in equations 4.49 and 4.52 respectively. Difficulty arises when there is more than one signal eigenvalue.

The key to this analysis is to realize that the moment-generating function is the product of N L^{th} order poles [46]. The pdf, then, is the convolution of the inverse transform of each of the terms in the product. This can be further simplified by noting that as the value of the signal eigenvalue becomes small, the pole moves away from the imaginary axis, and its transform approaches an impulse function. It is then intuitive to include only the dominant terms in the convolution.

The approach used here computes the inverse transform of the first terms in the product in equations 4.48 and 4.51. The convolution is performed numerically, and then the resulting pdf is normalized so it integrates to unity, again, numerically. These pdfs may then be integrated numerically to yield ROC curves.

This approach is more accurate than the effective DOF approach listed above, but becomes computationally inefficient when the signal decorrelation becomes severe. For moderate signal coherences, as in the case of greatest interest to this thesis, the convolution approach leads to strong agreement with theory with very using very few signal eigenvalues.

Chernoff Bound Approach

The third approach to performance analysis in the signal-decorrelation case is to derive the Chernoff Bound. The Chernoff bound has appeared in literature, and

leads to approximate expressions for the probabilities of detection and false alarm given below. A clear derivation of this appears in [41]. The Chernoff bound is computed by expressing P_F and $P_M = 1 - P_D$ in terms of a new variable with a "tilted" density. This new variable has a mean near the threshold at which one wants the ROC computed. This tilted density is used so that the CLT may be invoked with greater accuracy to tighten the bound.

The Chernoff Bound is based on $\mu(s)$, the natural logarithm of the moment-generating function of the LRT conditioned on the null hypothesis. Expressions for P_F and P_M are then:

$$P_F \leq \exp\left[\mu(s) - s\gamma\right] \tag{4.72}$$

$$P_M \leq 1 - \exp\left[\mu(s) + (1-s)\gamma\right] \tag{4.73}$$

where γ is the threshold. In order to make the threshold tight, one may minimize the bound with respect to s. This leads to the threshold becoming the first derivative of μ with respect to s, i.e. $\dot{\mu}(s)$.

These expressions are valid, then for values of s in the interval [0,1], and for cases when the threshold is to the left of the mean of the *pdf* of the LRT statistic conditioned on H_0.

These expressions can be further simplified by invoking at Central Limit Theorem argument, hence providing the justification for the tilted densities. Arguing that the test statistic is made up of a sum of many independent random variables, (i.e. many snapshots), one may derive tighter bounds on the performance given below.

$$P_f \approx e^{\mu(s) - s\dot{\mu}(s) + \frac{s^2}{2}\ddot{\mu}(s)} erfc_*(s\sqrt{\ddot{\mu}(s)}) \tag{4.74}$$

$$P_d \approx e^{\mu(s) + (1-s)\dot{\mu}(s) + \frac{(s-1)^2}{2}\ddot{\mu}(s)} erfc_*((1-s)\sqrt{\ddot{\mu}(s)} \tag{4.75}$$

The quantity $\mu(s)$ is the natural logarithm of the moment-generating function of

the likelihood ratio statistic conditioned on the null hypothesis. Altering the parameter s leads to computing the error probabilities at different thresholds.

For the problem of interest to here, one may compute $\mu(s)$ directly from the pdfs of the data as

$$\mu(s) = ln \int_{-\infty}^{\infty} [p_{y|H_1}(\mathbf{y}|H_1)]^s [p_{y|H_0}(\mathbf{y}|H_0)]^{1-s} d\mathbf{y} \tag{4.76}$$

with the pdfs of the whitened data given by equations 3.30 and 3.31. Then

$$\mu(s) = ln \int_{-\infty}^{\infty} \frac{1}{|K_1|^s |K_0|^{1-s}} \exp(-\mathbf{y}^H (sK_1^{-1} - (1-s)K_0^{-1})\mathbf{y} d\mathbf{y} \tag{4.77}$$

If we next specify a matrix Q such that

$$Q^{-1} = sK_1^{-1} + (1-s)K_0^{-1} \tag{4.78}$$

then the integral can be expressed as the pdf of a complex normal random vector with covariance Q. This results in

$$\begin{aligned} \mu(s) &= -ln(|K_1|^s |K_0|^{-s} |K_0||Q^{-1}|) && (4.79) \\ &= -ln(|K_1|^s |K_0|^{-s} |K_0||Q^{-1}|) && (4.80) \\ &= \sum_{i=1}^{N} (1-s) ln(\lambda_{s,i} + 1) - ln(1 + (1-s)\lambda_{s,i}). && (4.81) \end{aligned}$$

It is important to note (as seen in appendix A) that the Chernoff Bound is valid for values of s in the interval[0,1]. Therefore, the Chernoff Bound does not necessarily compute the entire Receiver Operating Characteristic (ROC) curve. The previous approximations based on the chi-squared densities do, and are therefore more useful for practical application, if the approximation is accurate.

Performance

Figures 4.2-4.4 demonstrate the performance of the models presented in this section and simulations implementing the optimum processor given in equation 4.21. In

all three figures, a single line array containing 240 sensors spaced 12.5m apart is used. The signal is modeled as a plane wave source at 50 Hz at a bearing of 90°, i.e. broadside. A plane wave model is used in all scenarios. Further, in all three figures, the interference is modeled as having experienced slight decorrelation, with a coherence length at the array of 250 element spacings ($\approx$ 1 array length). All examples use 50 snapshots in the data model. Recall that since this processor is conditioned on known covariance matrices, it is not necessary to use the SCM, and therefore not necessary for the number of snapshots to exceed the number of sensors. These plots show the Receiver Operating Characteristic (ROC) curve. This is the curve traces out of the Pd and Pf as the threshold of the LRT is varied.

Figure 4.2 shows a comparison of the ROC curve computed using the Chernoff Bound (in blue), the chi-squared DOF estimation model (green), and simulations (red) for the case of perfect signal coherence. There is an interferer at 90.3° with an element-level strength of 20 dB. The element-level target strength is 0 dB, and the white noise level is 0 dB. Recall that for the perfectly coherent signal case the DOF estimation algorithm is the exact analytical result (i.e. only one DOF in the signal covariance matrix). This plot therefore shows that the bound is tight in that it is essentially equal to the analytical result. The convolution approach is not shown here since there is only one signal eigenvalue. The convolution approach yields the same results as the effective DOF approach. Figure 4.3 shows the same interference scenario, this time with a target coherence length of 500 elements. In this case the Chernoff Bound does not encompass the full ROC. The DOF estimation does encompass the full ROC, and the agreement with simulation is fair. This is a stressing case for the effective DOF approach in that there is a very strong, in-beam interferer, and the processor is sensitive. The DOF model is very sensitive, and leads to slight degradation in performance. The convolution model is shown when only the largest two signal eigenvalues are included in the analysis. The results are more accurate than both the Chernoff Bound and the effective DOF model. Including more eigenvalues in the convolution produces little improvement.

Finally, Figure 4.4 demonstrates the performance of these models in a more re-

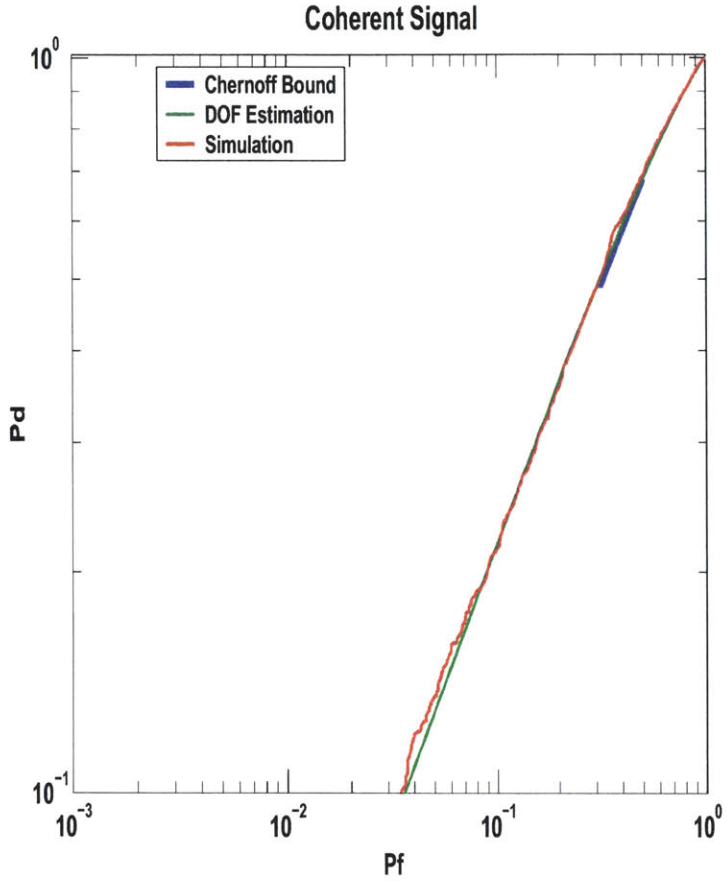

Figure 4-2: Comparison between the Chernoff Bound (blue), analytical ROC curve (green), and simulation (red) for coherent signal example.

alistic scenario. In this example, there is again a target at broadside, but there are 21 interferers scattered through the scene. The interferer signal levels and locations are provided in Table 5.1. In this case, the DOF model captures the statistics of the optimum processor very well. These interference-dominated cases are the cases of interest to this thesis. It is seen that in this case, the effective DOF model and the convolution model both provide strong agreement with simulation. Since there is no main-beam interferer, the effective DOF model performs well. Because of its computational simplicity and adequate performance, the DOF estimation model will be used to predict the optimum performance through the rest of this thesis. In general, as snapshot support increases, or adaptive rejection of interference improves,

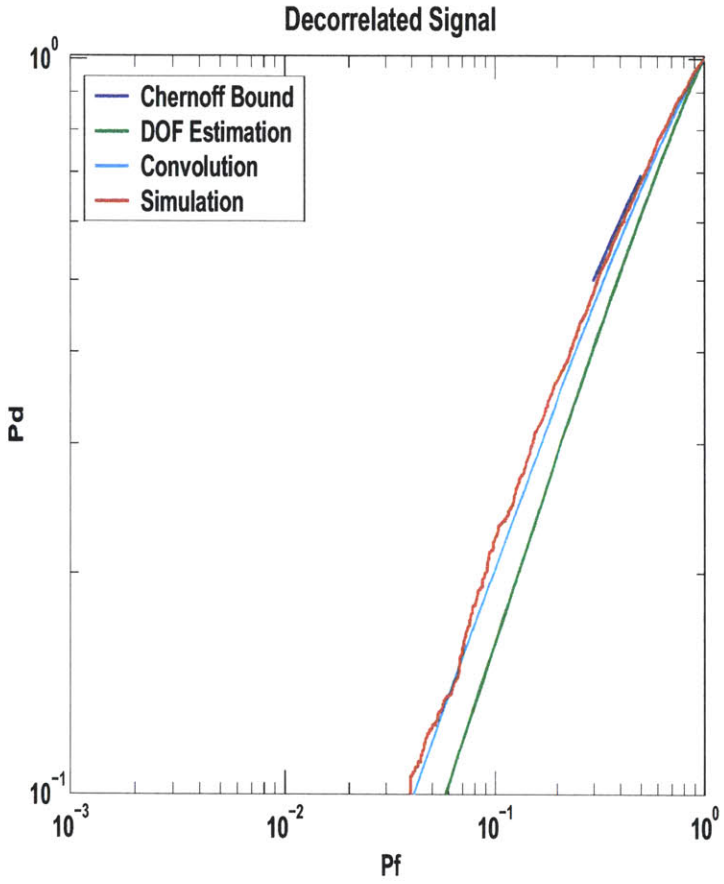

Figure 4-3: Comparison between the Chernoff Bound (blue), analytical ROC curve (green), Convolution model (cyan), and simulation (red) for target coherence length of 500 elements.

adaptive subarray algorithms may attain very close to this optimum performance

The statistics of the CTA Algorithm are presented next.

4.3 Conventional Then Adaptive Statistics

This section derives the detection performance performance of the Conventional-Then-Adaptive (CTA) algorithm. This derivation leverages heavily off of the Capon Goodman results, providing exact pdfs of the power estimates. There are two assumptions in this analysis:

1. Data snapshots are independent, identically distributed Gaussian random vec-

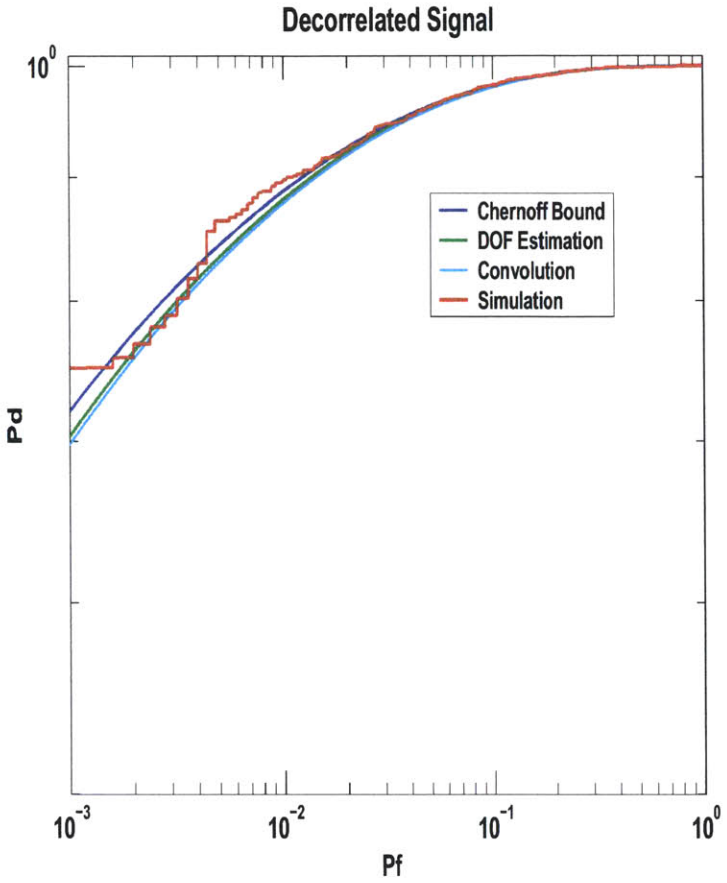

Figure 4-4: Comparison between the Chernoff Bound (blue), analytical ROC curve (green), convolution model (cyan), and simulation (red) for target coherence length of 500 elements, multiple interferer example.

tors. Since the random vectors are assumed to be identically distributed, the environment is assumed to be stationary.

2. The number of snapshots exceeds the number of subarrays.

CTA algorithm performs conventional beamforming at the first stage of processing. Begin with the full array sample matrix, X, as defined in equation (3.37). Since the snapshots are complex Gaussian random vectors, the distribution of the columns are zero mean with covariance K. An NxM matrix, A, is formed to perform the conventional stage of the algorithm, as defined in equation 3.39, with N being the number of sensors and M the number of subarrays. Recall that the columns of A

are simply normalized partitions of full array cbf steering vector. Therefore, each subarray is steered to the same physical location, Since the weights, and hence the matrix A, are deterministic, the new "data" matrix is still comprised of columns of complex normal, zero-mean, iid random vectors.

$$Z = A^H X \tag{4.82}$$

The columns of Z then have zero mean and covariance $A^H K A$. It is important to note that the dimensionality of Z has been reduced. Z now represents conventionally beamformed subarray outputs. The adaptive stage is then applied to this rank-reduced matrix.

The sample covariance matrix is then formed based on these snapshots.

$$\hat{K}_{cta} = \frac{1}{L} Z Z^H \tag{4.83}$$

Note that the outer product of the snapshot matrices has a complex Wishart distribution denoted as

$$Z Z^H \sim CW(M, L, A^H K A) \tag{4.84}$$

with the normalization of 1/L omitted. The power estimate is then identical in form to the Capon/Goodman estimator of equation (4.16).

$$\hat{y}_{cta} = (\underline{1} \hat{K}_{cta}^{-1} \underline{1})^{-1} \tag{4.85}$$

Note that the new steering vector is a vector of ones. This is because all "steering" was performed at the first stage, so all subarrays are now coherent. Now, defining the quantity z to be

$$z = \frac{L \hat{y}_{cta}}{P_{cta}} \tag{4.86}$$

where P_{cta} is the clairvoyant power estimate, Capon and Goodman give the pdf if z to be

$$p_Z(z) = \frac{z^{(L-M+1)-1} e^{-z}}{\Gamma(L - M + 1)}. \tag{4.87}$$

Using derived distributions, the pdf of the sample-based CTA power estimate is then given by

$$p_{Y_{cta}}(y) = \left(\frac{L}{P_{cta}}\right)^{L-M+1} \frac{y^{(L-M+1)-1} e^{-\frac{yL}{P_{cta}}}}{\Gamma(L-M+1)}. \tag{4.88}$$

This analysis is very straightforward, but is a new result in the context of subarray processing.

It is important to note that this analysis has relied on a general model for the data, specified only by the data covariance matrix. This, therefore, is valid for the coherence model presented in Chapter 2, as well as for any propagation model. The only limitations are that the data be complex Gaussian and the snapshots be independent. No limitation has been set on the propagation model or the data covariance matrix other than it must be full rank.

The detection framework for the performance analysis of these algorithms is the same posed in section 3.3. In this case, however, the "data" is the scalar power estimate rather than the data snapshots. In this case, with complex chi-squared pdfs, the power estimate becomes the sufficient statistic in the log-likelihood ratio test. Therefore, the pdf of the power estimate under the "signal present" and "signal absent" hypotheses is the basis for the probabilities of detection and false alarm.

$$P_f = \int_{\gamma}^{\infty} p_{Y|H_0}(y)dy \tag{4.89}$$

$$P_d = \int_{\gamma}^{\infty} p_{Y|H_1}(y)dy \tag{4.90}$$

where these random variables are the conditional power estimates.

Noting that the power estimates are linear functions of complex chi-squared distributions, it is possible to express these error probabilities in terms of MATLAB functions following the same procedure as in equations (4.56) - (4.62). The resulting expression for the probability of detection is then

$$P_{d,cta} = 1 - chi2cdf\left(\frac{P_{cta|H_0}}{P_{cta|H_1}} chi2inv(1-pf, 2(L-M+1)), 2(L-M+1)\right). \tag{4.91}$$

These expressions lead to efficient comparisons between the CTA algorithm and the optimum performance.

The expression for the *pdfs* of the power estimates and the detection probability are exact under the assumptions of independent, identically distributed Gaussian snapshots and full rank sample covariance matrices. Therefore, these expressions agree well with simulation as shown in the following figures. Since this thesis is primarily concerned with performance in interference-dominated environments, examples containing loud interference are used. In the following examples a common interference environment and array geometry are used. The array is a single line containing 240 sensors spaces 12.5 m apart, operating at 50 Hz. There is a target at 90^o (broadside) and an interferer at 90.3^o (the edge of the conventional beam). The element-level signals of the target and interferer are 0 dB and 20 dB respectively. There is 0 dB white noise, and a plane wave propagation model is used. In these examples, non-overlapping subarrays are use, although the analysis of this algorithm is equally valid for overlapping configurations as well.

Figure 4.5 demonstrates the detection performance as a function of the number of subarrays for a P_{fa} of 0.01. In this example the signal is perfectly coherent and the interferer has a high coherence length of 2500 elements (more than 10 array lengths). The blue curves are an example using 250 snapshots in the SCM and the red curves use 50 snapshots in the SCM. The solid lines correspond to the theory and the circles are the simulations. The simulations used 3000 independent realizations to compute the *pdfs* of the power estimates under each hypothesis, and the detection statistics are then computed from the *pdfs*. This figure demonstrates excellent agreement between theory and simulation, as expected.

Figure 4.6 again demonstrates the detection performance of the CTA algorithm as a function of subarrays, but in this case for an interferer coherence length of 50 elements (approximately 0.2 array lengths). The P_{fa} used in this example is 0.1. The detection performance for a P_{fa} of 0.01 agrees well with simulation, yet is very poor. Note also that while the optimum subarray configuration for this scenario is only a few subarrays, there is little performance difference between that case and

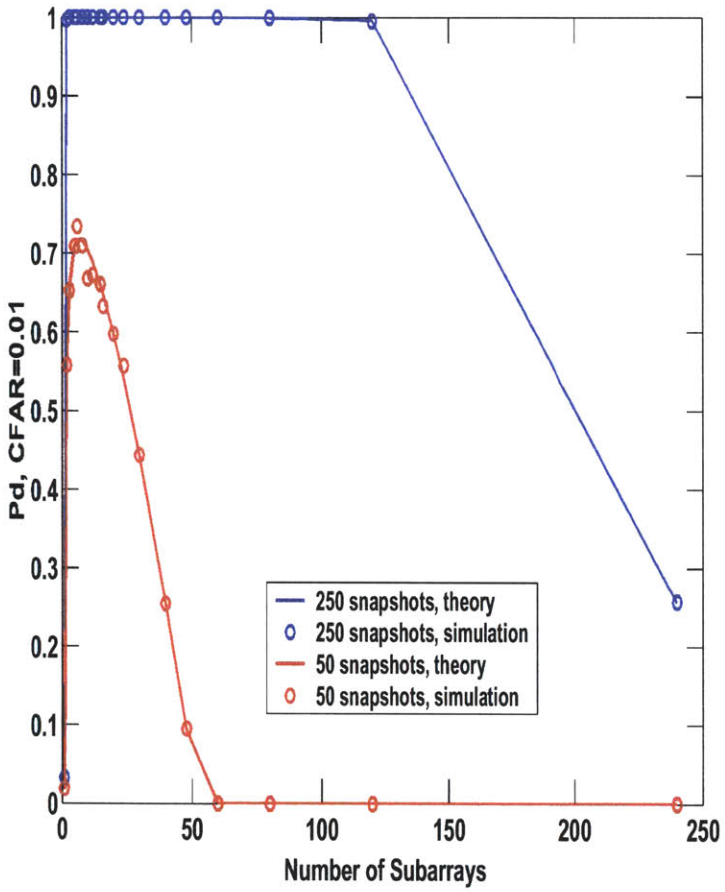

Figure 4-5: Comparison of simulated and analytical curves for CTA algorithm, interference-dominated example. Lcs=inf, Lci=2500 elements.

the full-array conventional processing (M=1). The blue curves again present results for a 250-snapshot scenario and the red curves a 50-snapshot scenario. Again, there is strong agreement between the theory and simulations. While not shown in these figures, the theory and simulations agree equally well when the target experiences spatial decorrelation as well.

There are a few comments that should be made at this point. First, there is clearly an optimal subarray configuration which varies with snapshot support and coherence. There is an inherent trade-off between number of subarrays (i.e. adaptive degrees of freedom) and snapshot support. If too many subarrays are chosen, then the high bias in the power estimates resulting from poor covariance estimates hamper detection.

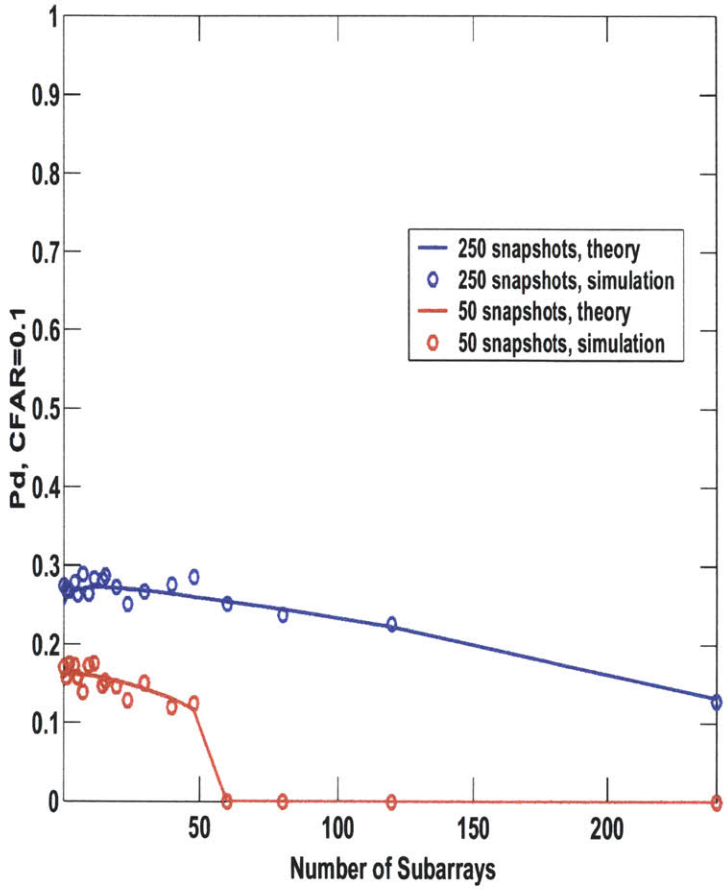

Figure 4-6: Comparison of simulated and analytical curves for CTA algorithm, interference-dominated example. Lcs=inf, Lci=50 elements.

If too few subarrays are chosen, there is insufficient adaptivity to suppress the interference, again resulting in poor detection performance. Further, as the interference decorrelates, more adaptivity is needed to null the spread interference, further stressing the trade-off between adaptivity and snapshot support. These trade-offs will be discussed in detail in Chapter 5.

The purpose of this section is to provide validation of the CTA analysis through comparison with simulations. The analytical results provided here for the CTA algorithm are exact, within the class of signal models used in this thesis. Their agreement with simulation validates both the analysis as well as the simulation method. The next section provides the analysis and validation for the AI algorithm.

4.4 Adaptive Incoherent Algorithm Statistics

As seen in section 4.3, analytical expressions for algorithm performance can be extremely helpful. This section derives the statistics of the Adaptive Incoherent algorithm. The AI algorithm also leverages off of the results of Capon and Goodman quite significantly. The algorithm begins by partitioning the sample data matrix into M partitions, where M is the number of subarrays as in equation (3.44). Similarly the steering vector is also partitioned into M components as in equation (3.45). These partitions are then used to form MVDR power estimates based on each subarray. The resulting power estimate is given by equation (3.48) repeated here for convenience.

$$\hat{y}_{ai} = \frac{1}{M} \sum_{i=1}^{M} \hat{y}_{mvdr,i} \tag{4.92}$$

The "hat" notation is again used here to emphasize that this estimate is based on a sample covariance matrix.

Based on the Capon/Goodman results, the pdf of each subarray power estimate, $\hat{y}_{mvdr,i}$ is known to be a linear function of a complex chi-squared random variable. The challenge arises from determining the pdf of the sum of these random variables.

At this point, some simplifications are made to reduce the complexity of the

problem. First, a solution is proposed for the case when the spatial coherence of the interference environment is very low. In that case, the following assumptions are made:

1. Data snapshots are independent, identically distributed Gaussian random vectors. Since the random vectors are assumed to be identically distributed, the environment is assumed to be stationary.

2. The number of snapshots exceeds the number of elements in a subarray

3. Each subarray power estimate is independent from the others. This is valid when the coherence is very low.

4. Subarray power estimates are identically distributed. This is valid when there is little fading across the array.

Under these assumptions, there exists an analytic solution to the pdf of the AI power estimate.

Let the subarray estimates be denoted as $\hat{y}_i$. Then

$$\hat{y}_{ai} = \frac{1}{M}\sum_{i=1}^{M} y_i \tag{4.93}$$

and the moment generating function of $\hat{y}_{ai}$ is then

$$\begin{aligned} \Phi(s) &= E\left[e^{s\hat{y}_{ai}}\right] && (4.94)\\ &= E\left[e^{\frac{s}{M}\sum \hat{y}_i}\right] && (4.95)\\ &= \prod_{i=1}^{M}\int_{-\infty}^{\infty} e^{\frac{sy_i}{M}} p_y(y_i)dy_i. && (4.96) \end{aligned}$$

Applying the fact that the subarray estimates are independent and identically distributed, then

$$\Phi(s) = \left[\int_{-\infty}^{\infty} e^{\frac{sy_i}{M}} p_y(y_i)dy_i\right]^M. \tag{4.97}$$

It is now useful to define the term N_s as the number of elements in a subarray. Now,

invoking the analysis of Capon and Goodman, the quantity

$$z = \frac{y_i L}{P_{mvdr,sub}} \tag{4.98}$$

is a complex chi-squared random variable with $L - N_s + 1$ degrees of freedom with $P_{mvdr,sub}$ being the clairvoyant output power. Again, using derived distributions, and the moment generating function of the complex chi-squared random variable, the moment generating function of the Ai power estimate is then given by

$$\Phi(s) = \left[1 - \frac{sP_{mvdr,sub}}{LM}\right]^{-M(L-N_s+1)}. \tag{4.99}$$

the moment-generating function of a chi-squared random variable with M(L-N+1) degrees of freedom. This moment generating function can then be inverted to give the pdf of the AI power estimate as

$$p_{\hat{y}_{ai}}(y) = \left(\frac{LM}{P_{mvdr,sub}}\right)^{M(L-N_s+1)} \frac{y^{M(L-N_s+1)-1} e^{-\frac{LM}{P_{mvdr,sub}}y}}{\Gamma(M(L-N_s+1)} \tag{4.100}$$

Again, using the same procedure as with he previous analyses, the probability of detection can be expressed in terms of the MATLAB functions *chi2cdf* and *chi2inv* as

$$P_{d,ai} = 1 - chi2cdf\left(\frac{P_{mvdr,sb|H_0}}{P_{mvdr,sb|H_1}}(1 - chi2inv(pf, 2M(L-N_s+1))), 2M(L-N_s+1)\right) \tag{4.101}$$

This analysis has assumed that the power outputs from each subarray are independent and identically distributed. That assumption is most valid when the subarray size is large compared to the coherence length. Figure 4.7 shows a comparison of this model to simulations. Again, a single line array of 240 sensors is used. There is a target at 90-deg and an interferer at 90.3-deg. The target and interferer have element-level signals of 0 dB and 20 dB respectively. The white noise level is 0 dB, and 250 snapshots are used in this model. In this case the target signal has decorrelated $L_{cs} = 50dy$ but the interference is relatively coherent $L_{ci} = 2500dy$. It is clear

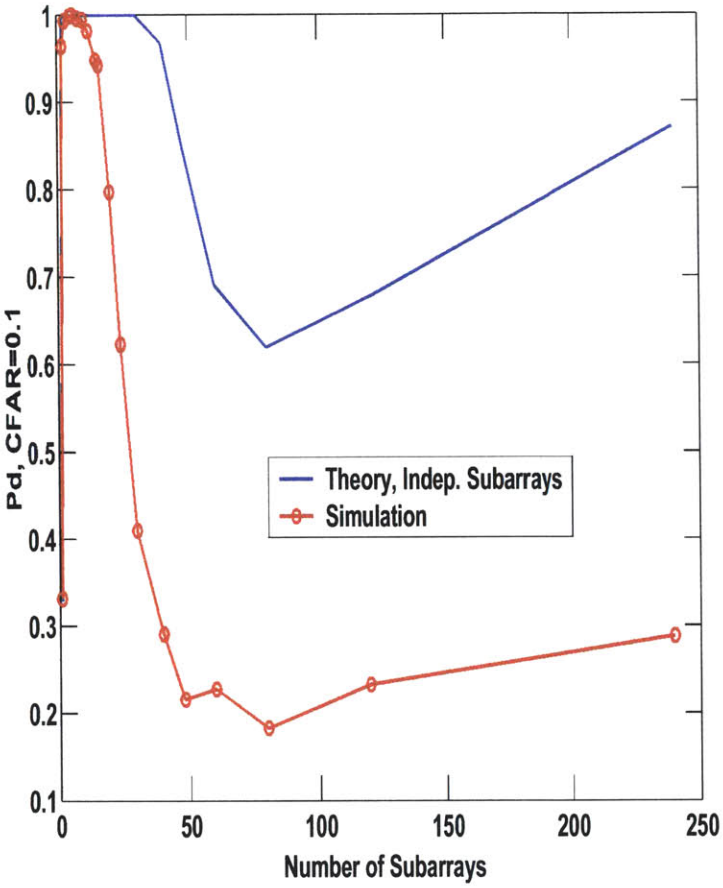

Figure 4-7: Comparison of simulated and analytical curves for AI algorithm, interference-dominated example. Lcs=50 elements, Lci=2500 elements.

from the figure that the agreement between the theoretical model and simulations is good for low numbers of subarrays (i.e. large subarrays) but degrades as subarrays get smaller. While not shown, the agreement is even worse for the case of a coherent signal and coherent or incoherent interference.

A more comprehensive model is needed to capture the effects of correlation between subarrays. We now present a new model which yields far better agreement with simulation for a a variety of cases, particularly the case of high signal coherence and low interferer coherence.

The proposed method recognizes that the degrees of freedom in the chi-square distribution is proportional to the number of subarrays. If, however, the subarray

output power estimates are correlated, true distribution will have fewer degrees of freedom. Therefore, one may model the pdfs as chi-squared distributions with an effective number of degrees of freedom. It is then necessary to devise a scheme for estimating the available degrees of freedom under each hypothesis.

The proposed estimation procedure is based on the transformation of array data to subarray data. Even though this algorithm processes the data on a subarray by subarray basis, one must determine the degree to which these subarrays are independent. Therefore, to estimate the available degrees of freedom, the first step is to transform array data to subarray data exactly as in the first step of the CTA algorithm. Second, form a covariance matrix based on subarrays. The degrees of freedom in this covariance matrix will then be used as the effective degrees of freedom in the subarray-processed data. The DOF estimation is preformed as in equation 4.71. This method will also take into account propagation effects in the modeled signal such as fading across the array, and range-dependent transmission loss as in the MFP case.

Figure 4.8 shows the comparison between the analytical expressions for the AI performance and the simulated performance as a function of number of subarrays. This is the same scenario as in Figure 4.8 with a third trace showing the improved performance of the effective DOF model.

The performance differences between these models may be explained in terms of the DOF estimation. The greater the DOF in the complex chi-squared model, the lower the variance of the *pdf*. Therefore, if the DOF are over-estimated (in the case of large numbers of subarrays and independence assumption) the model leads to *pdfs* with lower variances, and therefore better than true detection performance. Conversely, the effective DOF model leads to slightly poorer-than-true detection performance in the high subarray region. The agreement, however, between the new, effective DOF model and simulation is far better than the independent subarray approximation.

Figure 4.9 shows a comparison between the analytical expressions and simulation for a high coherence case. The array and source levels and locations are the same as in Figures 4.7 and 4.8. The target is perfectly coherent, and the interference has a

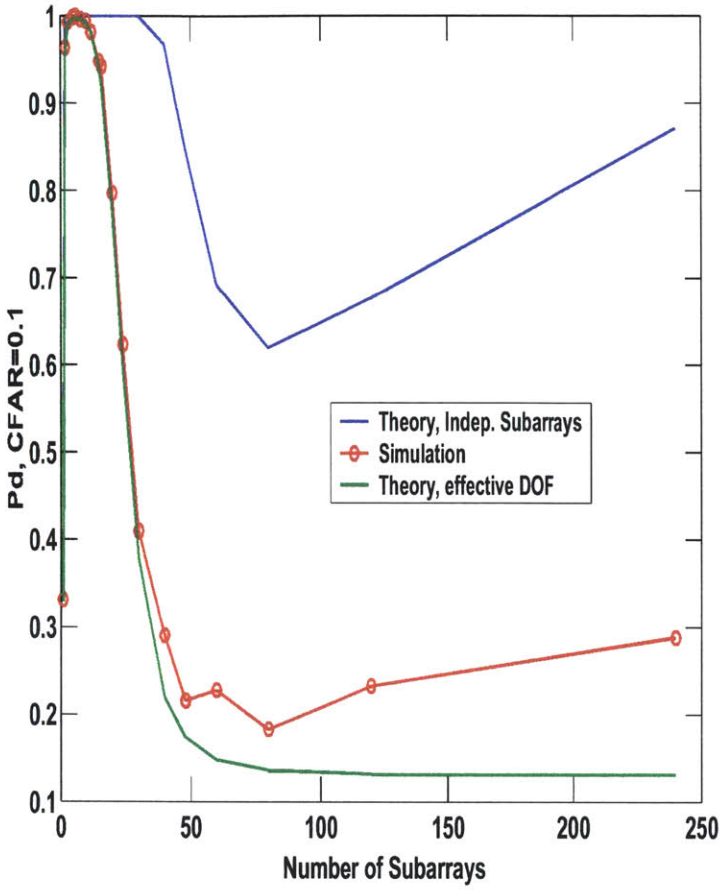

Figure 4-8: Comparison of simulated and analytical curves for AI algorithm, interference-dominated example showing improved model. Lcs=50 elements, Lci=2500 elements.

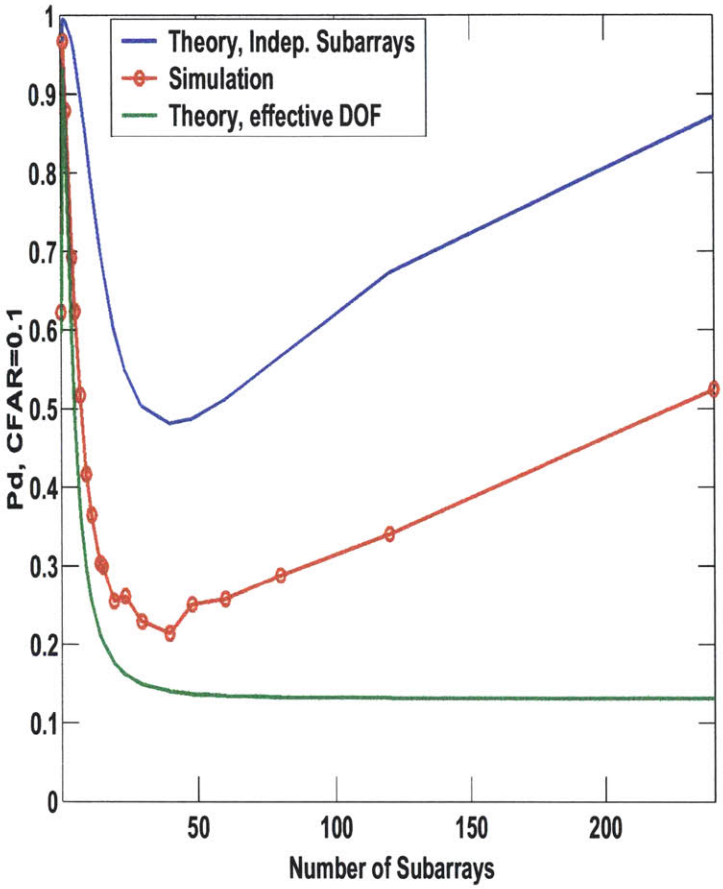

Figure 4-9: Comparison of simulated and analytical curves for AI algorithm, interference-dominated example showing improved model. Lcs=inf, Lci=2500 elements.

coherence length of 2500 elements. Again, the independence model over-estimates the DOF and the effective DOF model underestimates. In the high-detection performance region, however, the effective DOF model performs very well. From this point on, the performance of the AI algorithm will be modeled using the new, effective DOF model.

This section has derived the statistics of the AI algorithm which accounts for correlation between subarrays. The DOF estimation procedure proposed here provides excellent agreement with simulations when the number of subarrays is small to moderate (i.e. subarrays of substantial size). The model performs best when the target has experience some spatial decorrelation. The following section examines the statis-

tics of the final algorithm under study in this thesis, the Adaptive-then-Conventional algorithm.

4.5 Adaptive Then Conventional Algorithm Statistics

As seen in sections 4.3 and 4.4, the analyses of the CTA and AI algorithms leveraged strongly off of the Capon and Goodman work of [7]. The analysis of the CTA algorithm was straightforward by virtue of the fact that the algorithm broke down to processing linear-transformed Gaussian random vectors using the MVDR algorithm. The results of [7] were directly applicable. The AI algorithm applied the MVDR algorithm directly and simply summed the power outputs of each subarray. The effective-DOF approach worked well. The ATC algorithm, however, is more difficult. The first stage of the processor filters the data with a non-deterministic MVDR weight. These "beamformer outputs", i.e. not subarray powers, are then coherently combined. These beamformer outputs are not Gaussian, and therefore the statistical model is more complicated. This section presents an analysis of the problem using a Central Limit Theorem approach. The underlying assumption is that if the number of subarrays and/or snapshots is large, the power estimate may be assumed to be Gaussian, and therefore completely determined by its mean and variance.

The approach taken here is, rather than find the complete pdf of the ATC power estimate, seek its first and second moments. Then we seek conditions under which the central limit theorem may be invoked, and use that to predict detection performance. Even in deriving the first and second moments of the power estimates, it is necessary to make assumptions along the way. The following analysis takes two approaches. First, the problem is examined for the case of a 2-subarray partition, making use of the analytic expressions for a matrix inverse. It will be seen that this analysis leads to fair performance for what is terms a "low-energy coherence" case in which the discrete signals in the environment have levels well below the white noise level. This,

however, is not the problem of interest to this thesis. This thesis focuses on detection in an interference-dominated environment. Therefore a second approach is taken to approximating the first and second order statistics of the ATC power estimate, applying intuition and again leveraging off the Capon/Goodman work. This results in an analytical model which is valid for many interference-dominated scenarios.

The derivation begins with a look at the case of a 2-subarray partition. There exist several closed-form solutions for matrix inversions with a 2x2 partitioned matrix which facilitate the analysis. The results may then be extended to higher-order partitions.

The algorithm, as described in Chapter 3, begins by forming adaptive weights based on the sample covariance matrix of each subarray as in equation 3.49, repeated here for convenience.

$$\mathbf{w_i} = \frac{\hat{\mathbf{K}}_{\mathbf{ii}}^{-1}\mathbf{v_i}}{\mathbf{v_i^H}\hat{\mathbf{K}}_{\mathbf{ii}}^{-1}\mathbf{v_i}} \tag{4.102}$$

The weights are then stacked and applied to the data covariance matrix as in equations 3.50 and 3.51, also repeated below.

$$\mathbf{w_{ATC}} = \frac{1}{\mathbf{M}}\begin{bmatrix} \mathbf{w_1} \\ \mathbf{w_2} \\ \vdots \\ \mathbf{w_M} \end{bmatrix} \tag{4.103}$$

$$y_{atc} = \mathbf{w}_{atc}^H \hat{K} \mathbf{w}_{atc} \tag{4.104}$$

The expression for the power estimate may be written in terms of individual subarray covariance matrices and steering vectors. If $\mathbf{v_i}$ is the steering vector for the i^{th} subarray, K_{ii} is the covariance matrix of the i^{th} subarray, and K_{ij} is the cross-covariance between the i^{th} and j^{th} subarrays, and M is the number of subarrays, then the ATC power estimate can be written as

$$\hat{P}_{atc} = \frac{1}{M^2}\sum_{i=1}^{M}\sum_{j=1}^{M}\frac{\mathbf{v_i^H}\hat{K}_{ii}^{-1}\hat{K}_{ij}\hat{K}_{jj}^{-1}\mathbf{v_j}}{(\mathbf{v_i^H}\hat{K}_{ii}^{-1}\mathbf{v_i})(\mathbf{v_j^H}\hat{K}_{jj}^{-1}\mathbf{v_j})}. \tag{4.105}$$

For the two subarray case, this simplifies to

$$\hat{P}_{atc} = \frac{1}{4}\left[(\mathbf{v_1^H}\hat{K}_{11}^{-1}\mathbf{v_1})^{-1} + (\mathbf{v_2^H}\hat{K}_{22}^{-1}\mathbf{v_2})^{-1} + \frac{\mathbf{v_1^H}\hat{K}_{11}^{-1}\hat{K}_{12}\hat{K}_{22}^{-1}\mathbf{v_2} + \mathbf{v_2^H}\hat{K}_{22}^{-1}\hat{K}_{21}\hat{K}_{11}^{-1}\mathbf{v_1}}{(\mathbf{v_1^H}\hat{K}_{11}^{-1}\mathbf{v_1})(\mathbf{v_2^H}\hat{K}_{22}^{-1}\mathbf{v_2})}\right]. \tag{4.106}$$

The first two terms are the MVDR power estimates for the individual subarrays. The first and second moments of each of these terms are known from the Capon Goodman results. The difficulty arises in computing the statistics of the cross terms. It is useful to examine the numerator of these cross-terms separately.

Let

$$t_1 = \mathbf{v_1^H}\hat{K}_{11}^{-1}\hat{K}_{12}\hat{K}_{22}^{-1}\mathbf{v_2}. \tag{4.107}$$

Now, it is useful to express this in terms of the full array covariance matrix and/or its inverse. That will enable us to bring previous work on full-array adaptive processing to bear on this problem.

Let the full sample covariance matrix, $\hat{K}$, be partitioned according to subarrays.

$$\hat{K} = \begin{bmatrix} \hat{K}_{11} & \hat{K}_{12} \\ \hat{K}_{21} & \hat{K}_{22} \end{bmatrix} \tag{4.108}$$

The inverse of this matrix may then be expressed as

$$\hat{K}^{-1} = \begin{bmatrix} \Psi & -T\Theta^{-1} \\ \Theta^{-1} & T^H\Theta^{-1} \end{bmatrix} \tag{4.109}$$

where

$$T = \hat{K}_{11}^{-1}\hat{K}_{12} \tag{4.110}$$

$$\Theta = \hat{K}_{22} - \hat{K}_{21}T \tag{4.111}$$

$$\Psi = T\Theta^{-1}T^H + \hat{K}_{11}^{-1} \tag{4.112}$$

It is then possible to express t1 in terms of the matrix partitions and the partitions of the matrix inverse.

$$t1 = \begin{bmatrix} \mathbf{v_1} \\ \mathbf{0} \end{bmatrix}^H \hat{K}^{-1} \begin{bmatrix} \mathbf{0} \\ -\Theta \hat{K}_{22}^{-1} \mathbf{v_2} \end{bmatrix} \tag{4.113}$$

One may then substitute

$$\Theta \hat{K}_{22}^{-1} \mathbf{v_2} = I - T^H \hat{K}_{12} \hat{K}_{22}^{-1} \mathbf{v_2} \tag{4.114}$$

into the equation for t1 to obtain

$$t1 = \begin{bmatrix} \mathbf{v_1} \\ \mathbf{0} \end{bmatrix}^H \hat{K}^{-1} \begin{bmatrix} \mathbf{0} \\ -\mathbf{v_2} \end{bmatrix} + \begin{bmatrix} \mathbf{v_1} \\ \mathbf{0} \end{bmatrix}^H \hat{K}^{-1} \begin{bmatrix} \mathbf{0} \\ T^H \hat{K}_{12} \hat{K}_{22}^{-1} \mathbf{v_2} \end{bmatrix} \tag{4.115}$$

or

$$t1 = t1a + t1b. \tag{4.116}$$

The part is simply the full array sample covariance matrix pre and post-multiplied by deterministic vectors. The first and second moments of those terms are known [6]. The second term, t1b, is more challenging. Again, seek an expression in terms of the full array covariance and deterministic vectors and/or matrices.

Let

$$A = \begin{bmatrix} I \\ 0 \end{bmatrix} \tag{4.117}$$

and

$$B = \begin{bmatrix} 0 \\ I \end{bmatrix} \tag{4.118}$$

Then

$$\hat{K}_{11} = A^H \hat{K} A, \tag{4.119}$$

$$\hat{K}_{22} = B^H \hat{K} B, \tag{4.120}$$

$$\hat{K}_{12} = B^H \hat{K} A, \tag{4.121}$$

and

$$\hat{K}_{21} = A^H \hat{K} B. \tag{4.122}$$

With these substitutions, term t1b is then

$$t1b = \mathbf{v_1} A^H \hat{K}^{-1} B A^H \hat{K} B (A^H \hat{K} A)^{-1} B^H \hat{K} A (B^H \hat{K} B)^{-1} \mathbf{v_2}. \tag{4.123}$$

Note also that the remaining term in the power estimate is simply the complex conjugate of t1. At this point, no assumptions have been made other than that the sample covariance matrix $\hat{K}$ is full rank, i.e. invertible.

At this point, some assumptions are made about the data. The first term in t1, namely t1a is familiar to array processing. The second term, however, has more complicated statistics. This begs the question, then, are there any cases in which terms t1b and t2b can be neglected. Fortunately, the answer is yes.

If the propagation environment is white-noise dominated, terms t1b and t1a may be neglected. This is referred to as the low-energy coherence case [45]. In this case, the element-level signal and interference levels are significantly smaller than the element-level white noise level, but when several snapshots of data are averaged, the coherent signal eventually rises above the noise level providing detection potential. In such a case, for essentially all interferer coherence lengths, terms t1a and t1b may be neglected. Figure 4.12 demonstrates the effect of neglecting these terms in the clairvoyant power estimate as a function of interferer coherence length. The environment contains a signal with a -30 dB element-level psd at 90-degrees, an interferer at 90.3-degrees with a psd of -20 dB and a white noise level of 0 dB. The blue curve is the clairvoyant power estimate using the ATC algorithm and a 240 element single line array with two subarrays. The target is perfectly coherent for this example.

Continuing with this approximation, one must still estimate the expected value of the cross terms. The approximate power estimate is now, neglecting t1b and t2b,

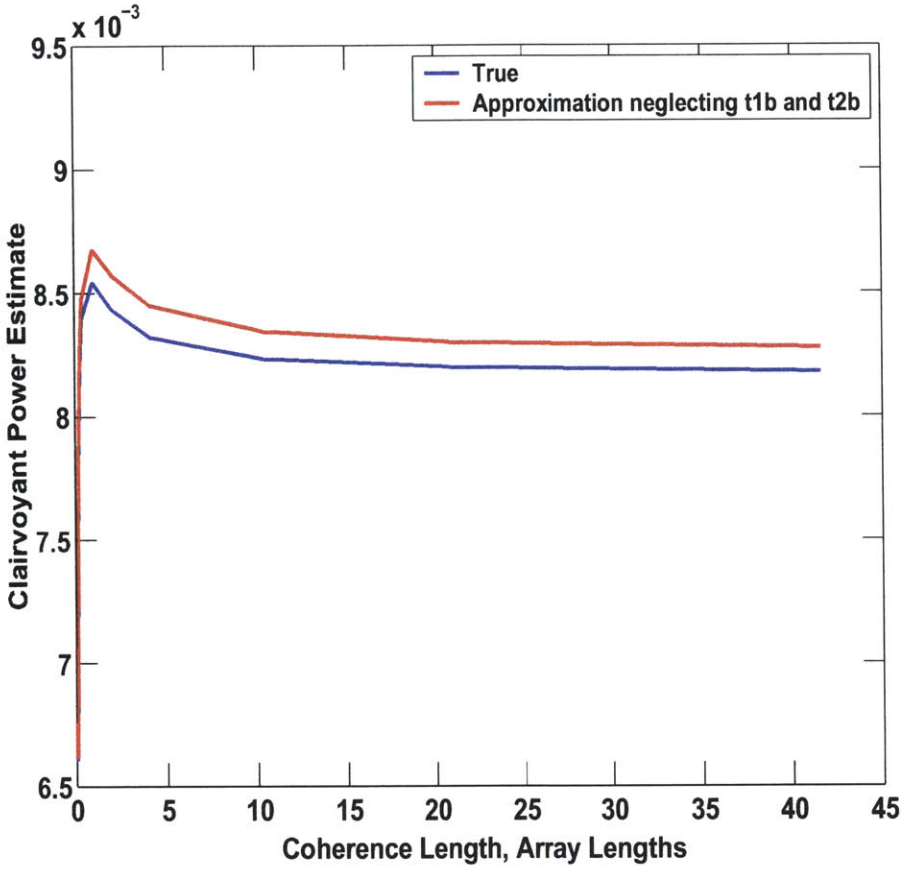

Figure 4-10: Clairvoyant ATC power estimate and approximation neglecting terms t1b and t2b for a low-energy coherence example.

given by

$$\hat{P}_{atc,lec} = \frac{1}{4}\left[(\mathbf{v}_1^H \hat{K}_{11}^{-1}\mathbf{v}_1)^{-1} + (\mathbf{v}_2^H \hat{K}_{22}^{-1}\mathbf{v}_2)^{-1} + \frac{\mathbf{v}_1^H A^H \hat{K}^{-1} B\mathbf{v}_2 + \mathbf{v}_2^H B^H \hat{K}^{-1} A\mathbf{v}_1}{(\mathbf{v}_1^H \hat{K}_{11}^{-1}\mathbf{v}_1)(\mathbf{v}_2^H \hat{K}_{22}^{-1}\mathbf{v}_2)}\right] \tag{4.124}$$

Again, this approximation assumes that the environment, while it may contain discrete interference, is dominated by white noise. At this point we invoke another assumption. We now approximate each of the terms as being independent. Clearly, if this assumption were made earlier, the entire cross-terms would be eliminated. By making the assumption at this point, we preserve some of the impact of these cross-terms. This assumption may be valid for environments with very limited spatial

coherence.

In this case, the expected value of each term may be computed. The expected value of the first two terms is given by the Capon/Goodman work [7]. The expected value of the inverse of the full array covariance matrix is provided by [19]. The result can be expressed in terms of clairvoyant estimates (denoted by no hats).

$$E\left[\mathbf{v}_1^H \hat{K}_{11}^{-1}\mathbf{v}_1)^{-1}\right] = \frac{L-N/2+1}{L}P_1 \tag{4.125}$$

$$E\left[\mathbf{v}_2^H \hat{K}_{22}^{-1}\mathbf{v}_2)^{-1}\right] = \frac{L-N/2+1}{L}P_2 \tag{4.126}$$

$$E\left[\frac{\mathbf{v}_1^H A^H \hat{K}^{-1} B\mathbf{v}_2}{(\mathbf{v}_1^H \hat{K}_{11}^{-1}\mathbf{v}_1)(\mathbf{v}_2^H \hat{K}_{22}^{-1}\mathbf{v}_2)}\right] = P_1P_2\left(\frac{L-N/2+1}{L}\right)^2 (P_{12})\frac{L}{L-N} \tag{4.127}$$

$$E\left[\frac{\mathbf{v}_2^H B^H \hat{K}^{-1} A\mathbf{v}_1}{(\mathbf{v}_1^H \hat{K}_{11}^{-1}\mathbf{v}_1)(\mathbf{v}_2^H \hat{K}_{22}^{-1}\mathbf{v}_2)}\right] = P_1P_2\left(\frac{L-N/2+1}{L}\right)^2 (P_{21})\frac{L}{L-N} \tag{4.128}$$

where

$$P_1 = (\mathbf{v}_1^H K_{11}^{-1}\mathbf{v}_1)^{-1} \tag{4.129}$$

$$P_2 = (\mathbf{v}_2^H K_{22}^{-1}\mathbf{v}_2)^{-1} \tag{4.130}$$

$$P_{12} = \begin{bmatrix}\mathbf{v_1}\\ \mathbf{0}\end{bmatrix}^H \hat{K}^{-1}\begin{bmatrix}\mathbf{0}\\ -\mathbf{v_2}\end{bmatrix} \tag{4.131}$$

$$P_{21} = \begin{bmatrix}\mathbf{0}\\ -\mathbf{v_2}\end{bmatrix}^H \hat{K}^{-1}\begin{bmatrix}\mathbf{v_1}\\ \mathbf{0}\end{bmatrix} \tag{4.132}$$

Clearly, it cannot be true that the inverses of the individual subarray sample covariance matrices are independent of the inverse of the full array sample covariance matrix, but the approximation greatly simplifies the statistics. It also provides a reasonable approximation to the mean of the ATC power estimate when the snapshot support is high. Figure 4.11 shows the bias in the ATC estimate compared to simulations.

While this approximation may be implemented in low-energy coherence environments, many applications of interest in passive sonar, and the applications of interest

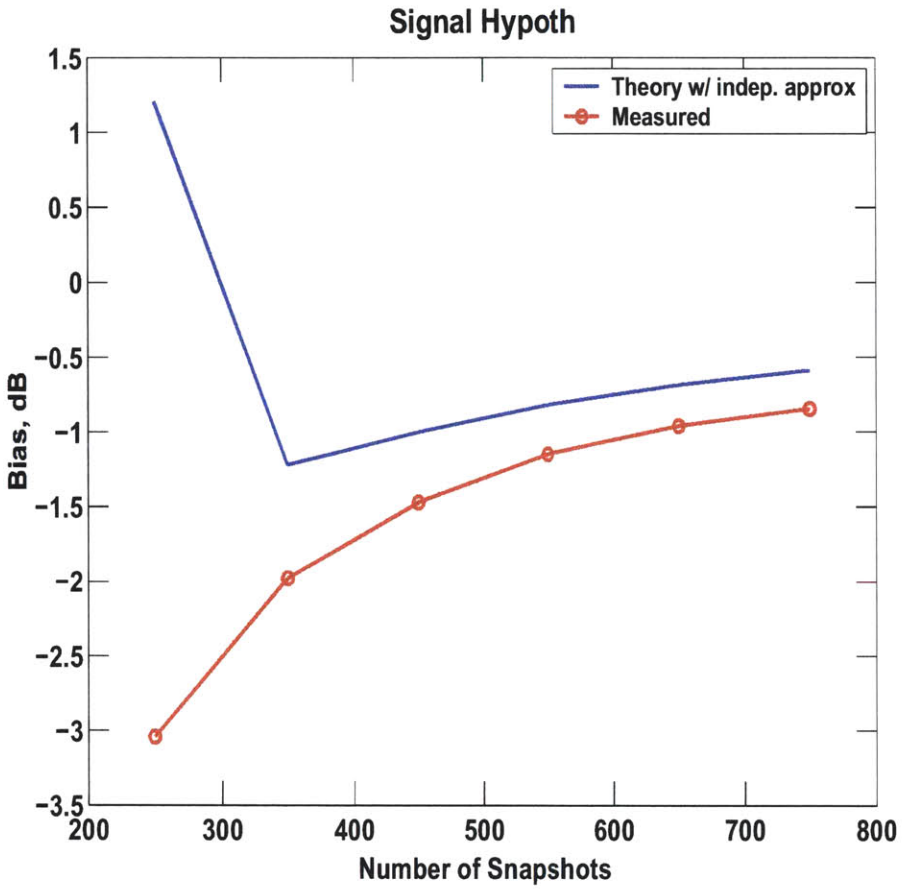

Figure 4-11: Simulated and theoretical bias of ATC power estimate in LEC example. Signal and interferer are coherent.

to this thesis, are dominated by loud interference. In this case, the LEC approximation is poor. Figure 4.12 shows the effects of neglecting t1b and t2b in the clairvoyant power estimate. This example is identical to that in Figure 4.10 except the element-level signal power is 0 dB and the element-level interferer power is 20dB. Clearly, those terms may no longer be neglected.

To summarize, the model presented thus far for the ATC statistics is reasonable under the following conditions:

1. Number of snapshots is moderately larger than the number of sensors in the full array

2. The element-level signal and interference powers are significantly lower than the

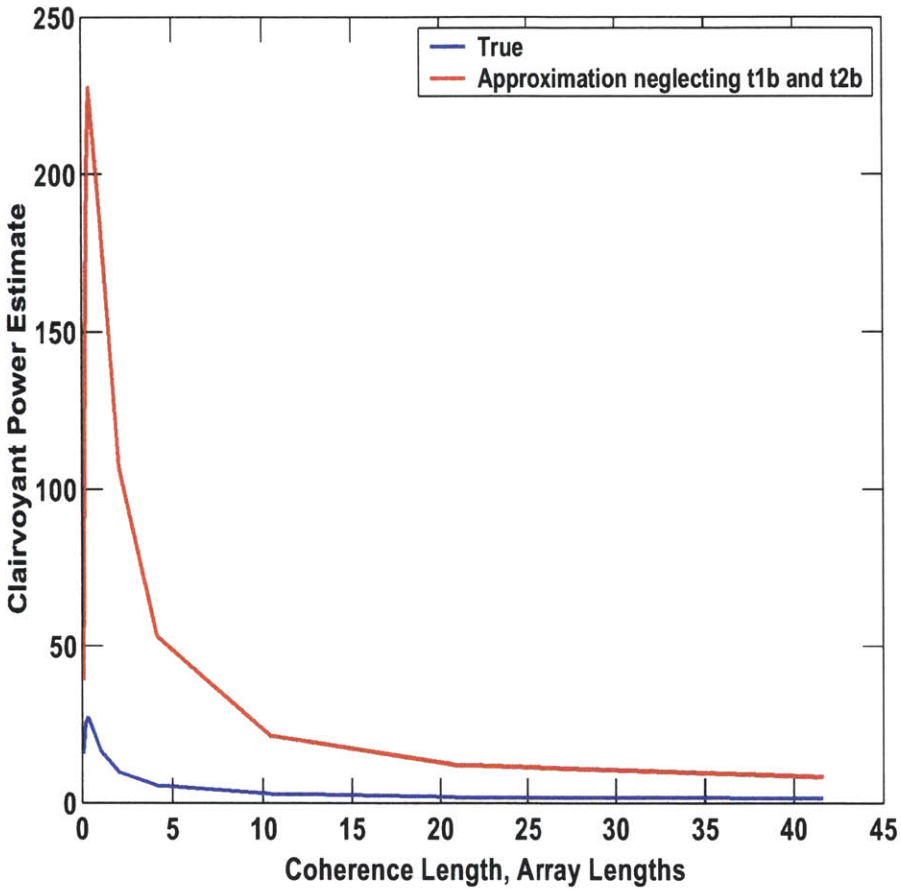

Figure 4-12: Clairvoyant ATC power estimate and approximation neglecting terms t1b and t2b for non-lec example.

white noise level

This approach will not provide adequate accuracy for the interference-dominated environments of interest. Therefore, a better model is needed. Further, the analysis thus far is conditioned on full rank sample covariance matrices for the full array. One purpose of subarray algorithms is to reduce the requisite snapshot support. We therefore need a model which is valid for reduced snapshot scenarios.

Taking a step back from the linear algebra, it is clear that all adaptivity of the processor is a result of adaptive processing on a given subarray. Therefore, the bias of the power estimates should intuitively be of the same order of magnitude as those incurred by processing an array the length of the subarray. Since there is a second

stage to the processing, the bias of the overall power estimate will certainly vary from this approximation, but it is useful to examine the validity of this approximation.

Capon and Goodman showed that the expected value of the MVDR power estimate (for a full array) is given by

$$E\left[\hat{P}_{mvdr}\right] = P_{mvdr}\frac{L-N+1}{L}. \tag{4.133}$$

Let us now approximate the expected value of the ATC power estimate as the clairvoyant estimate multiplied by the same "snapshot factor" replacing N, the number of sensors in the array, by N/M, the number of sensors in a subarray. This results in

$$E\left[\hat{P}_{atc}\right] \approx P_{atc}\frac{L-N/M+1}{L}. \tag{4.134}$$

Figure 4.13 shows the same bias plot of Figure 4.11, only this time includes the approximation based on the Capon Result. Clearly, the Capon/Goodman approximation yields a far better model than that of the independence assumption.

Figure 4.14 shows a plot of the fractional bias as a function of number of snapshots of this approximated power estimate. It is compared to the bias of simulations. This example again contains a single target at 90-deg, 0dB, an interferer at 90.3-deg, 20 dB, and 0 dB white noise. Both the target and interferer are assumed to be perfectly coherent, and a single streamer is used.

As the coherence of the interferer degrades, this approximation improves since there is less correlation between the subarrays. This is shown in Figure 4.15. Note also the strong agreement when the snapshot support is low. These simulations have been conducted for the 2-subarray configuration.

This new statistical model assumes that only the adaptive stage contributes to the bias. If it is further assumed that the adaptive stage dominates the variance as well, the variance may be approximated again using the work of Capon and Goodman [7]. The variance of the MVDR power estimate is given by

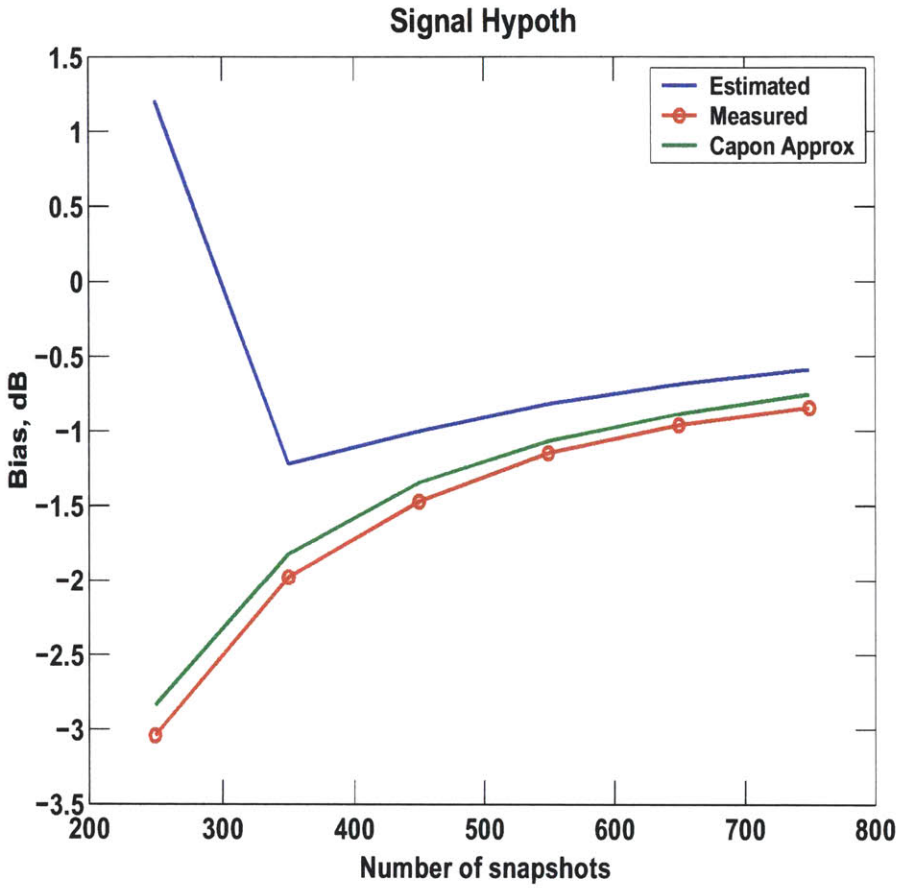

Figure 4-13: Bias predicted using a modified Capon/Goodman approximation compared to simulation when target and interferer are coherent, lec environment.

$$var\left[\hat{P}_{mvdr}\right] = \frac{1}{L-N+1} E\left[\hat{P}_{mvdr}\right]^2 \tag{4.135}$$

$$= \frac{L-N+1}{L^2} P_{mvdr}^2. \tag{4.136}$$

These statistics are derived for full array processing. In the proposed model, the number of elements in a subarray replaces N, yielding

$$var\left[\hat{P}_{atc}\right] \approx \frac{L-N/M+1}{L^2} P_{atc}^2. \tag{4.137}$$

Figure 4.16 shows a comparison between the simulated and modeled variance as

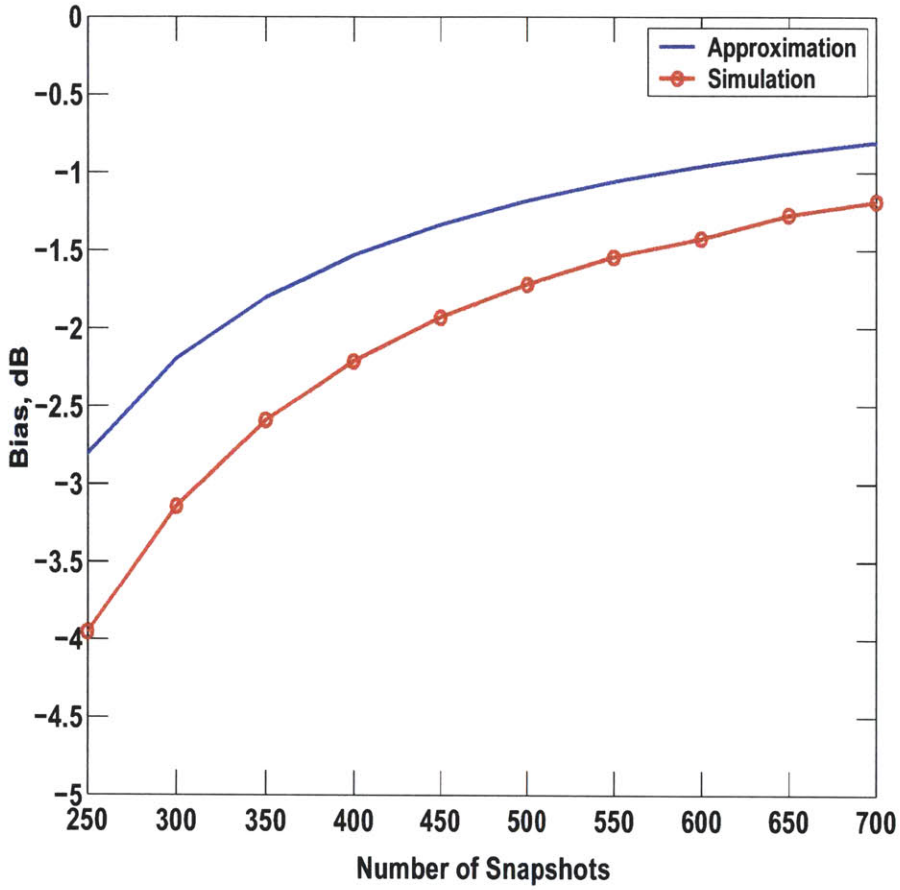

Figure 4-14: Bias predicted using a modified Capon/Goodman approximation compared to simulation when target and interferer are coherent, non-lec environment.

a function of the number of snapshots, normalized by the square of the asymptotic power estimate.

The agreement is within about 3 dB.

The goal is to model the pdf of the power estimate in order to predict detection performance. There is now a model for the mean and variance of the power estimate. The approach taken here is then to model the power estimate as a Gaussian random variable with mean and variance given. If the number of snapshots and subarrays are large,that indicates that the power estimate is the sum of a large number of random variables, and hence, may be be reasonably approximated by a Gaussian random variable with mean and variance given by the model.

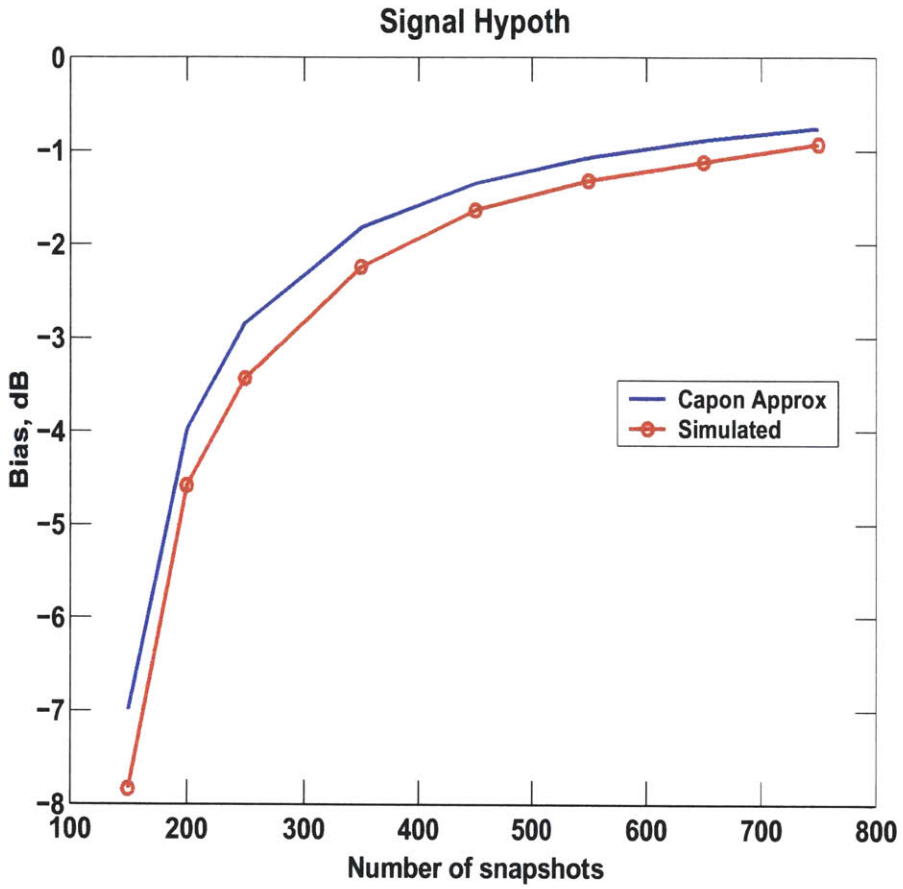

Figure 4-15: Bias predicted using a modified Capon/Goodman approximation compared to simulation when interferer coherence is 100 elements.

These pdfs are then fed into a LRT as in the previous sections. Again, the performance metric of interest is then the detection probability for a constant false alarm rate. There are a few cases of interest in validating this model. First, the accuracy of this model as a function of coherence is of interest. Second, the accuracy of this model as a function of the number of subarrays is of interest. Figure 4.17 shows the agreement between model and simulation for 12 subarrays with 250 snapshots. The agreement is remarkable.

This algorithm performs well for all scenarios of interest in this thesis. As mentioned earlier, the approximation is stressed most when the discrete sources decorrelate. Even in those cases the approximations are good. Figure 4.18 shows the

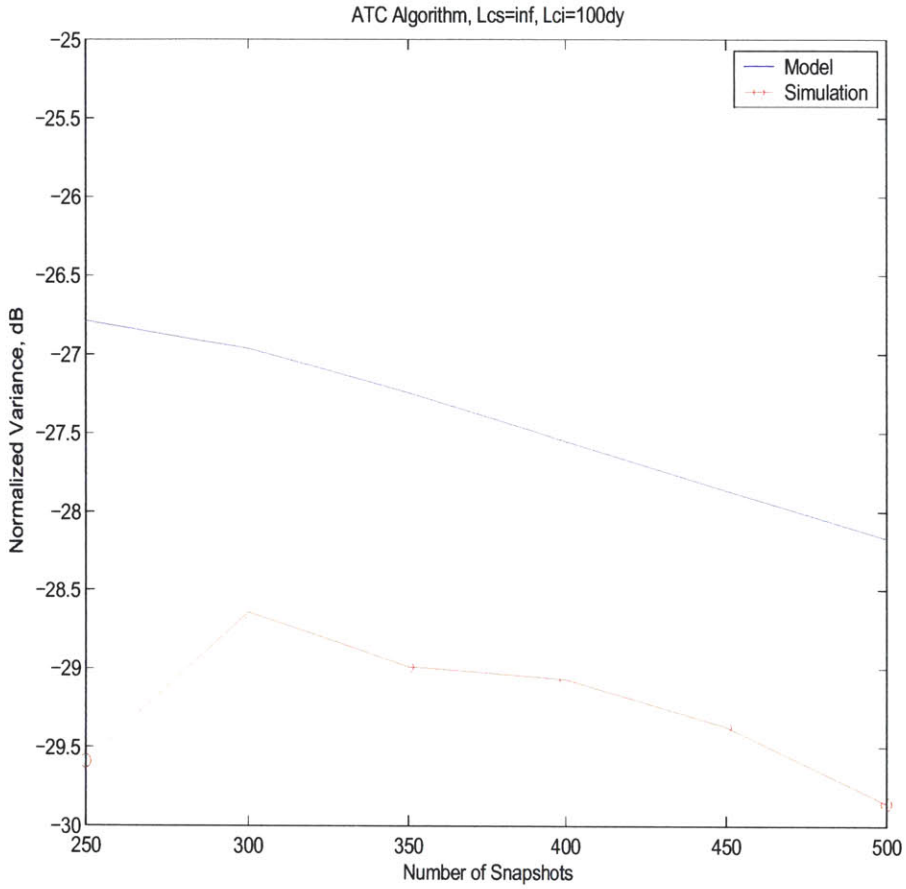

Figure 4-16: Variance predicted using a modified Capon/Goodman approximation compared to simulation when interferer coherence is 100 elements.

comparison between the model and simulations for a coherent target and coherent interference for 50 snapshots and 250 snapshots. The agreement is good, but not perfect. It is good enough to represent the trends in the algorithm performance. Figure 4.19 shows the performance when the signal is coherent but the interferer has a coherence length of 50 elements. The agreement between the model and simulations are excellent. Similar agreement is seen when the signal decorrelates, although those results are not shown here.

This new model is then valid when:

1. The number of snapshots exceeds the number of elements in a subarray

2. Signal and interference are coherent or decorrelated, although it is best when

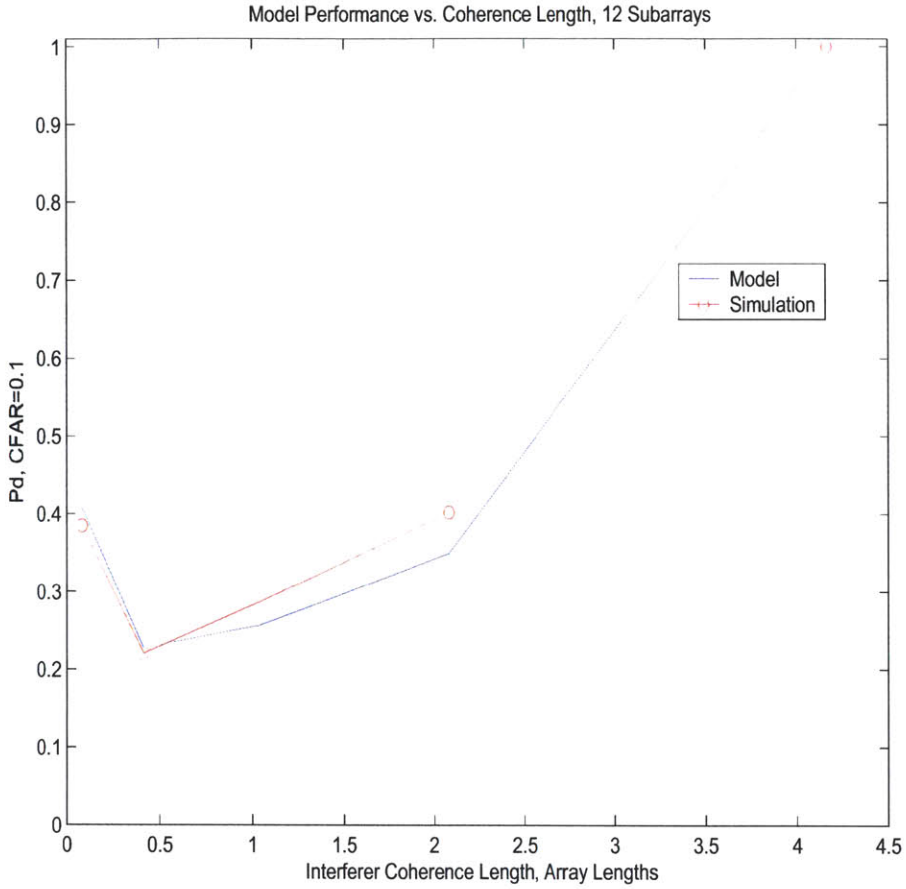

Figure 4-17: Detection performance vs. coherence length for 12 subarrays, 250 snapshots. Model and simulation.

the interference has decorrelated.

This new simple model will be used in the remainder of the thesis to predict the performance of the ATC algorithm.

4.6 Summary

This chapter has derived statistical models for the detection performance of an array using the CTA, AI, and ATC algorithms. The models agree well with simulations in all regions of snapshot support so long as the number of snapshots exceeds the number of adaptive DOFs. The validity of the models in signal and interfere coherence regions

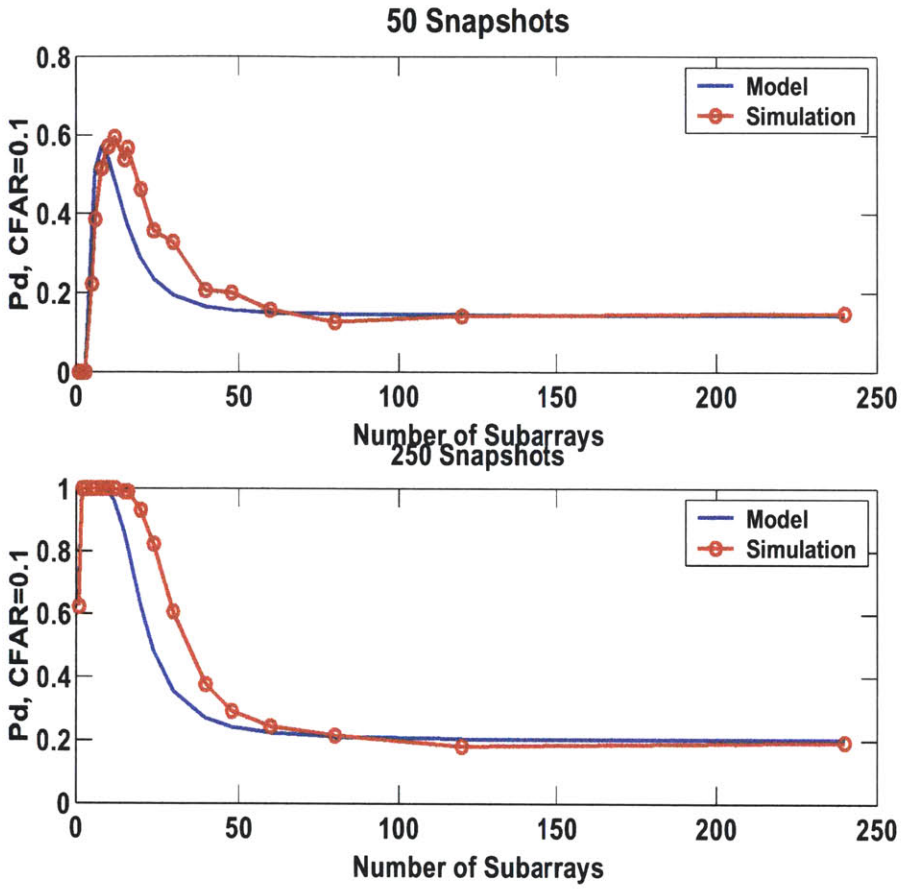

Figure 4-18: Detection performance vs. number of subarrays. The target is coherent and the interferer has a coherence length of 2500 elements (¿10 array lengths).

are provided in tabular form below. The notation is given below.

- HH - High target coherence, High interferer coherence
- HL - High target coherence, Low interferer coherence
- LH - Low target coherence, High interferer coherence
- LL - Low target coherence, Low interferer coherence

The computational savings afforded by these models leads to simple comparisons of algorithm and subarray partition performance without exhaustive Monte Carlo simulations. These models incorporate both snapshot support and coherence limitations of discrete sources, and are independent of propagation model.

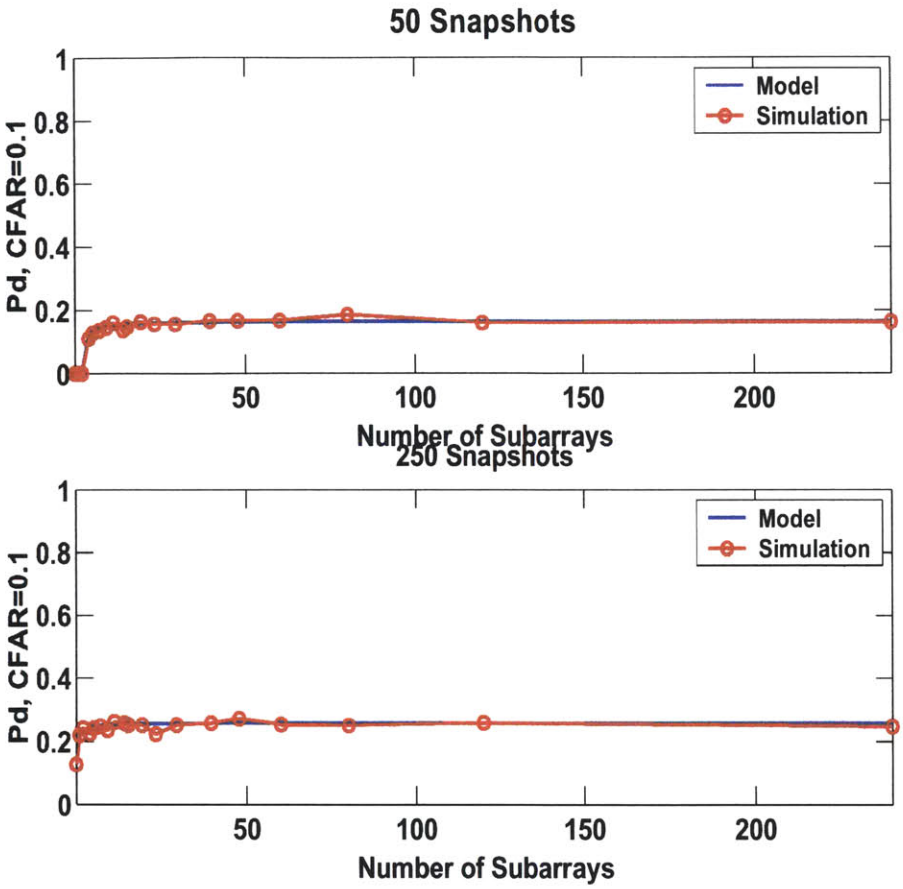

Figure 4-19: Detection performance vs. number of subarrays. The target is coherent and the interferer has a coherence length of 50 elements.

Chapter 5 uses the theory and models developed in this chapter to examine the performance of arrays in interference-dominated environments in which there is limited snapshot support and limited spatial coherence. Insight into optimum array partitioning for processing in these environments is gained for both linear arrays and planar arrays, with both plane-wave propagation models and matched-field models.

Algorithm	HH	HL	LH	LL	Comments
Optimum, DOF model	excellent	excellent	moderate	moderate	exact for coherent signal
CTA	excellent	excellent	excellent	excellent	exact statistics
AI	good	good	good	good	best for low numbers of subar
ATC	moderate	excellent	moderate	excellent	best for decorrelated interfere

Table 4.1: Summary of model validity. The second column characterizes the performance in scenarios of interest to this thesis.

Chapter 5

Array Performance in Coherence-Limited and Snapshot-Starved Environments

Chapter 4 presented a statistical analysis of the detection performance of subarray algorithms. The statistical analyses included the effects of two performance degradation mechanisms, namely finite spatial coherence and limited snapshot support. While subarray processing helps mitigate the effects of these mechanisms, the question of subarray partitioning strategy is still open. This section presents several new results which yield insight and design guidelines for partitioning and processing large aperture planar arrays via sub-apertures.

It is first important to understand the impact of coherence limitations on the array processor. The effects of interference decorrelation impact performance in a manner different than source decorrelation. The first section of this chapter examines the effects of spatial coherence on detection performance and sub-aperture partitioning using a single line array and one main beam interferer.

Next Section 5.2 presents a comparison of the CTA and ATC algorithms. Since the algorithms apply adaptivity at different stages, their performance is significantly different for a given subarray configuration. This section also presents a discussion of the trade-off between resolution and adaptivity in a coherence-limited environment.

The CTA algorithm applies adaptivity across subarrays, which hold the potential for high resolution, but may not be coherent. The ATC algorithm applies the adaptivity within a subarray trading resolution for processing over a coherent aperture. The two algorithms are compared in an interference-dominated environment.

The third section of this chapter explores the potential improvements to processing a planar array via subarray processing using MFP. In the case of MFP, both coherence and resolution play a role in subarray partitioning schemes. This is discussed in detail in Section 5.3.

5.1 Coherence Effects

This section presents a study of the effects of spatial decorrelation of signals of interest as well as interfering noise sources. Much work has been done to examine the signal gain degradation effects of spatial decorrelation of sound sources in the ocean. Several exponential models exist [3], [4], one of which was presented in Chapter 3. Further there have been numerous experimental studies of signal coherence in the ocean [33],[2], and [5] among others. The most common method for estimating spatial coherence is through examining the array response to a narrow-band signal oriented broadside to an array. This orientation limits the effects of multi-path propagation prevalent in shallow water environments. The measured array gain is then used to estimate the transverse coherence length of a signal according to a coherence model.

Further, simulation studies have been conducted to assess the coherence loss of signals propagating through anisotropic environments, such as those containing internal waves [47]. The resulting coherence estimates in those cases have a spatial dependence based on the orientation of the source and the internal wave field.

In all cases, spatial decorrelation of a signal impacts the array's detection performance. One aspect of this coherence issue which has not been studied, however, are the relative effects of target vs interferer coherence. It is accepted that signals propagating over longer ranges are more likely to encounter phenomena such as inter-

nal waves and other volume inhomogeneities which would cause them to lose spatial coherence. Further, interference sources are typically much louder than targets of interest, and hence impact detection performance over longer ranges. Therefore, the coherence of interferers may be much lower than that of a nearby, quiet target. Alternatively, there may be a loud interferer nearby which has not experienced significant spatial decorrelation. Therefore, it is useful to examine the effects of both target and interference levels of coherence separately.

Recall the coherence model presented in section 2.3. This models the coherence between two sensors as degrading exponentially with their separation in the direction transverse to the signal's propagation. This is based on the assumption that signal will be less coherent when originating from the broadside direction than the endfire direction.

As a discrete signal decorrelates, the transverse wavenumber spread of it spectrum widens. The resolution of this spectrum, however, depends upon the resolution of the array. For example, a single coherent plane wave has an impulsive wavenumber spectrum, but a finite array is not able to resolve this impulse in wavenumber. The spectrum appears to have a finite width due to the array length. As the signal decorrelates, however, this impulse gains a finite width. Figure 5.1 shows the array response as a function of wavenumber to a source located broadside to the array with varying coherence lengths. The array is a single line of 240 sensors spaced 12.5m apart. The operating frequency is 50 Hz, and the element-level signal spectral level is 0 dB. As the coherence length increases, the width of the mainlobe expands while the level of the peak decreases since power is conserved. In the limit of a signal completely decorrelating, the result is a flat spectrum, analogous to a white noise spectrum.

This decorrelation applies to all discrete sources, whether it is a target of interest or clutter. The role each of these play in the detection problem, however, are quite different. First, the role of interference coherence is examined, followed by a discussion of target source decorrelation. To simplify the analysis so as to better understand the effects of decorrelation, a plane wave model is used in this analysis. This eliminates the effects of fading across the array. Further a single line array is used for the

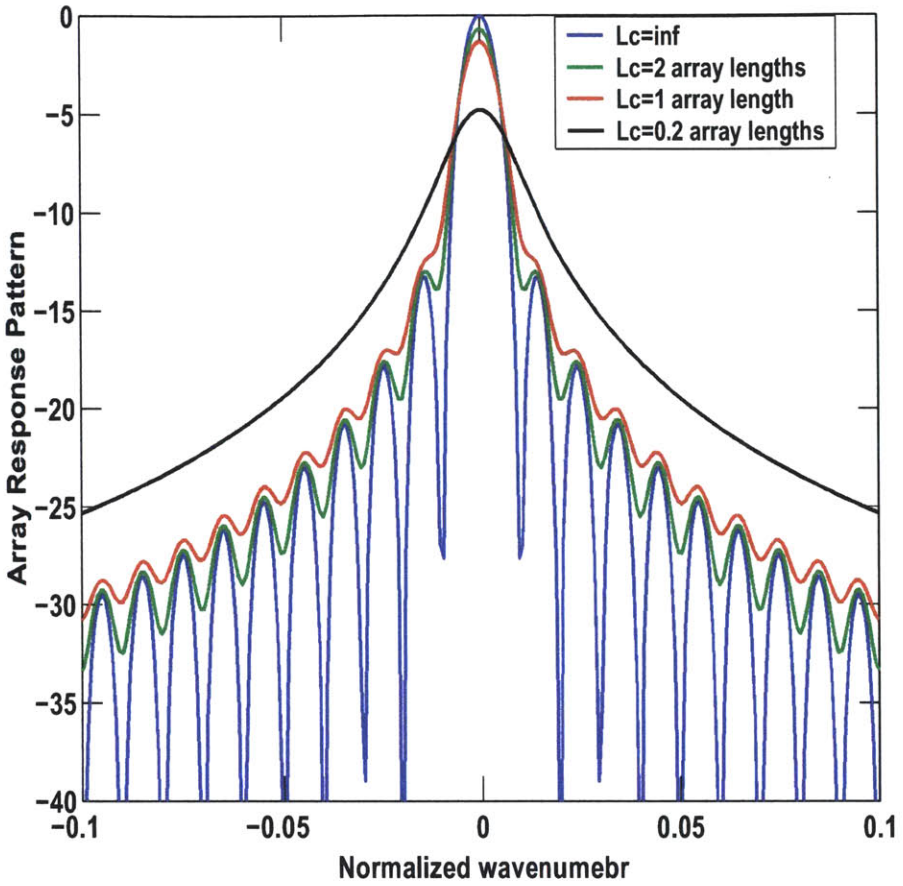

Figure 5-1: Array response to signals of various coherence lengths in wavenumber domain.

examples in sections 5.1.1 and 5.1.2. This array contains 240 sensors spaced 12.5m apart operating at a frequency of 50 Hz.

5.1.1 Interference Decorrelation

Consider, first, the optimum processor. The first stage in the processing is whitening the signal with the data covariance conditioned on the null hypothesis. If the interference spectrum is separated from the signal spectrum by more than the wavenumber resolution of the array, the whitening has little effect on the signal spectrum. If the interference spectrum is spread due to limited spatial coherence, the whitening stage removes any part of the target signal spectrum which overlaps the interference spatial

spectrum. Figure 5.2 shows an example of this phenomenon. Figure 5.2(a) shows the wavenumber response of a target at broadside in red and the response to an interference source plus white noise in blue. The array for this example is a 240-element linear array with inter-sensor spacing of 12.5m. The frequency of is 50 Hz.

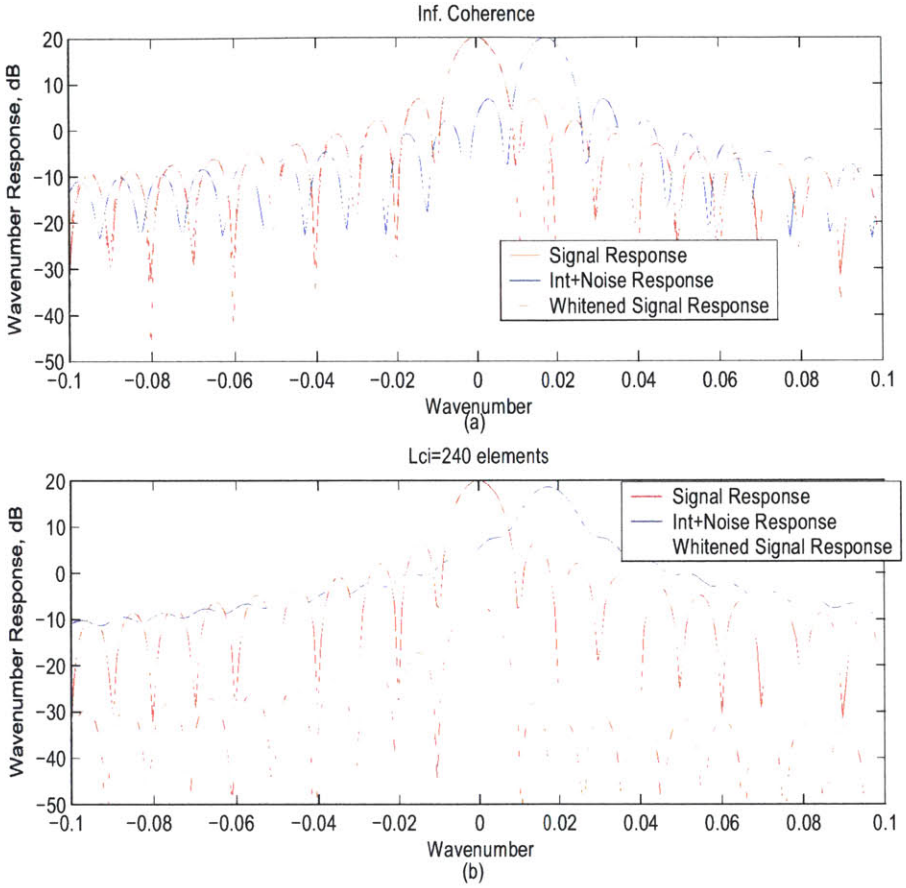

Figure 5-2: Array response to signal, interference, and whitened response for (a) perfect interferer coherence, and (b) Lci=240 elements.

As discrete interference decorrelates, its spectrum overlaps to that of the signal of interest, making detection more difficult. Alternatively, this can be examined by looking at the spread in the eigenvalues of the interference. As an interferer decorrelates, it has a larger wavenumber spectrum, hence occupies a larger subspace. Therefore, to adaptively null this interference, one needs more adaptive degrees of freedom. Figure 5.3 shows the dominant eigenvalues for the scenario in Figure 5.2(a). Here, the

signal is a rank one signal (a perfectly coherent target source). The interference is also coherent, and hence rank one also. Since the target and interference are separated in wavenumber by more than the array's resolution, very little of the signal is lost through whitening. Conversely, when the interference decorrelates, its rank is no longer one as seen in Figure 5.4. This plot shows the dominant eigenvalues relevant to figure 5.2(b). In this case, the interference occupies a greater subspace, some of which contains the signal of interest. Therefore, when this subspace is used to whiten the data, some of the signal power is removed.

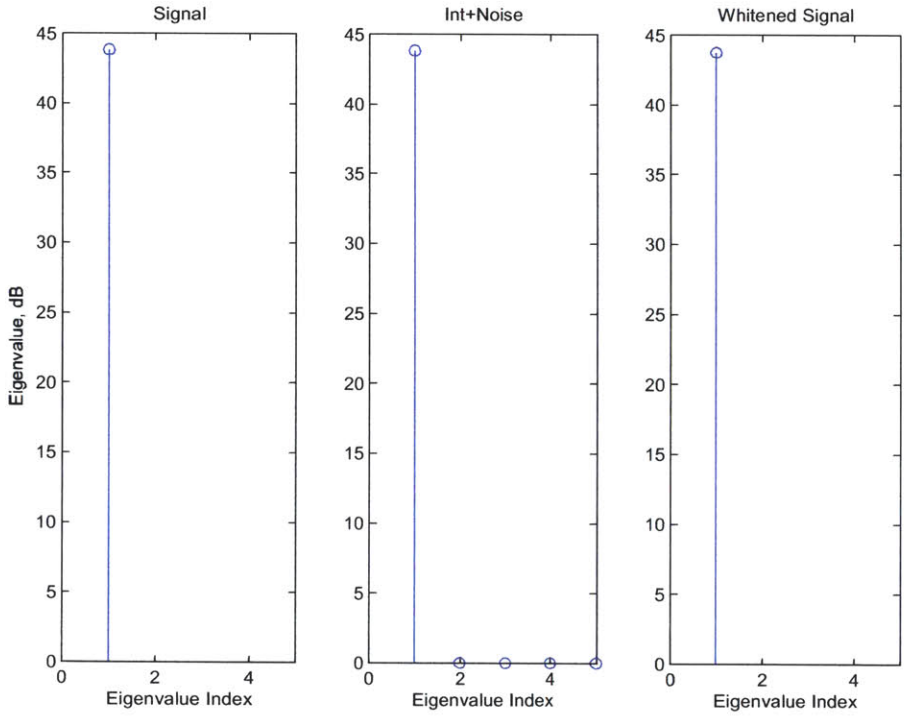

Figure 5-3: Dominant eigenvalues of the signal, interference, and whitened signal covariance for a perfect interferer coherence.

It appears, thus far, that the detection performance degrades as the interference correlation degrades. This is not always the case. In the limit of the interference correlation degrading completely, the interference is spread over all wavenumbers. This then behaves as a heightened level of white noise. In this case, the signal does incur some losses, but less of the interference power is in the direction of the signal (since it is equally spread over all wavenumber) and detection performance improves

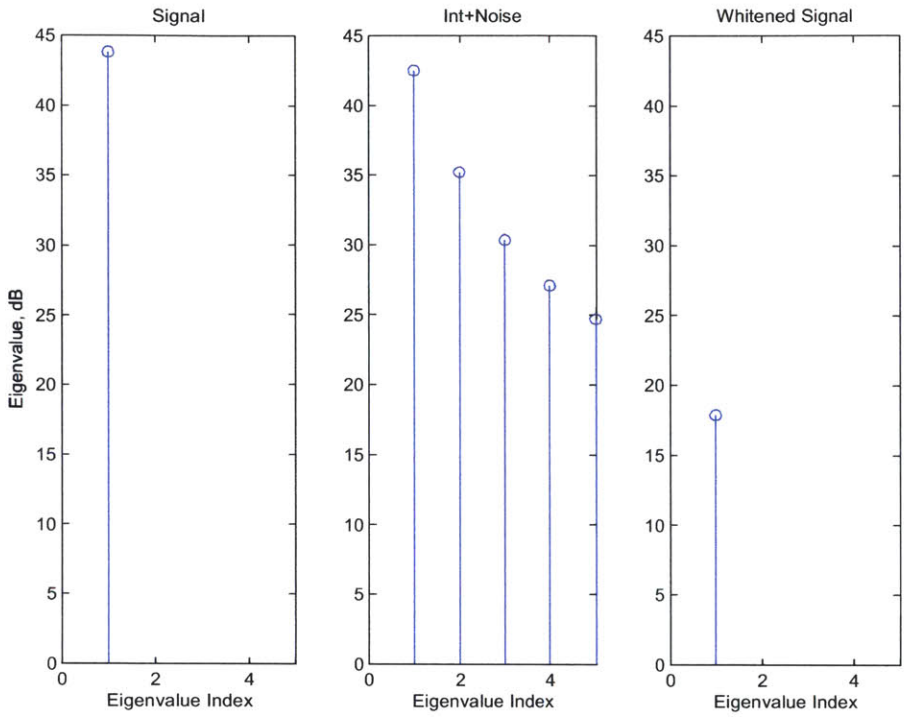

Figure 5-4: Dominant eigenvalues of the signal, interference, and whitened signal covariance for an interferer with a coherence length of 240 elements.

again. Figure 5.5 shows this phenomena. In this example, there is a target of interest at 90-deg with an element level psd of 0 dB. There is also an interferer at 90.3 degrees (0.5 beamwidths away) with an element-level psd of 20 dB. White noise is also present in the example, with an element level of 0 dB. The array is, again, a single streamer containing 240 sensors spaced 12.5m apart, and the frequency is 50 Hz. There were 250 snapshots used in this example. When the interference coherence drops below one array length, the array is able to resolve this spectral spread of the interference, and detection becomes much more difficult. As the interferer decorrelates further, more of the signal is removed during the whitening stage. Once the interference decorrelates beyond 0.2 array lengths (48 sensors) the interference has spread over a wide wavenumber space that it begins to remove less of signal component. This continues until the interference is virtually a white noise signal with a spectral level much lower than the target signal, allowing for detection again.

To this point, the coherence effects have been examined in the context of the

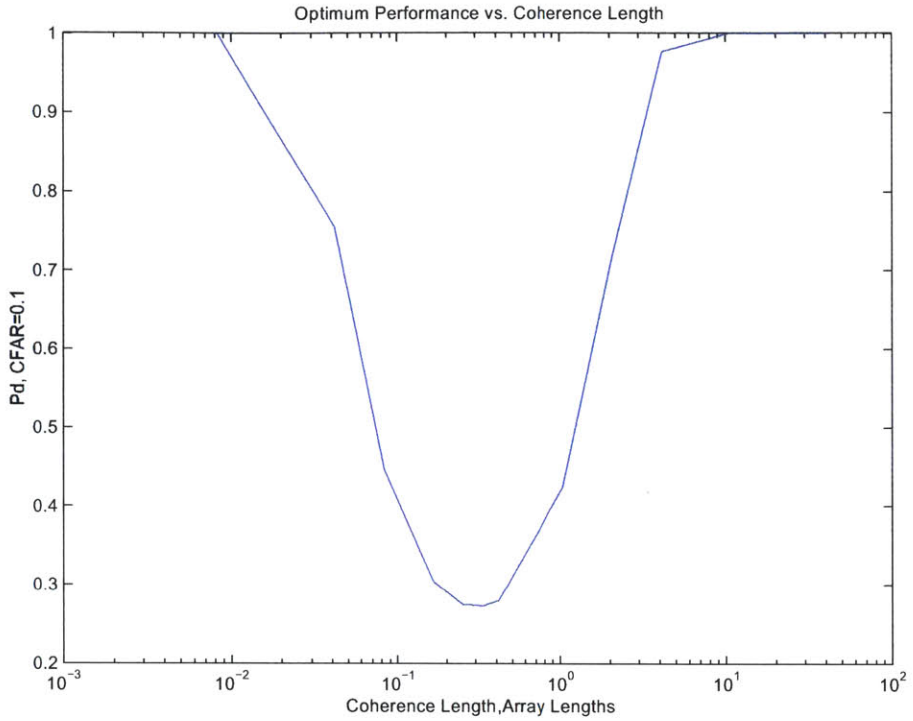

Figure 5-5: Detection performance vs. interference coherence length.

optimum processor. There is no explicit subarray processing for this algorithm, but rather the LRT operates on all data incident upon the array. Recall also that the optimum processor is conditioned on known signal, interference, and noise covariances, and does not incorporate uncertainties in their estimation from the sample covariance matrix. Since the losses associated with finite snapshot support are effectively de-coupled from the coherence problem in this case. As will be shown next, that is not the case with the adaptive subarray algorithms.

Interference decorrelation affects the adaptive subarray algorithms in a manner similar to the effects on the optimum processor. For all algorithms, when the interference decorrelates, a greater degree of adaptivity is needed to appropriately null the interference. This adaptivity has two components. There must be enough adaptive degrees of freedom (i.e. rank of the adaptive-stage covariance) and also appropriate resolution. Further, all of the adaptive subarray algorithms rely on sample covariance matrices. As a result, snapshot support impacts the covariance estimate, hence

the statistics of the subarray power estimate. This, in turn, impacts detection performance. This is the inherent trade-off between adaptivity and snapshot support. While this section focuses on the affects of interference coherence, the snapshot support trade-off is inherently coupled, and must not be ignored.

Figure 5.6 demonstrates the affect of interferer coherence on the CTA algorithm. This example contains a 0 dB target at 90-degrees (broadside), a 20 dB interferer at 90.3-degrees, and 0 dB white noise level. Figure 5.6 plots the probability of detection as a function of interferer coherence length for a 20-subarray configuration. This example includes 250 snapshots, and the source coherence length is modeled as 2500 elements, or approximately 10 array lengths. It is clear that when the interferer is highly correlated, there is sufficient adaptivity and resolution to null the discrete interferer. As the interferer decorrelates, it becomes more and more difficult to remove its effects. When the interference becomes sufficiently decorrelated, it acts like a heightened level of white noise and detection performance again begins to improve. Identical effects are shown in Figures 5.7 and 5.8 for the ATC and AI algorithms respectively. These figures contain the same scenario, and both plots are generated for a 20-subarray configuration.

One may note that a given subarray configuration has different performance from algorithm to algorithm. One reason for this is that the adaptive DOF of the CTA is equal to 20, the number of subarrays. The adaptive DOF for the ATC and AI algorithms is 12, the number of elements within the subarray. There are also more subtle reasons for the performance differences involving resolution and uses of adaptivity. The discussion of these topics is deferred to section 5.2 of this thesis. The ultimate affect of interferer decorrelation is impeded detection which increases with increased decorrelation until the decorrelation spans the observation subspace, behaving like white noise. When the interferer's spectral level in the look-direction falls below that of the target, detection performance improves.

It has been shown that as an interferer decorrelates, its wavenumber spectrum spreads, and as a result, more adaptive degrees of freedom are required to mitigate the interference. The question remains as to how much adaptivity is needed, i.e. what

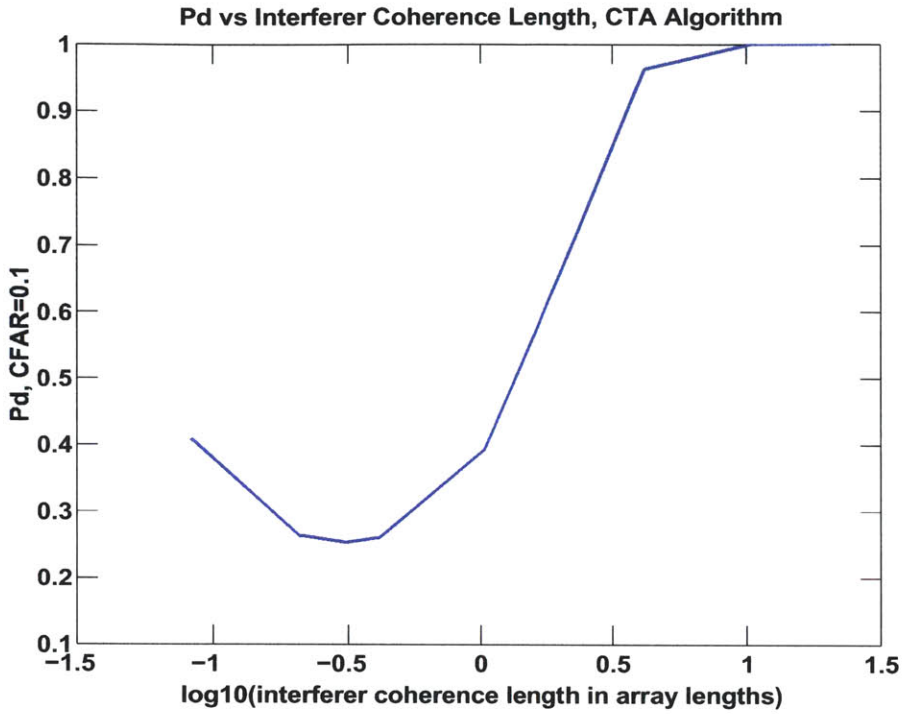

Figure 5-6: Detection performance of the CTA algorithm plotted against the log of the interferer coherence in array lengths. This example contains a 0 dB broadside target, a 20 dB in-beam interferer, and 0 dB white noise level. There are 20 subarrays and 250 snapshots in this example.

is the optimum number of subarrays. Recall also that these algorithms are based on sample covariance matrices, therefore, snapshot support plays a crucial role in this trade-off. To study this trade-off, it is useful to plot the detection performance for a fixed coherence length as a function of subarray configurations. However, since the trade-off is really between adaptivity of the processor and snapshot support, it is more instructive to plot the detection performance against adaptive degrees of freedom for the given algorithm. For the CTA algorithm, the available number of adaptive degrees of freedom (DOF) is equal to the number of subarrays, but for the ATC and AI algorithms, the adaptive DOF is equal to the number of sensors within a subarray.

Figure 5.9 shows the detection performance as a function of the number of subarrays for a fixed interferer coherence length of 500-elements, or roughly two array

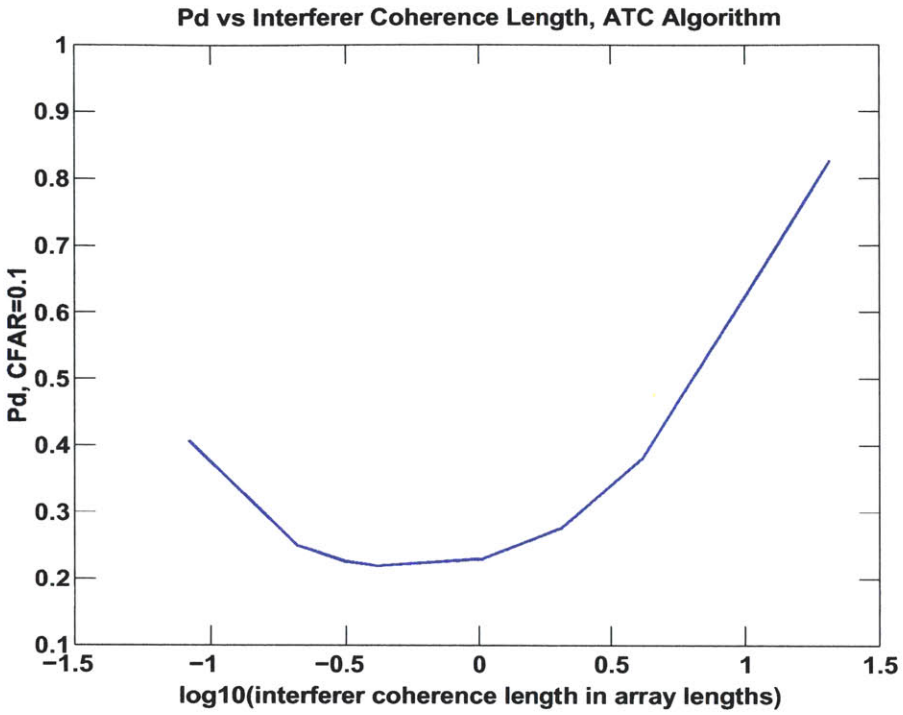

Figure 5-7: Detection performance of the ATC algorithm plotted against the log of the interferer coherence in array lengths. This example contains a 0 dB broadside target, a 20 dB in-beam interferer, and 0 dB white noise level. There are 20 subarrays and 250 snapshots in this example.

lengths. Again, there are 250 snapshots in this example. There is an optimum subarray configuration of 15 subarrays. If the number of subarrays is too few, there is not enough adaptivity to null the nearby interferer. Conversely, if too many subarrays are used, i.e. many adaptive degrees of freedom, the covariance matrices become poorly estimated and result in increased bias and variance of the power estimates leading to poor detection.

Figures 5.10 and 5.11 show the same plots for the ATC and AI algorithms respectively. Again, there is a trade-off between sufficient adaptivity and snapshot support. One may note that the optimum subarray configuration (and hence adaptive DOF) is different for the algorithms whose adaptive stage is first. One reason for this depends on resolution. For the CTA algorithm, the adaptivity is applied across the full array aperture, thus exploiting greater array resolution at the adaptive stage than the ATC

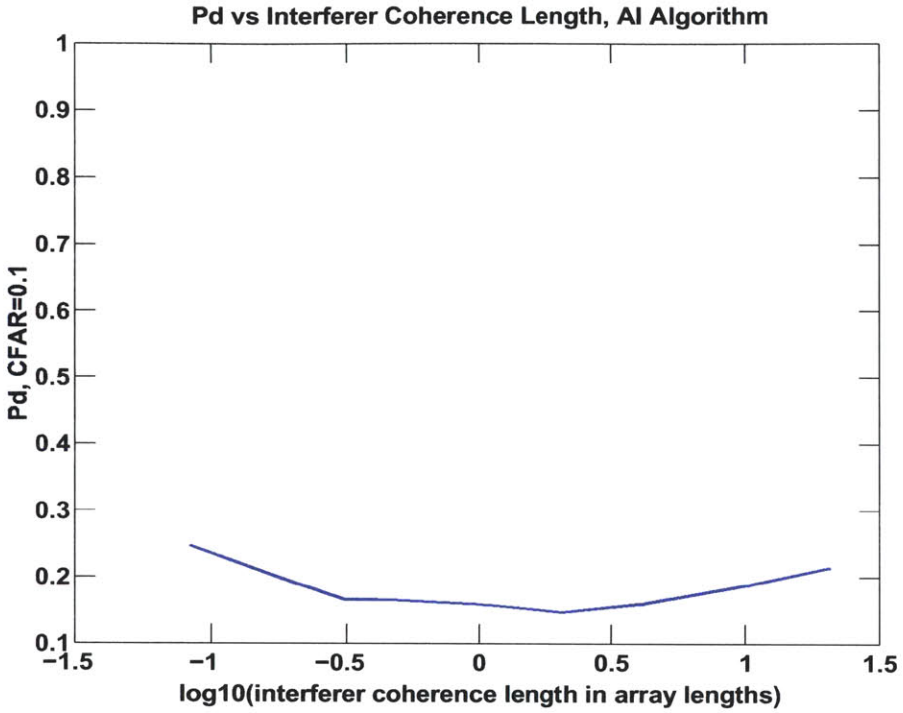

Figure 5-8: Detection performance of the AI algorithm plotted against the log of the interferer coherence in array lengths. This example contains a 0 dB broadside target, a 20 dB in-beam interferer, and 0 dB white noise level. There are 20 subarrays and 250 snapshots in this example.

and AI algorithms. The trade-off between algorithms will be discussed further in section 5.2.

In summary, interference decorrelation degrades detection performance. If, however, the interference has decorrelated to the point where its wavenumber spectrum is essentially flat in the vicinity of the target spectrum, its degradation is not as severe. Further, as interferer spectrum spreads, it increases the need for more adaptive degrees of freedom to null the interference. Finally, this requisite adaptivity must be traded against snapshot support in the adaptive subarray algorithms. As will be seen in the next section, decorrelation of the target has a significantly different affect on detection performance.

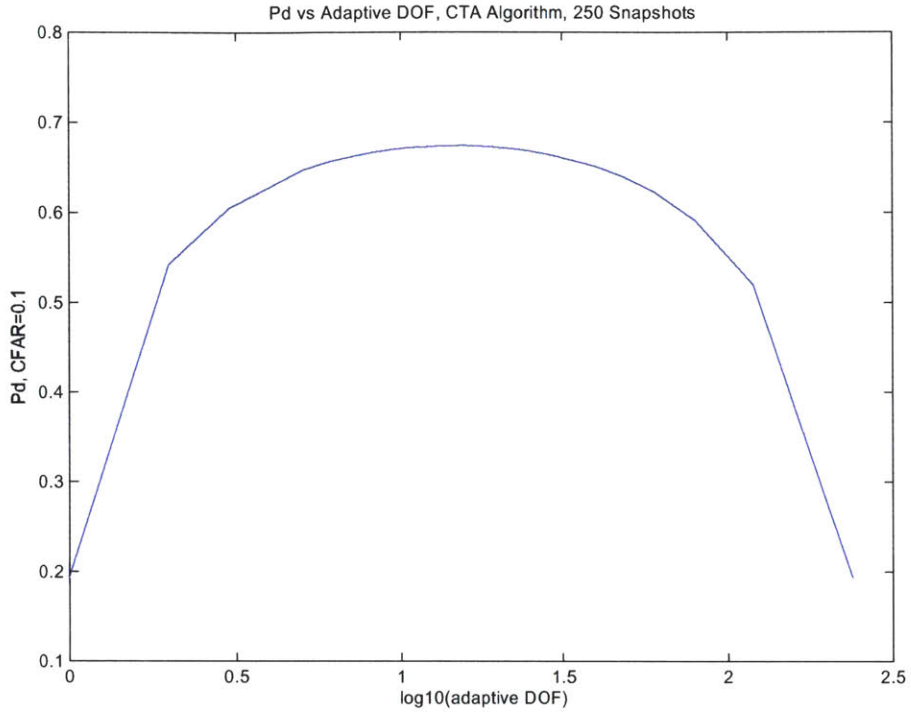

Figure 5-9: Detection performance of the CTA algorithm plotted against the log of the adaptive degrees of freedom. This example contains a 0 dB broadside target, a 20 dB in-beam interferer, and 0 dB white noise level. There are 250 snapshots in this example and an interferer coherence length of 500 elements.

5.1.2 Target Decorrelation

It has been shown in the previous sections that as a signal from a discrete source experiences spatial decorrelation, the wavenumber spectrum spreads, and the eigen subspace spanned by the signal increases in dimension. This is true for all discrete sources, whether emanating from a target of interest or an interference source. The effect on detection performance, however, can be quite different. As shown in the previous section, interference decorrelation decreases the detection performance until the source has decorrelated so much that it is white-noise-like and has less impact on detection performance.

When a signal decorrelates, the signal becomes spread in wavenumber. This results in two things. First, more of the signal may lie in the interference subspace. As interference is removed through adaptive nulling, the signal incurs target self-nulling

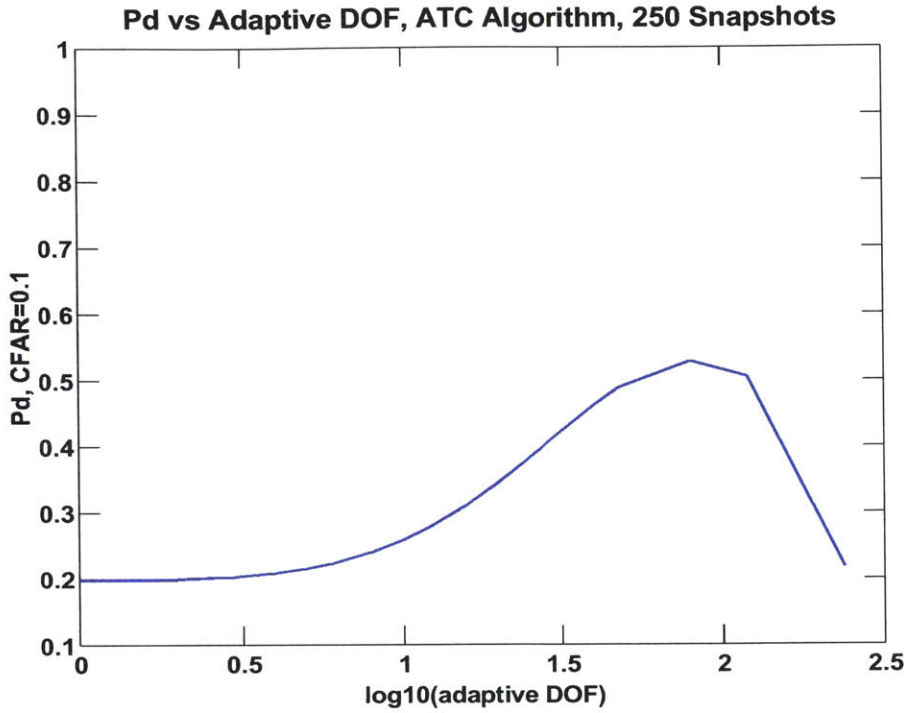

Figure 5-10: Detection performance of the ATC algorithm plotted against the log of the adaptive degrees of freedom. This example contains a 0 dB broadside target, a 20 dB in-beam interferer, and 0 dB white noise level. There are 250 snapshots in this example and an interferer coherence length of 500 elements.

as well. Second, the projection of the signal in the "look direction" decreases as well, leading to a lower signal power. As a result, the effect of signal decorrelation, in general, will be a monotonic degradation of detection performance. Figure 5.12 demonstrates the performance of the CTA algorithm as a function of target decorrelation. This example uses 20 subarrays, 250 snapshots, and a fixed interferer coherence length of 500 elements. The target is at broadside and the interferer is half a conventional beamwidth away at 90.3 deg as in Figures 5.7-5.11. Once the target coherence becomes less than about 3 array lengths, the detection performance degrades.

Figure 5.13 shows the detection performance vs. target coherence for the ATC and AI algorithms. In this case, it appears that the detection performance degrades and then improves again with decreased target coherence. This brings out a very important point in adaptive subarray processing. If one takes a closer look at the

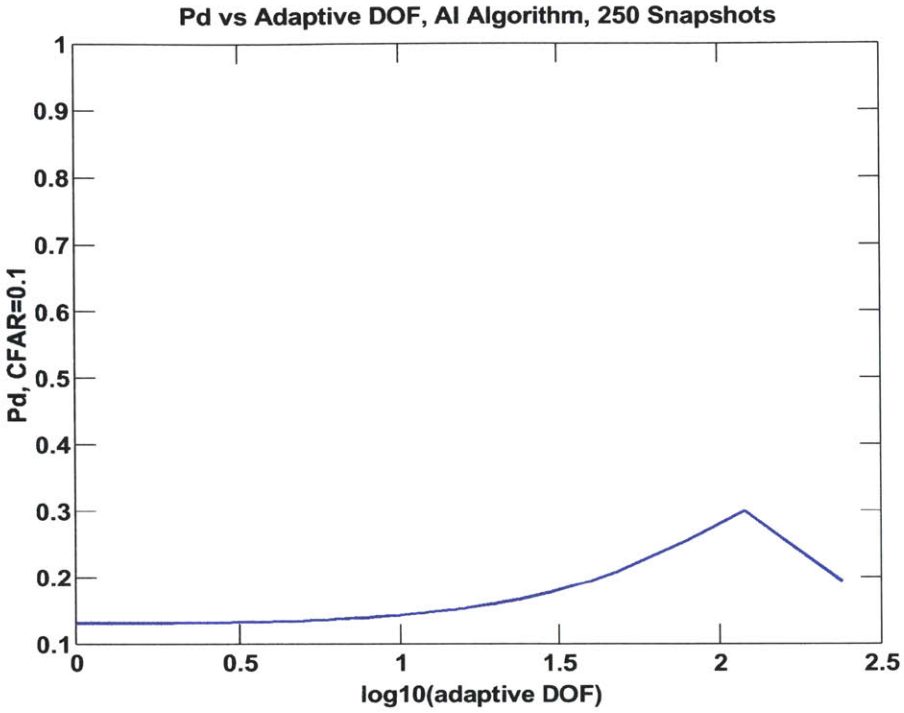

Figure 5-11: Detection performance of the AI algorithm plotted against the log of the adaptive degrees of freedom. This example contains a 0 dB broadside target, a 20 dB in-beam interferer, and 0 dB white noise level. There are 250 snapshots in this example and an interferer coherence length of 500 elements.

performance of all three algorithms for this example, it becomes evident that the ATC and AI algorithms are behaving poorly. The interferer of interest in this case is again half a beam-width away at 90.3 degrees, within the conventional main beam of the full array. As such, the subarrays have even poorer resolution, and it is more challenging to null the interferer. As a result the adaptive subarray weights lead to high white noise gain. The technique mentioned in Chapter 4 of diagonal loading using the white-noise gain constraint (WNGC) would limit this effect. Figure 5.14 shows the beam patterns for the CTA (blue) and ATC (red) algorithms respectively. The ATC pattern has a high "sidelobe" at 78-deg due to a grating lobe of the conventional stage of the processing. The conventional stage of the ATC algorithm in this example, forms the beampattern of a 20-element array spaced (N/M)=12 element spacings apart. This will be inherent in the ATC algorithm due to the sparse array at the conventional

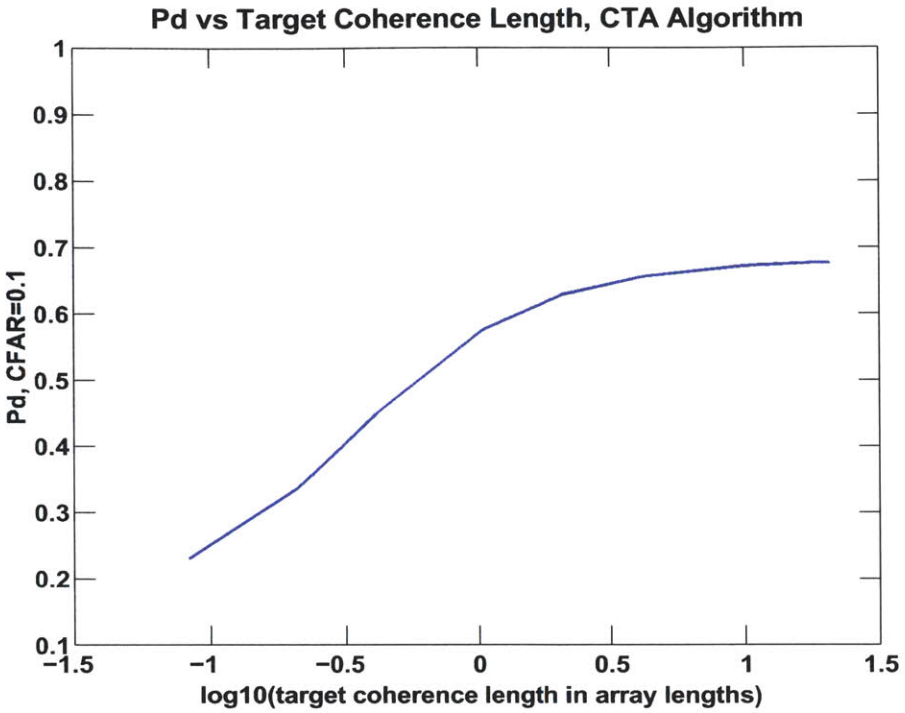

Figure 5-12: Detection performance of the CTA algorithm plotted against the log of the target coherence in array lengths. This example contains a 0 dB broadside target, a 20 dB in-beam interferer, and 0 dB white noise level. There are 20 subarrays and 250 snapshots in this example.

stage. Since the beam-pattern of the adaptive stage, is boosted due to the high white noise gain, this grating lobe is larger than it would be ordinarily. As a result, as the signal decorrelates its wavenumber spectrum spreads, and comes through this grating lobe. While this seems to improve detection, it is a poor practice to operate in a region with such high white noise gain and grating lobes. As will be seen in section 5.2, grating lobes can cause significant difficulties when the environment is dominated by several interferers.

This example of an in-beam interferer proves to be too challenging to the ATC and AI algorithms since it pushes the array into the super-gain region. If instead of having an in-beam interferer at 90.3-deg, there is instead a stronger interferer outside the main beam at 93-degrees, the effect of target decorrelation is consistent across algorithms. Figure 5.15 shows plots of the detection performance for a 20-subarray

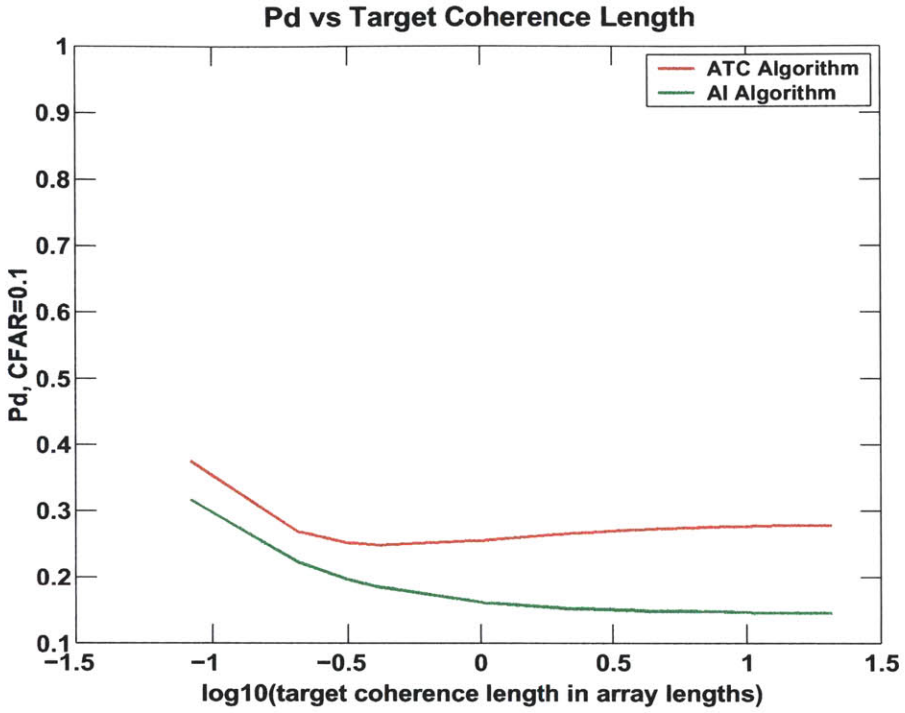

Figure 5-13: Detection performance of the ATC algorithm (in red) and the AI algorithm (in green) plotted against the log of the target coherence in array lengths. This example contains a 0 dB broadside target, a 20 dB in-beam interferer, and 0 dB white noise level. There are 20 subarrays and 250 snapshots in this example.

configuration, 250 snapshots, and interferer coherence of 500 elements. The target strength is -5 dB, the interferer strength is 40 dB, and the white noise level is 0 dB.

In this example, the ATC and AI algorithms have lower white noise gain, so the grating lobe at 78-deg is lower as seen in Figure 5.16. The issue of adaptivity, resolution, and sensitivity will be revisited again in section 5.2. It can be concluded that target decorrelation will degrade detection performance in all cases except those cases when the adaptive stage of the algorithm is performing poorly.

5.1.3 Coherence Effects and Subarray Partitioning

Sections 5.1.1 and 5.1.2 examine the effects of interferer and target decorrelation respectively. This study has illuminated some significant aspects of algorithm performance in this context. It has been seen that white noise gain can significantly impact

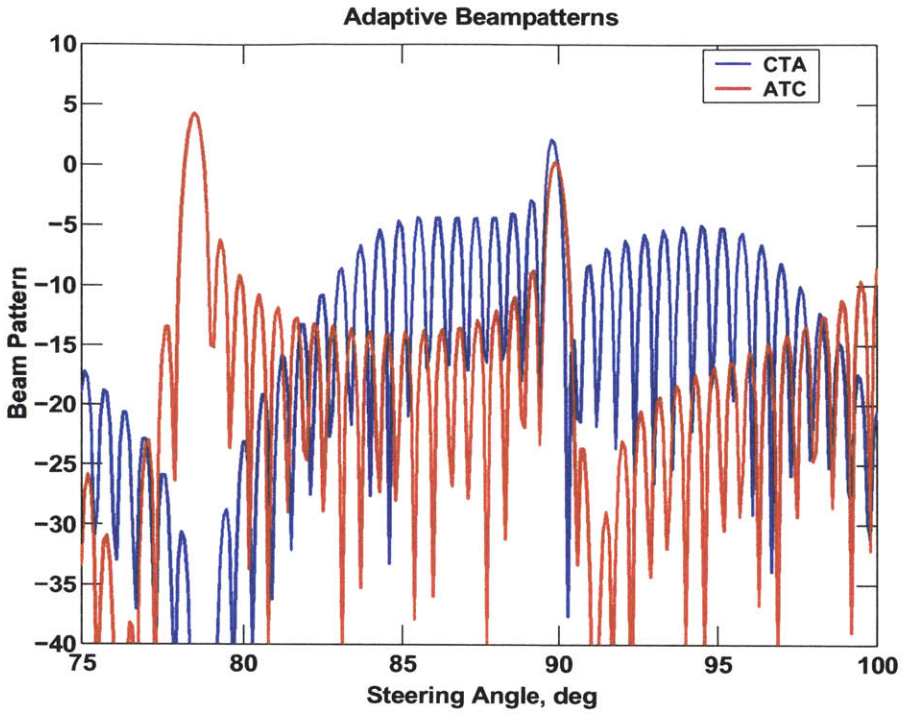

Figure 5-14: Beam patterns of the CTA (blue) and ATC (red) processors in the vicinity of the broadside target. These beam patterns are computed using a 20-subarray configuration with an interferer coherence length of 500 elements.

array performance, particularly in coherence-limited environments.

At this point, since the effects of signal decorrelation have been seen on a general scale, it is useful to examine the manner in which they impact subarray partitioning strategy. This section will examine subarray partitioning schemes in the presence of a nearby interferer. The examples shown here contain a target at broadside, with target level of 0 dB. There is a 20 dB in-beam interferer at 90.3 deg, and a white noise level of 0 dB is used.

CTA Algorithm

First lets examine the subarray partitioning strategy of the CTA algorithm. Keeping in mind that to minimize the computational burden of an algorithm, the partitioning scheme yielding the best performance with the fewest subarrays is the optimal choice. Therefore, if the detection probability is equal for two subarray configurations with a

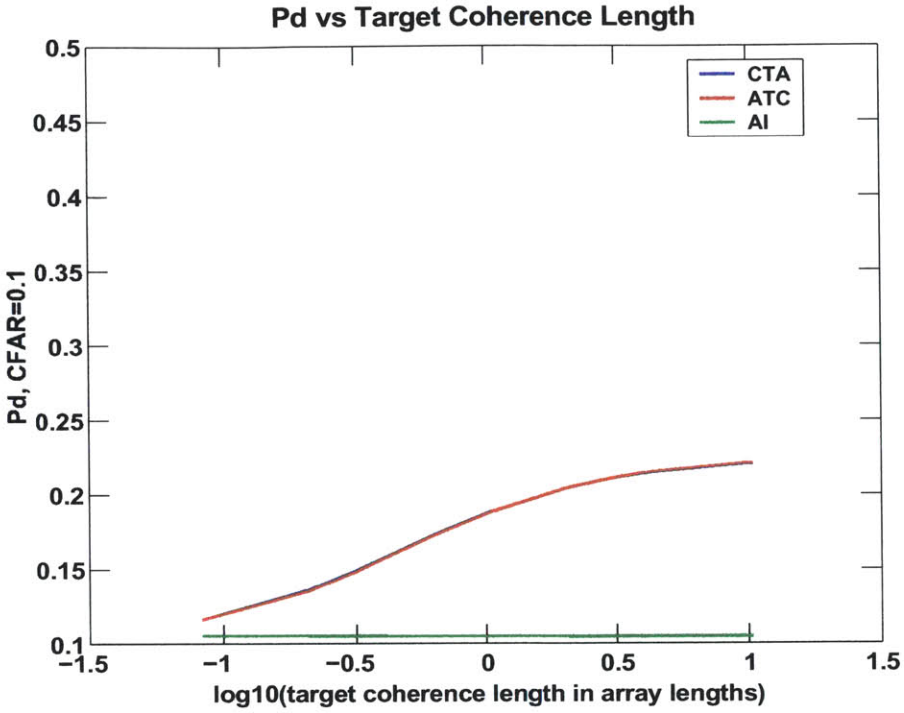

Figure 5-15: Detection performance of the CTA algorithm (in blue), ATC algorithm (in red), and the AI algorithm (in green) plotted against the log of the target coherence in array lengths. This example contains a -5 dB broadside target, a 40 dB interferer, and 0 dB white noise level. There are 20 subarrays and 250 snapshots in this example.

fixed snapshot support, the configuration with the smaller number of subarrays will be considered the optimum. By the same argument, the ATC and AI algorithms would choose the subarray configuration with the larger number of subarrays since that corresponds to a smaller number of sensors per subarray over which adaptive processing is performed.

Figure 5.17a plots the best detection probability for the specified probability of false alarm as a function of interferer coherence on the x-axis and target coherence on the y-axis. Figure 5.17b plots the optimum subarray configuration yielding this Pd as a function of target and interferer coherence respectively. The "optimum" subarray configuration is computed by determining the minimum number of subarrays which attain a P_d greater than or equal to the optimum less 0.01. This buffer of 0.01 is used to ensure that insignificant variations in P_d do not lead to misleading results as

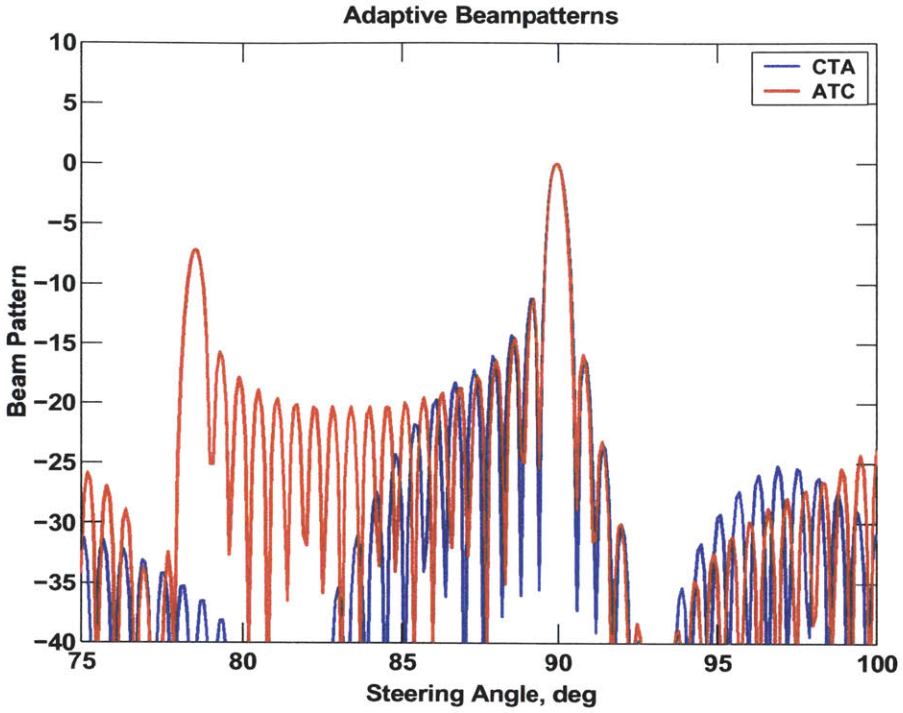

Figure 5-16: Beam patterns of the CTA (blue) and ATC (red) processors in the vicinity of the broadside target. These beam patterns are computed using a 20-subarray configuration with an interferer coherence length of 500 elements, interferer at 90.3 deg.

to the optimum number of subarrays, particularly in the poor-detection regions. The plots shown here are for an example containing 250 snapshots. Several things may be learned from this plot.

First, examine Figure 5.17a. Looking at P_d variation along the horizontal axis, the detection performance degrades and the improves again as interferer coherence degrades. This holds true for all values of signal coherence. The corresponding effect on the optimum subarray configuration is that for a strong, low-rank interferer and high signal coherence, few subarrays are needed to achieve adequate nulling. As the interference coherence degrades, more subarrays are needed, and finally as the interference degrades beyond an array length, fewer subarrays are required to attain adequate detection performance (less adaptivity is required).

At this point, it is useful to make a few observations. First, MVDR processing

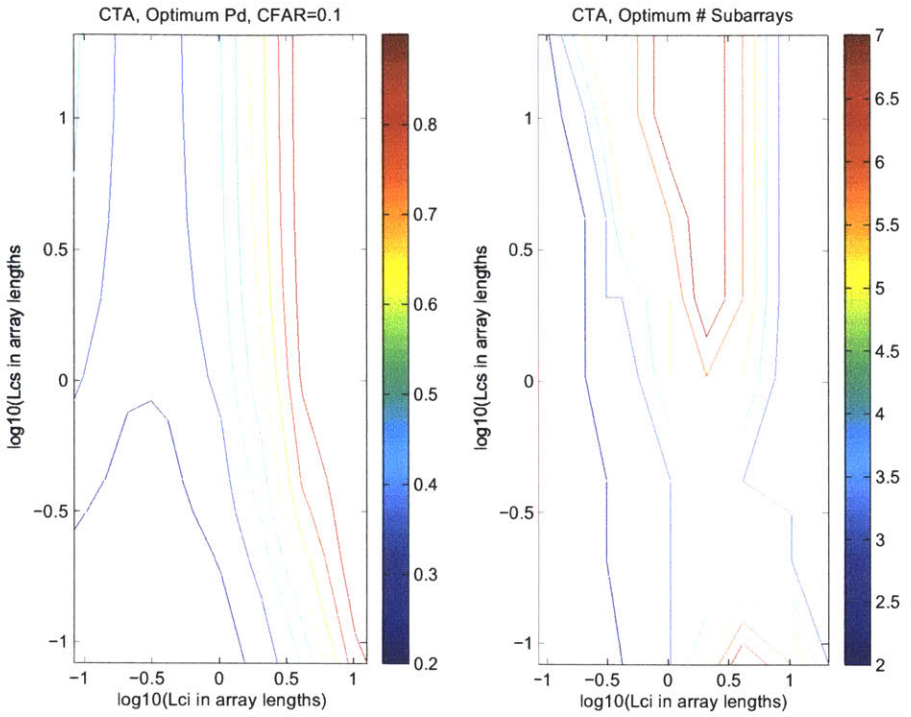

Figure 5-17: Detection performance and optimum subarray configuration of the CTA algorithm as a function of interferer and target coherence for a loud in-beam interferer.

attempts to reject loud interferers which are mismatched to the assumed propagation direction, *i.e.* have large mismatch to the steering vector. As a result, the loudest sources dominate the adaptive weight computation. It is then useful to examine the beam patterns of the CTA algorithm as a function of both target and interference coherence. Figure 5.18 shows the beam patterns for this algorithm for three cases of target coherence for three cases of interferer coherence for a 20 subarray configuration. In the vicinity of the steering vector (90-deg) for high signal coherence lengths, the interferers dominate the adaptive weight computation, and the wavenumber-spreading of the target has very little effect on the pattern. Once the target signal decorrelates beyond an array length, the adaptive stage of the processing begins to adapt to the spread signal resulting in high sensitivity.

Another observation to be made is that there are variations along the signal-coherence dimension. The lower left corner corresponds to low signal and interference coherence. In this region, both the signal and the interference appear white-noise-like.

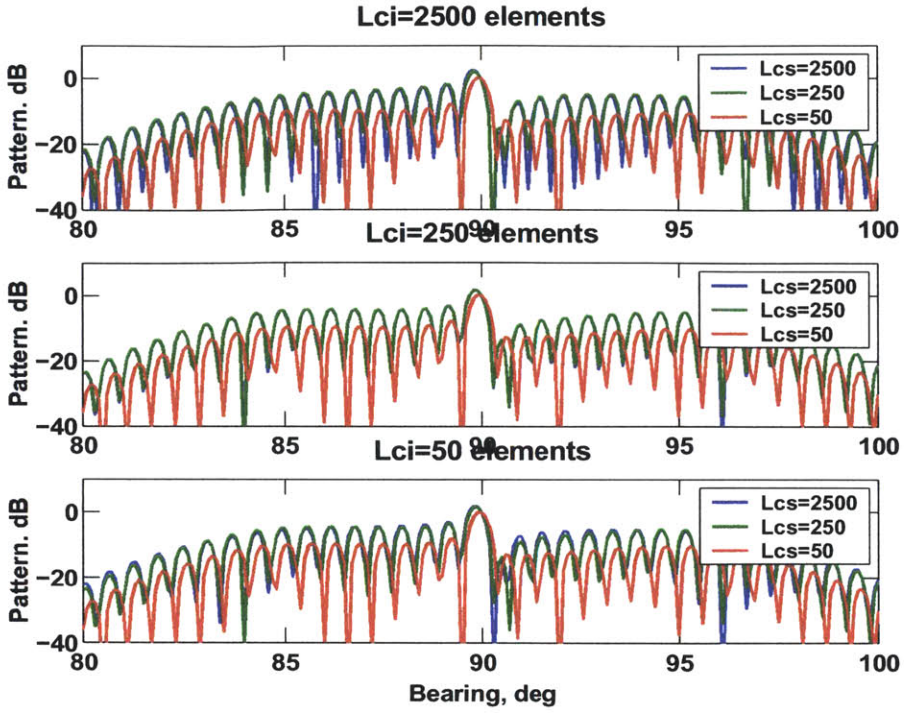

Figure 5-18: Adaptive beam-patterns for a variety of signal and interference coherences. The interference which dominates the adaptive weight computation until the target signal has experienced significant decorrelation.

The detection problem then becomes an issue of detecting two different levels of white noise. Since little is gained from adaptivity, fewer subarrays are needed. The question still remains as to why the performance is not constant vs target decorrelation. The reason for this is that there is a trade-off between how much of the interference is removed and how much of the signal is allowed to pass through. In general adaptivity is needed to remove interference. As the target decorrelates, it is configurations with high side-lobes in the region of the target spread that allows more of the target through. It has been shown that for moderate coherence lengths of the target, as in the case of greatest interest to this thesis, the CTA algorithm does not adapt to the spread target because it its component outside the main resolution beam of the array is much weaker than the spread interference. As a result, high side-lobes prove to be beneficial in this poor detection example. Figure 5.19 shows the beam pattern for configurations of 5, 10, and 20 subarrays for the case of interferer and target

coherence equal to one array length. It should be noted here, however, that detection performance is extremely poor when the signal has decorrelated significantly.

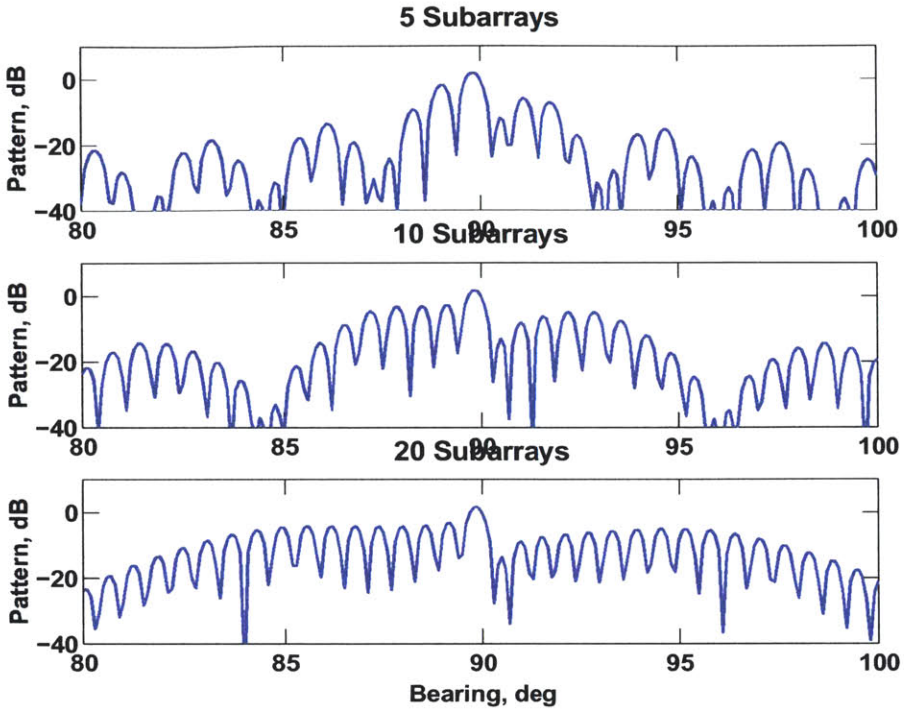

Figure 5-19: Adaptive beam patterns for 5, 10, and 20 subarray configurations. Lcs=Lci=250 elements. High sidelobes in the vicinity of the look direction impact performance.

The study of the CTA algorithm presented in this subsection can be summarized as follows:

1. Adaptive weights are dominated by the interference as long as the interference is significantly louder than the target, even when the interference coherence is low.

2. When the interference source is low rank, an optimal subarray configuration can be found to remove the interference and preserve detection even when the target source has experienced moderate decorrelation.

3. When both the target source has experienced significant decorrelation, and the interference has decorrelated to the point where it cannot be adequately re-

moved, the high sidelobes of the beam patterns with less adaptivity retain more of the target signal, hence providing slight detection performance improvement.

Next the ATC algorithm performance is examined.

ATC Algorithm

The ATC and AI algorithms provide adaptive processing within an array. Therefore, for small subarrays, adaptive resolution becomes an issue. The ATC algorithm retains some of that resolution by coherently combining the subarray outputs. When coherence is very low, the AI algorithm has the potential to improve detection performance by averaging subarray output powers which are essentially independent, thus reducing the variance of the power estimate and potentially improving detection. The question remains if this reduction in variance is more beneficial than the (slight) information that can be gained by coherently processing subarrays which are only slightly correlated. Figure 5.20 shows a comparison of the performance of the ATC and AI algorithms as a function of interferer and target coherence for an example of a broadside target and an in-beam interferer at 90.3-deg, the same example studied in section 5.2.1. It is clear that when the target coherence is high, the ATC algorithm outperforms the AI. In the regions of low target coherence, the ATC and AI algorithms both perform poorly, and there is no benefit to the AI algorithm. For that reason, attention is be devoted to the ATC and CTA algorithms for the remainder of this thesis.

The detection performance of the ATC algorithm shows the same trends as the CTA algorithm as a function of interferer and target coherence. Figure 5.21 shows the detection performance and the optimal subarray configuration for the ATC algorithm as a function of interferer and target coherence. It can be observed from the figure that when the interferer is highly coherent, there may be more subarrays than when the interferer decorrelates. Once the interference has decorrelated beyond half an array length, little is gained from adaptively processing a subarray. Recall that the adaptivity is proportional to subarray size rather than the number of subarrays as in the CTA algorithm. Therefore, as more adaptivity is needed to remove the

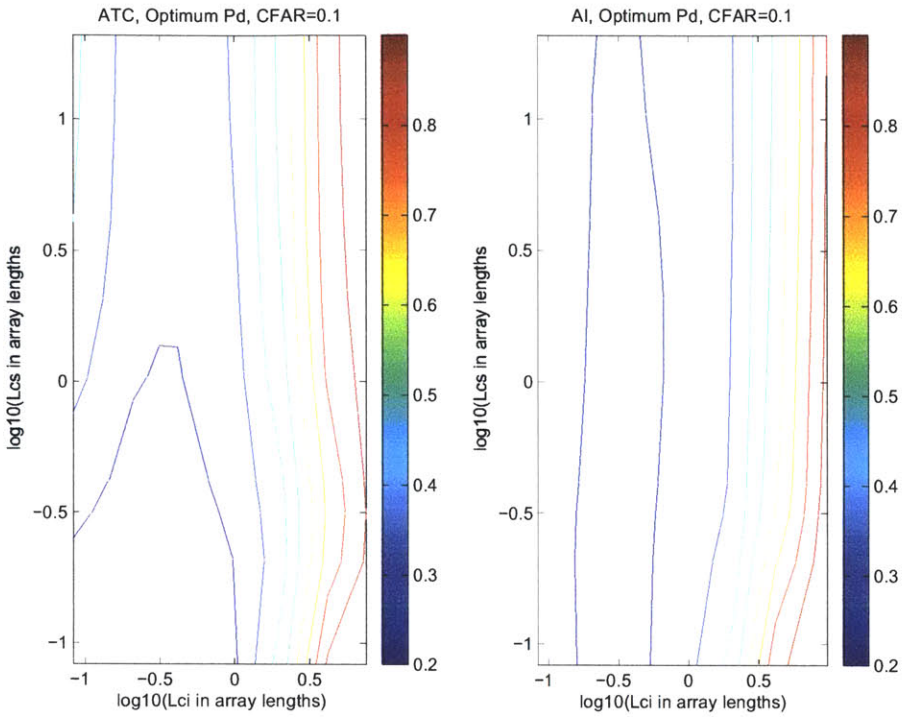

Figure 5-20: Detection performance of the ATC and AI algorithms as a function of interferer and target coherence for a loud in-beam interferer.

interference, fewer subarrays, i.e. longer subarrays, are needed. Finally, when the interference has decorrelated to the point where adaptivity no longer helps detection, the number of subarrays increases again.

An important difference between the ATC and CTA algorithms, is that for low target coherence, the ATC algorithm detection performance improves again. This is a result of two factors. First, the resolution of the subarray is poorer than that of the full array. Therefore, the target spectrum may spread more before the adaptive stage attempts to null its tails. Figure 5.22 shows the beampatterns of the ATC algorithm for a 20-subarray (12 element/subarray) configuration for a variety of coherence lengths of the signal and interferer. In contrast to Figure 5.18, the signal decorrelation has little impact on the beampattern. As mentioned in section 5.1, the reason for this is the high sensitivity of the MVDR processor on the subarrays. This example contains an interferer very close to the target of interest. As a result, the adaptive pattern has very high sidelobes enhanced by grating lobes of the conven-

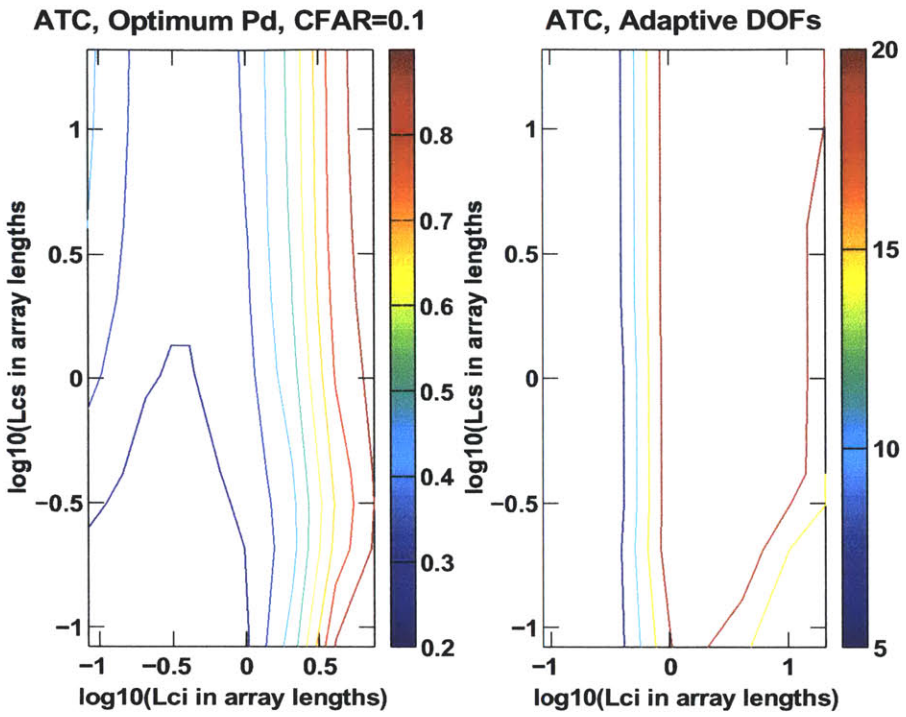

Figure 5-21: Detection performance and optimum degrees of freedom of the ATC algorithm as a function of interferer and target coherence for a loud in-beam interferer.

tional stage that follows. Therefore, the spatially spread target signal comes through these high sidelobes. The sensitivity of the ATC algorithm tends to be higher because the ATC algorithm operates on a subarray with resolution much less than that of the full array. The widening of the interference spectrum stresses the ATC algorithm even more, drastically degrading the performance.

To summarize the effects of coherence on the ATC algorithm:

1. Adaptive weights are again dominated by the interference even more than in the CTA algorithm because of the reduced resolution of a subarray over a full array.

2. When the interference source is low rank, more (smaller) subarrays can accomplish the task of interference rejection

3. High interference decorrelation leads to high sensitivity of the adaptive stage of the processing, leading to high sidelobes. As the signal decorrelates, the poor

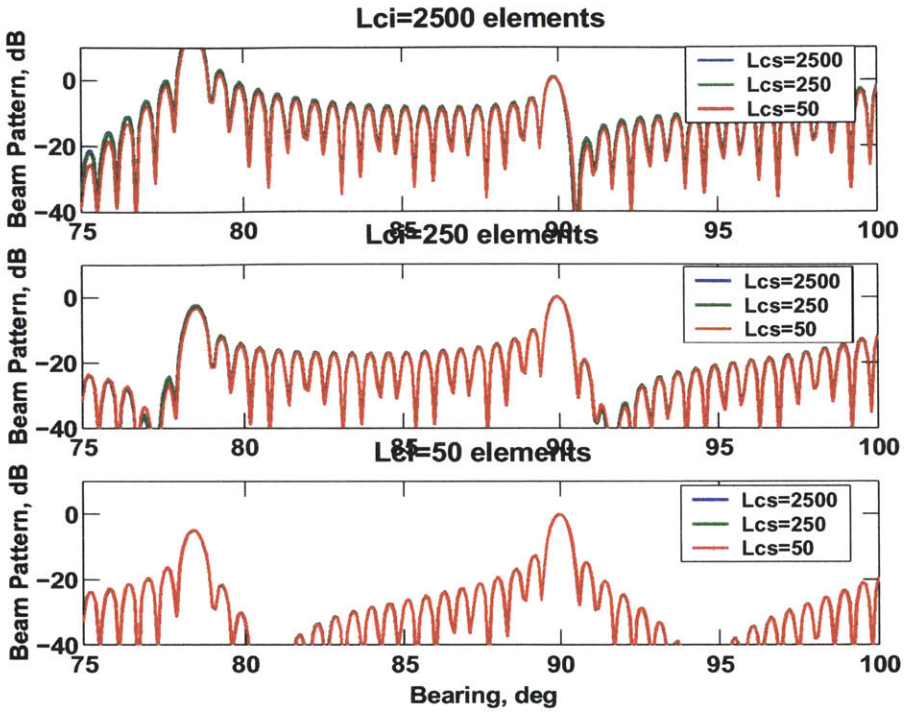

Figure 5-22: Adaptive beam-patterns for a variety of signal and interference coherences. The interference which dominates the adaptive weight computation in the ATC algorithm.

subarray resolution does not allow target self-nulling, and more of the signal passes through these sidelobes improving detection, although high sidelobes are poor practice in general.

This section has used two examples to illustrate the effects of target and interferer decorrelation on detection and subarray partitioning scheme. There are several conclusions that may be drawn.

1. Source decorrelation leads to a spectral spreading of the target and interferer alike.

2. When the interference is significantly louder than the target it is the dominant factor in adaptive weight computation, leaving the signal to pass through whatever spatial filter best removes the interference.

3. White noise gain or sensitivity increases when the adaptivity is applied across

an aperture with limited resolution creating beam patterns with high sidelobes. In regions of poor detectability, these high sidelobes can slightly, though not significantly improve detection performance of decorrelated targets. This practice is not recommended.

4. In all adaptive algorithms there is an inherent trade-off between adaptive degrees of freedom and snapshot support.

These observations are important in the following sections. This section used a single interferer to delineate the effects of snapshot support, target coherence, and interferer coherence. Section 5.2 applies these algorithms to a more practical scenario in which a quiet target is to be detected in the presence of several interferers.

5.2 Algorithm Comparison in Interference-Dominated Environment

Section 5.1 provided several insights into the separate effects of target and interferer coherence as well as snapshot support on the detection performance and optimal partitioning strategy for the CTA and ATC algorithms. The comparison between the two algorithms, however, has been deferred until this time. To examine the relative performance of the CTA and ATC algorithms, a more practical scenario is sought.

The environment presented here is taken from work done for the Acoustic Observatory [48]. The environment contains a quiet target broadside to the array, and 21 loud interferers, representative of surface ships. These surface ships are located at a depth of 5 m in the water column, and are scattered in bearing. The interferers are plotted in Figure 5.23. All of the interferers are assumed to have a power of 160 dB re uPa re 1m and the target is at a range of 15km with a power level of 130 dB re uPa re 1m and a white noise level of 40 dB is assumed. The ranges and depths of these interferers as well as the target will become important in section 5.3 in which MFP performance is presented. This section will focus on the performance of a linear array using a plane wave propagation model in the presence of this interference field.

All propagation to the array is assumed to be plane wave so there is no mismatch between the conventional steering vector and the array response vector aside from the mismatch due to coherence loss. This is chosen as the first approach so the subtleties of these algorithms may be studied without clouding by fading across the array inherent int MFP as well as the effects of the irregular range-bearing sidelobe structure of MFP. This section provides several insights into the performance of these algorithms in a more realistic scenario.

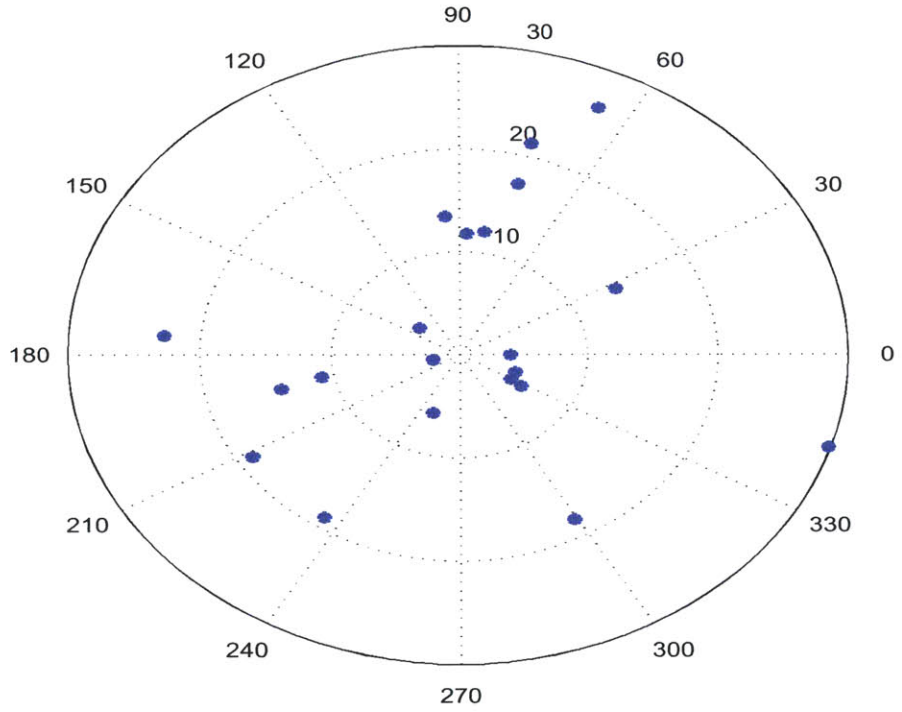

Figure 5-23: Range-bearing locations of interferers in the Acoustic Observatory [ref] environment.

Since this section examines plane wave propagation, the level of the signals impinging on each array element from a given source will be equal. The element-level signal has been computed using the KRAKEN normal model program to compute the average transmission loss from the source to the array for each interferer as well as the target. Element-level target signal is 31.6 dB, and the element-level interferer powers and bearings are provided in table 5.1.

Again, in order to gain insight in to a realistic problem, this section will study the

performance of the CTA and ATC algorithms when the target of interest has a high coherence length (2500 elements, or roughly 10 array lengths) and the interferers all have a nominal coherence length of 50 elements or 0.2 array lengths. The probability of false alarm is 10^{-3}. Recall, however, that the coherence model used in this thesis computes the coherence matrix of a signal based on the component of the inter-element spacing in the direction transverse to the direction of propagation. Therefore there is a variation in the coherence of a source based on its bearing. Endfire sources will be correlated and broadside sources will decorrelate.

The analysis here has fixed the target and nominal interferer coherence. In any practical scenario there is no way to alter the coherence of the ocean environment. The remaining parameters are the number of subarrays and the number of snapshots used in forming the sample covariance matrix. Figure 5.24 shows the detection performance as a function of the number of snapshots and the number of subarrays for the CTA and ATC algorithms.

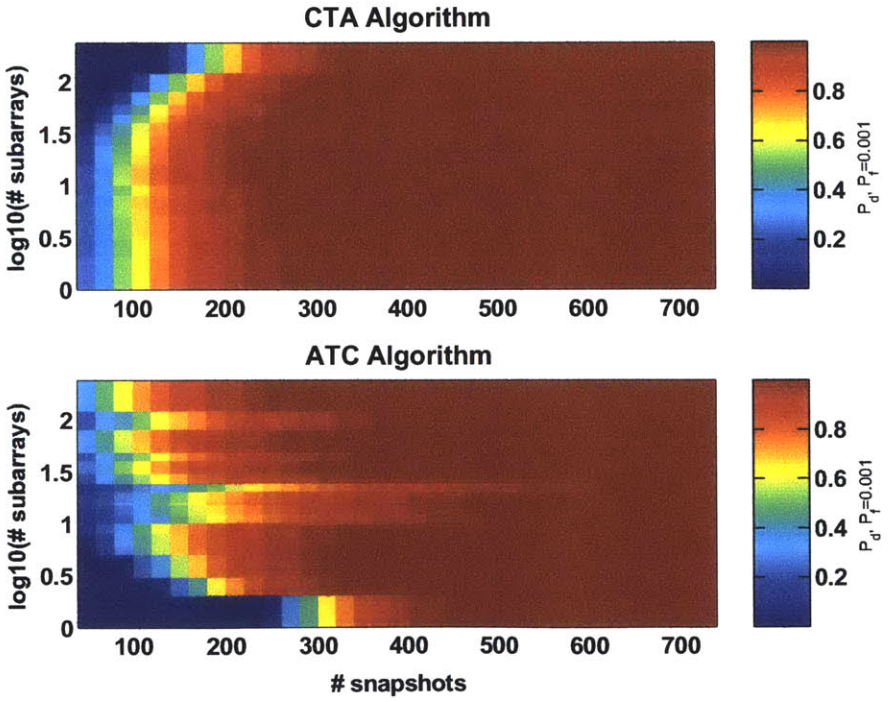

Figure 5-24: Detection performance of the CTA and ATC algorithms as a function of the number of subarrays and snapshots available.

This analysis assumes that all sources are stationary for the specified number of snapshots. In practice, the array size, bandwidth of processing, and interference environment will dictate the number of snapshots available to a given subarray processor. The analysis tools developed in this thesis could be amended to incorporate the effects of source motion, and that will be outlined in the future-work section of Chapter 6.

At first glance two observations may be made as to the relative performance of the algorithms. First, for a fixed snapshot support, the CTA algorithm outperforms the ATC algorithm. Second, the performance of the CTA algorithm is much smoother as a function of subarrays, having a clear optimum subarray configuration where the ATC algorithm does not.

For a fixed number of snapshots, the CTA algorithm has an optimum subarray configuration which is the result of the trade-off between adaptive degrees of freedom required to null the interference and the bias and variance of the power estimate that results from using the sample covariance matrices.

The ATC algorithm performance varies significantly with subarray configuration. This is primarily a result of a poor use of adaptivity and grating lobes in the conventional stage. This variation results in "stripes" in the lower plot of Figure 5.24. This same phenomena also explains why the performance of the CTA algorithm is superior to that of the ATC algorithm. The CTA algorithm performs conventional beamforming at the first stage. As such, interference that is spatially distant from the look-direction is attenuated by the sidelobes of the conventional beam. The adaptive stage is then left to null the interference close to the target look-direction. Further, the adaptivity is applied across subarrays, hence having a large effective aperture. Conversely, the ATC algorithm applies adaptive processing within a subarray. This results in poor performance for two reasons. First, the aperture over which adaptive processing is applied is much smaller. Therefore, the resolution is poorer and it is more difficult to null interference. Second, the MVDR algorithm works to null the strongest interference first. Therefore if there is a loud interferer several beamwidths away from the look-direction and a quieter interferer close to the look direction, the adaptive stage will null the distant interferer first. This is an inefficient used of

adaptive degrees of freedom, since the conventional stage would attenuate the distant interferer in most cases. Also, the conventional stage of the ATC is subject to grating lobes for many subarray configurations. Therefore, even if a distant interferer is attenuated by the adaptive stage, at some bearings there will be no further attenuation by the conventional stage.

This explanation is best seen through the following plots. Figure 5.25a shows the CBF beam pattern for a 12-element array. This is the pattern for a single subarray steered to the target direction. Note that there are two main-lobe interferers at the subarray level. The interferer bearings are denoted by red stars. Since the conventional beam pattern rejects some of the out-of-beam interferers, it leaves the adaptive stage to null main-beam interference. Figure 5.25b shows the pattern after the adaptive stage of the CTA algorithm, also for the 20 subarray configuration. Again the interferer bearings are denoted by red stars. One may observe that all interferers receive significant cancellation leading to fair algorithm performance.

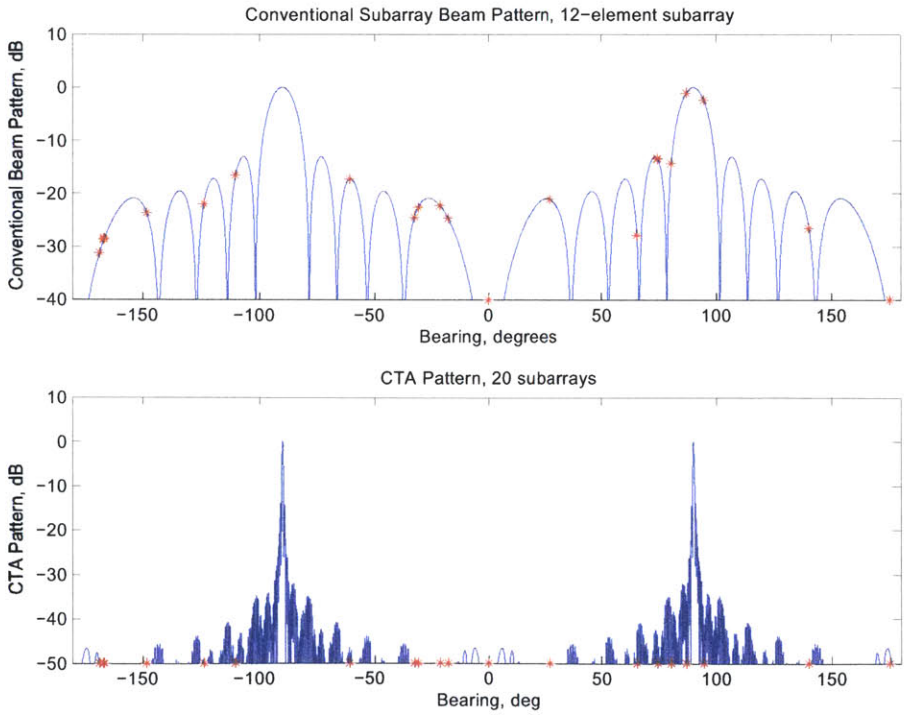

Figure 5-25: Beam patterns at the conventional stage (top) and composite CTA (bottom) with interferer locations superimposed.

Figure 5.26a shows the adaptive pattern of a 20-element subarray corresponding to the case of a 20-DOF ATC algorithm. Again, the interferers are marked by red stars. The loudest interferers are nulled first, many of which are spatially separated from the target. There are, however, main-lobe interferers which are not nulled since the adaptive subarray processing lacks sufficient resolution. Figure 5.26b shows the conventional beam pattern for sensors located at the center of each subarray. Since these subarrays are spaced greater than 0.5 wavelengths apart, there are grating lobes in the pattern. At the locations of grating lobes, no further attenuation of interference is provided. As a result, some interference is significantly under-nulled.

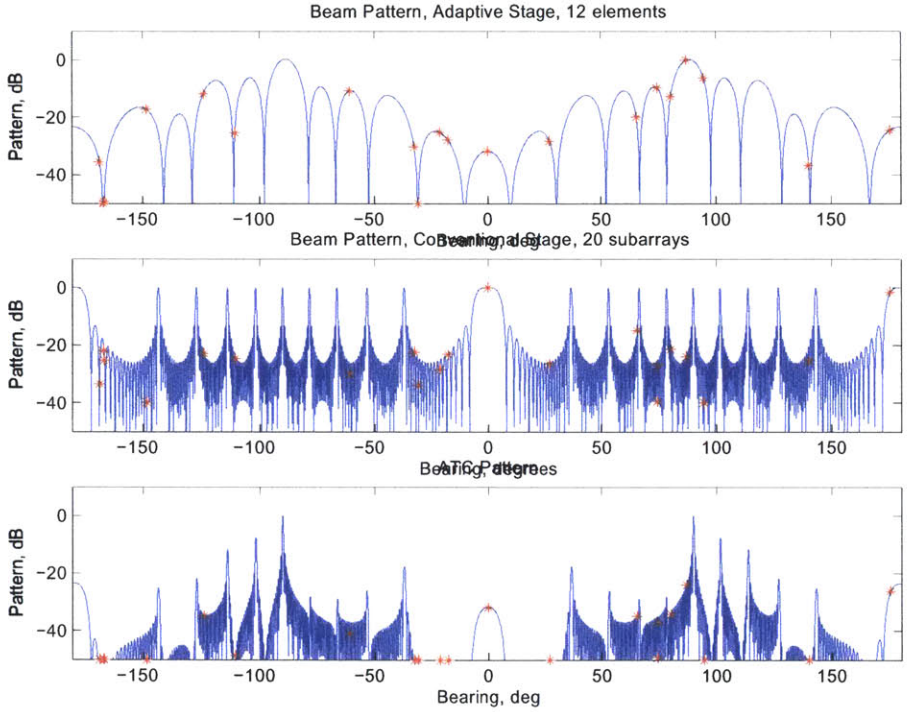

Figure 5-26: Beam patterns at the adaptive stage (top), conventional stage (middle) and composite ATC (bottom) with interferer locations superimposed.

Table 5.1 shows the element-level interferer power, bearing, and nulling at each stage of the processing for the CTA and ATC algorithms and a 20-subarray configuration. The CTA has a more efficient use of adaptivity even though the adaptive processing is applied across an aperture which is possibly not coherent.

Note that the patterns plotted in this case are based on adaptive weights formed

Int. Bearing	Int. dB	CTA Nulling, dB			ATC Nulling, dB		
		CBF	ABF	Total	CBF	ABF	Total
0	68	50	0	50	0	32	32
74.5	54	13	38	51	27	10	37
86.9	55	1	35	36	24	0	24
94.6	60.5	2	67	69	49	6	46
-110.1	61.6	17	34	51	24	25	49
27.6	55.6	21	30	51	26	28	54
-166.5	73.6	29	45	74	34	55	89
-30.7	66.6	22	52	74	34	55	89
175.4	50.9	47	1	48	1	25	26
-148.2	52.9	24	36	60	35	17	52
-21.1	66.2	22	35	57	28	25	53
-168.4	58.4	31	23	54	33	36	69
74.3	55.7	13	37	50	40	10	50
-166.3	55.6	29	27	56	25	49	74
-60.7	52.9	17	33	50	30	11	41
-123.7	53.0	22	34	56	23	12	35
140.2	68.1	26	38	64	25	37	62
65.4	49.8	28	14	42	15	20	35
-17.5	47.8	25	27	52	23	28	51
80.4	60.4	14	33	47	21	13	34
-32.3	64.2	24	34	58	22	30	52

Table 5.1: CBF and ABF nulling of CTA and ATC algorithms.

from clairvoyant covariance matrices. As the analysis in Chapter 4 showed, the sample-based power estimates are functions of the clairvoyant power estimates and the number of snapshots. The number of snapshots will alter the bias and variance, and hence the statistical properties of the detection, but the clairvoyant power estimates are a critical component.

The conclusions drawn here are consistent with the work of Nuttall [12]. While he examined the performance of an adaptive/adaptive processor, he came to the conclusion that the first stage of the processor, i.e. the processing within a subarray, must be forced to null interference which is spatially distant from the look-direction. Otherwise, significant white noise gain resulted and performance was poor. In that case, the second stage of the processing had larger effective aperture, and hence better resolution. It was therefore easier to null in-beam interference. In the CTA vs ATC study, it is better to apply the adaptivity to the second stage for two reasons. First, if there are many interferers the conventional stage at the start will eliminate interference which is spatially distant and therefore easy to remove. This allows the nearby interference to be rejected by adaptive processing applied to a large aperture hence keeping reasonable white noise gain. Second, if there are only main-beam interferers, it is better to null them with an array with high resolution rather than a subarray. Attempting in-beam interference cancellation with a subarray would lead to either high white noise gain or larger subarrays with more adaptive degrees of freedom and more calculation burden.

Examples using a plane wave model have been used to establish the effects of target and interferer coherence on detection performance and subarray partitioning scheme. It has been shown that there is a trade-off between adaptivity and snapshot support. Finally, the CTA and ATC algorithms have been compared showing that it is more efficient for the adaptivity to be applied at the second stage since distant interference can be removed to some degree by first-stage conventional processing. Further, the resolution afforded by adaptive processing across a large aperture, even when the signals are decorrelated, proves to be beneficial. The following section examines algorithm performance in the context of Matched Field Processing. First,

the performance is shown using a single line array and second a planar array.

5.3 Matched Field Processing via adaptive subarray algorithms

This section considers subarray processing in the context of Matched Field Processing in coherence-limited, snapshot starved environments. The interference environment presented in section 5.2 was developed in the context of a shallow-water environment dominated by surface ships. This section uses this same interference field to examine the performance of MFP in a coherence-limited environment. Recall from Chapter 2 that using a full-wave propagation model leads to the potential for an array to resolve sources in range, depth, and bearing. Therefore discrimination of surface from submerged sources is possible if the array had sufficient resolution.

Section 5.2 examined performance using a plane-wave propagation model and a plane-wave steering vector. The signal level on each array element was identical. That allowed for the study of the effects of coherence and snapshots without clouding the analysis with fading across the array and the like. In this section, both the signals and their replicas are generated using the KRAKEN normal mode program. To again simplify the problem at hand, it is assumed that the propagation environment is known exactly. That will never be the case in practice, as one can not determine the SVP and bottom properties everywhere, but the goal of this study is to determine the effects of coherence on array partitioning. That is more easily accomplished without incorporating environmental mismatch (other than that resulting from coherence loss) into the problem.

The environment used here has a simple downward-refracting sound speed profile and a fast bottom. The sound speed, density, and attenuation in each layer is shown in Figure 5.27. The sub-bottom is modeled as an isovelocity half-space.

All interferers are modeled as 160 dB point sources at a depth of 5 m. The target is also a point source at a depth of 100m and a range of 15km. The range, bearing,

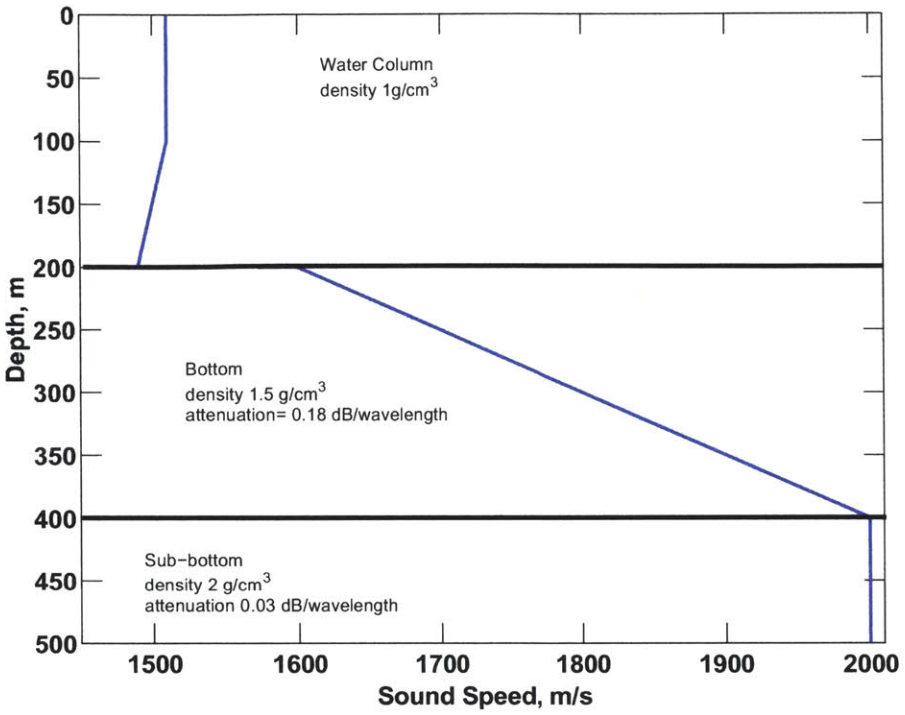

Figure 5-27: Propagation environment for MFP analysis.

and average TL across the array of each interferer is provided in Table 5.2. Section 5.3.1 will study the partitioning using a single line array, and section 5.3.2 examines the performance of a planar array using MFP.

5.3.1 Single Line MFP Subarray Processing

In Section 5.2 the behavior of the subarray processing algorithms were studies through the use of adaptive spatial beam patterns. Since a plane wave model was used, the array was only able to resolve things in one dimension, azimuth. As a result, with conventional processing, the highest sidelobes (i.e. spatial locations with the least mismatch to the main beam) were spatially close to the look-direction.

Alternatively, Matched Field Processing has the potential for resolving source in 3 dimensions, and therefore has a three-dimensional spatial beam pattern. As a result, the highest sidelobes do not necessarily lie in spatial proximity to the look-direction. Therefore, examining the nulling of each stage of the processing requires looking over

index	Range, km	bearing, deg	Avg. TL, dB
1	4	0	92.2
2	21.3	74.5	106.1
3	11.7	86.9	105.1
4	13.4	94.6	99.5
5	6.0	-110.1	98.4
6	13.8	27.6	104.4
7	2.1	-166.5	86.4
8	4.6	-30.7	93.4
9	22.7	175.4	109.1
10	18.8	-148.2	107.1
11	4.7	-21.1	93.8
12	10.9	-168.4	101.6
13	17.2	74.3	104.3
14	14.2	-166.3	104.4
15	18.3	-60.7	107.1
16	19.0	-123.7	107.0
17	4.0	140.2	91.9
18	26.3	65.4	110.2
19	29.9	-17.5	112.2
20	12.0	80.4	99.6
21	5.7	-32.3	95.8

Table 5.2: Range, Bearing, and Average TL to the array for interferers in AO environment.

3 dimensions. The resolution, however, is a result of the array itself. Figure 5.28 shows the CMFP and AMFP beam pattern using the full array. The array is focused at the target location of 15km, 90-deg, 100m depth. The beam pattern shown here is computed at 5m depth, i.e. the interference depth, and is plotted for range and bearings covering the interferers in this scenario. It is evident that this array has very poor depth resolution at broadside since the beam pattern is approximately 0 dB at broadside at the interferer depth.

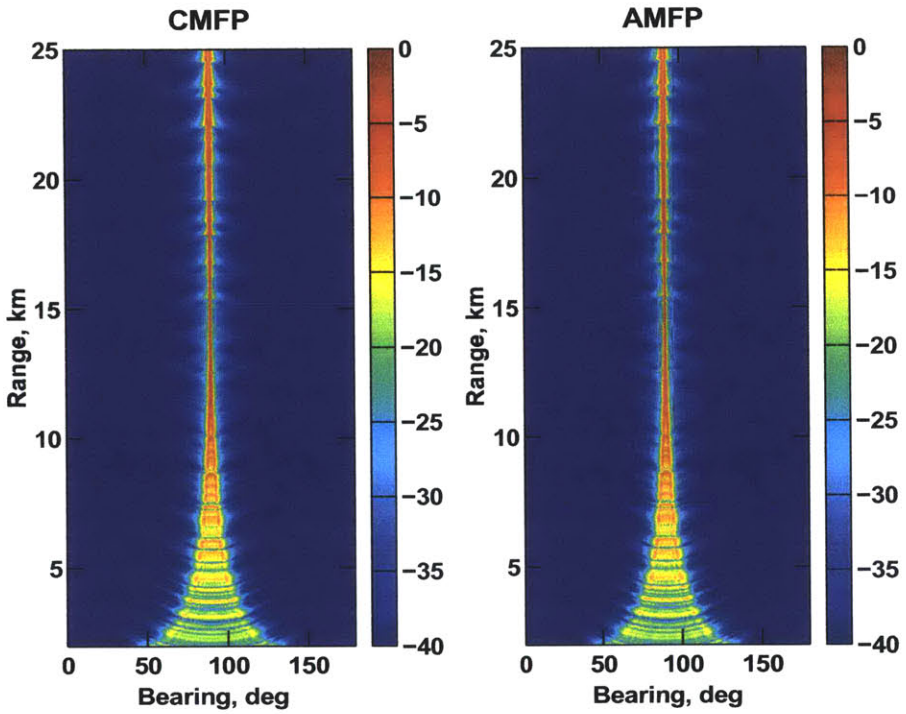

Figure 5-28: CMFP and AMFP beam pattern at interference depth for full array steered to 100m, 15km, and 90-deg.

There appears to be little difference between the AMFP beam patterns and the CMFP beam patterns in this plot. On this color-scale, most of the interference rejection shown results from angular resolution of the array. If the plot is examined more closely, however, it can be seen that the AMFP beam pattern rejects targets, even in range. Figure 5.29 shows the pattern as a function of range at a bearing of 0-deg (endfire). There is an interferer at 0-deg, 4km. The AMFP pattern shows a null at this location where the CMFP pattern does not.

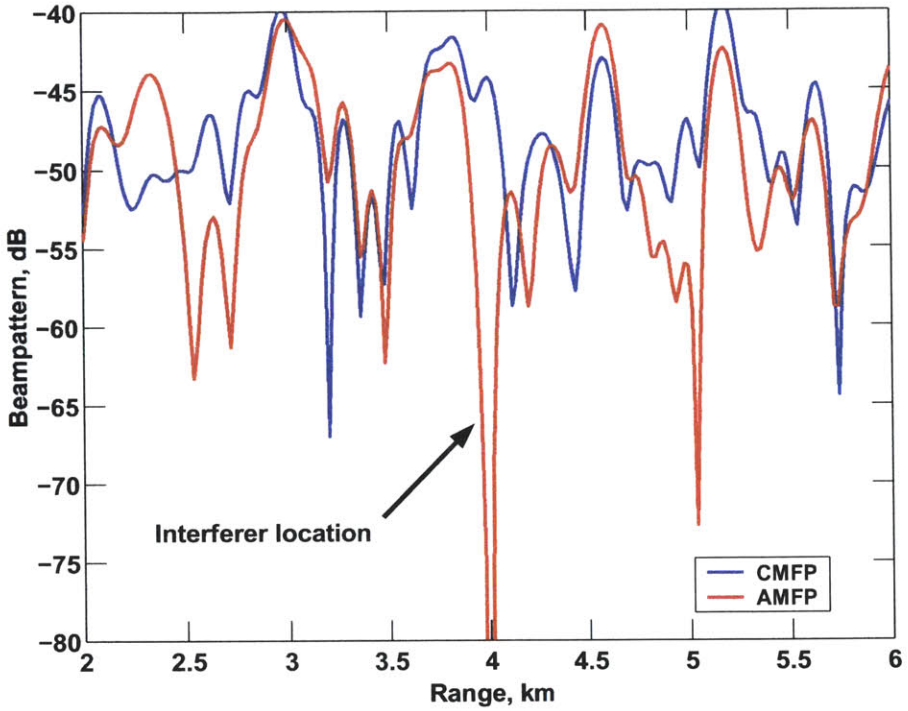

Figure 5-29: CMFP and AMFP beam pattern at interference depth, 0-deg bearing vs range for full array steered to 100m, 15km, and 90-deg in the vicinity of an interferer at 4km.

Since the focus of this work is to examine the impact of coherence degradation on array partitioning strategy, it is useful to examine the detection performance of the CTA and ATC algorithms. Figure 5.30 shows the detection performance and optimum subarray configurations of the CTA algorithm as a function of interferer and target coherence for 250 snapshots.

As seen using the plane wave model, detection performance degrades as target coherence degrades. Also, as the interferer coherence degrades, detection degrades as well. In this case there is too much interference for the detection to improve again, even when the interference is significantly decorrelated. Also, when the interference and target are highly correlated, CMFP (i.e. 1 subarray) is sufficient for optimum detection. As the interference decorrelates, more and more subarrays (i.e. more and more adaptivity) is needed to remove the interference until some of the interferers have decorrelated to the point where adaptivity is no longer helpful at removing them

(i.e. white-noise-like region). The effects here are the same as those seen using the plane-wave model.

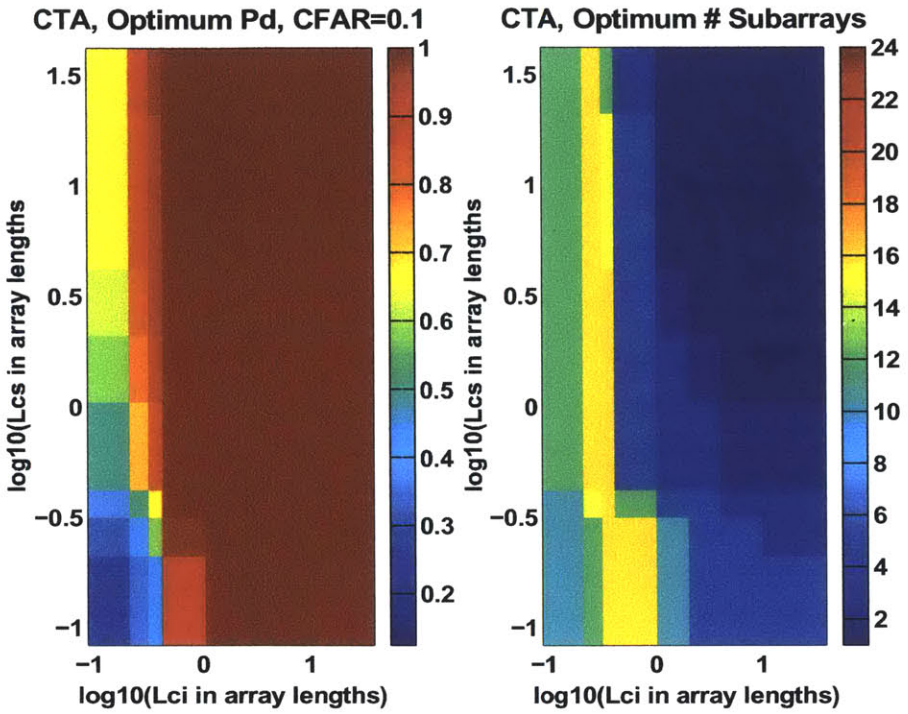

Figure 5-30: Pd vs coherence (a) and optimal subarray configuration adaptive degrees of freedom vs coherence for the CTA algorithm.

Figure 5.31 shows the same plots for the ATC algorithm. Again it is seen that for many coherences, little adaptivity is needed (blue regions) because either CMFP removes the interference (high coherence regions) or little is gained through adaptivity (low interferer coherence regions). When adaptivity is needed, several adaptive DOFs are required because the adaptive resolution is that of a subarray rather than the full array as discussed in Section 5.2.

Following the analysis of Section 5.2, examine the performance for a fixed coherence scenario as a function of subarray configuration and snapshot support. Figure 5.32 shows the performance for an example of high target coherence (2500 elements) and low interference coherence (50 elements). The top figure shows the performance of the CTA algorithm and the bottom figure shows the performance of the ATC algorithm. As was seen in the plane wave example, the CTA performance is much

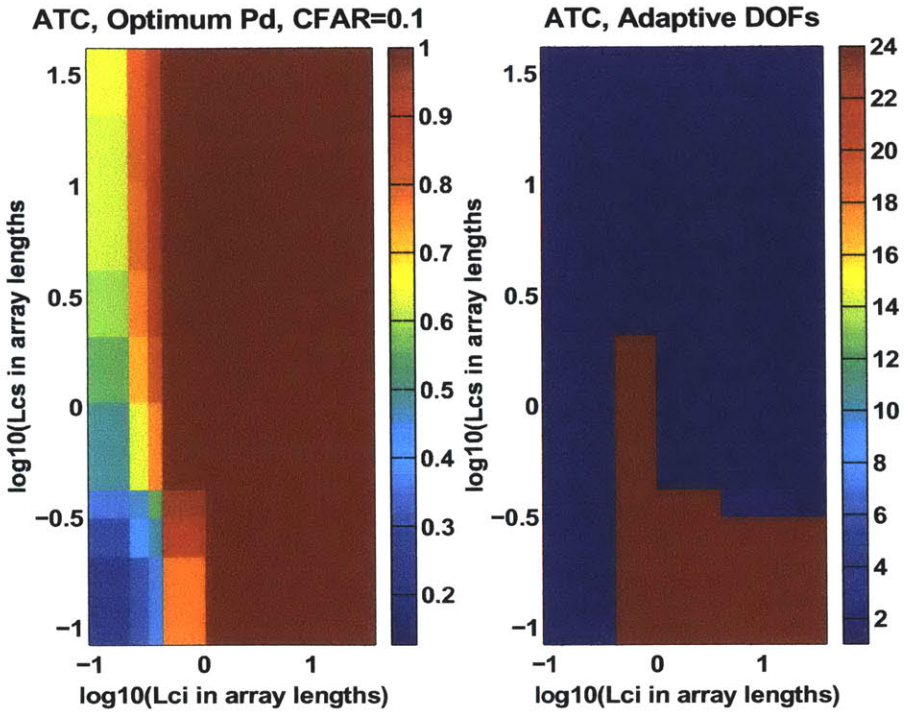

Figure 5-31: Pd vs coherence (a) and optimal subarray configuration adaptive degrees of freedom vs coherence for the ATC algorithm.

smoother as a function of subarrays than the ATC algorithm. In fact, with MFP, the differences are even more dramatic. This is again a result of performing adaptive processing within a subarray in the ATC algorithm. The adaptive stage attempt to remove strongest interference first, and when challenged, becomes very sensitive. As mentioned above, MFP has an irregular sidelobe structure, and results in little nulling at the conventional stage.

One may note that for a broadside target, there is little fading of the signal of the signal of interest across the array. When considering MFP, however, particularly at angles off broadside or in the context of planar arrays, there may be significant fading across the array due to constructive and destructive interference of multipath. It is then important to examine the impact of such fading on the detection performance of the algorithms.

Figure 5.33 shows the detection performance of the CTA and ATC algorithms for a target at 10-deg and a range of 15km. The interference field remains as described

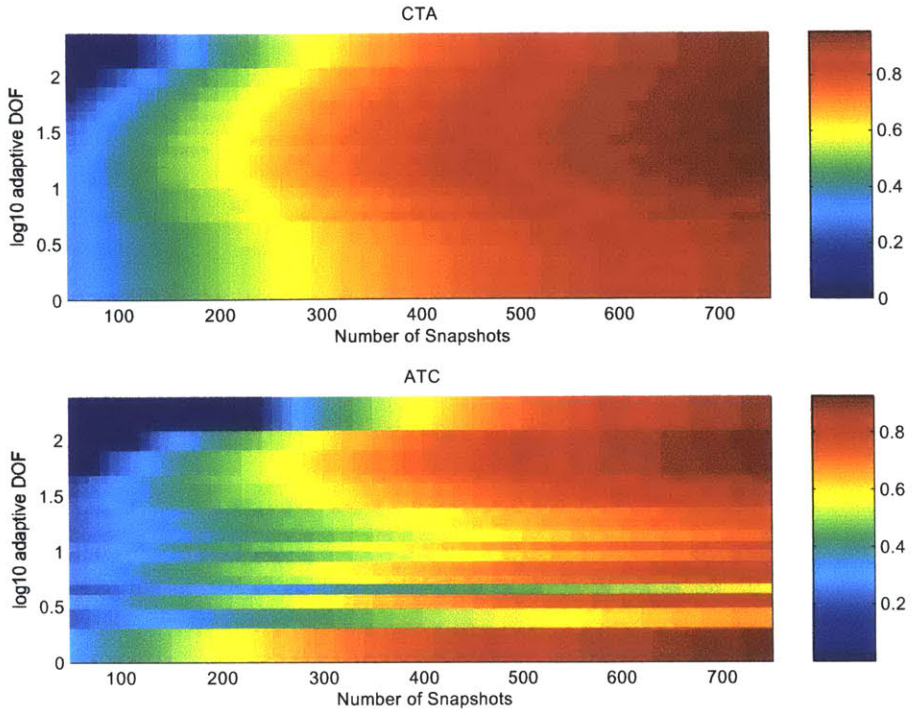

Figure 5-32: Pd vs adaptive DOF and snapshots, CTA and ATC algorithms.

in Figure 5.22. In this case, it is clear that the CTA algorithm is far superior to the ATC algorithm. The factors of resolution and nulling at each stage discussed above still hold, but fading across the array introduces another factor.

Note that the performance is best for an array with approximately 48 adaptive DOFs available. This corresponds to a CTA configuration with 48 subarrays and an ATC configuration with 5 subarrays. Figures 5.34 and 5.35 demonstrate the fading across subarray after the first processing stage for a broadside target and an endfire target. The difference is far more dramatic for the ATC algorithm, and leads to poorer performance in the endfire configuration.

At this point some conclusions may be drawn about the performance of the adaptive subarray algorithms using MFP.

1. Target and interferer decorrelation impact subarray algorithm performance in the same manner as with a plane wave model, indicating that the fading across the array has little impact on these phenomena with this coherence model.

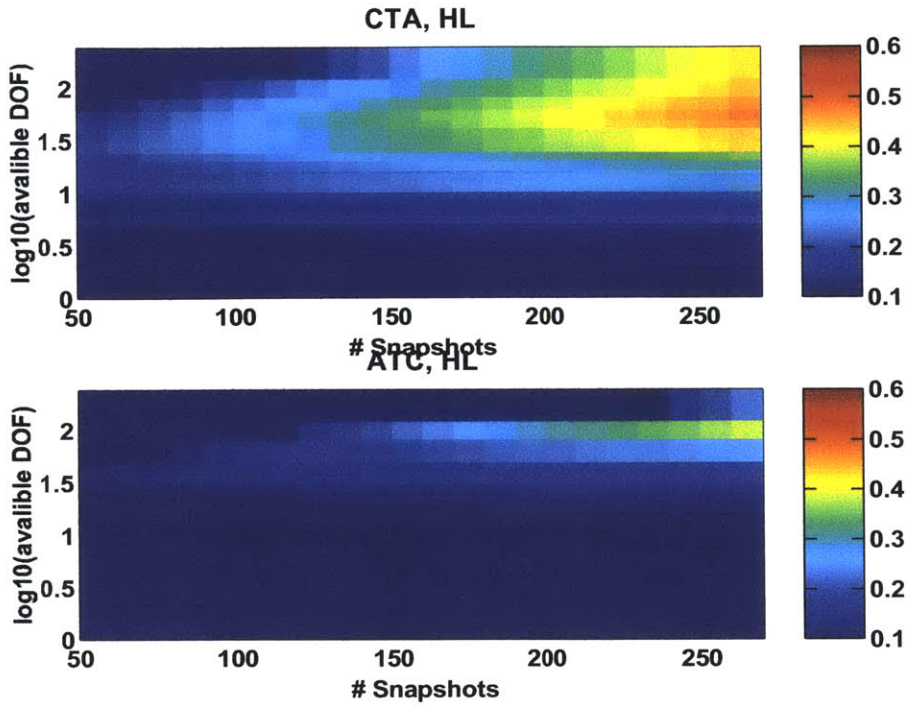

Figure 5-33: Pd vs adaptive DOF and snapshots, CTA and ATC algorithms, target at 10-deg, 15km.

2. The CTA algorithm is far superior to that of the ATC algorithm in an MFP arena due to the high spatial ambiguities inherent in the conventional Matched Field Processor as well as its resistance to fading across the aperture.

3. Interferers nulled at each stage are no longer appropriately determined using the azimuthal beam pattern since the beam pattern varies a functions of range and depth as well.

The next section examines the detection performance of the CTA and ATC algorithms using MFP and planar towed arrays.

5.3.2 Planar Array MFP Subarray Processing

It was shown in section 5.3.1 that the ATC and CTA algorithms have the same general performance trade-offs as in plane wave processing. Namely, the conventional and adaptive patterns can be computed to show that the CTA algorithm has a more

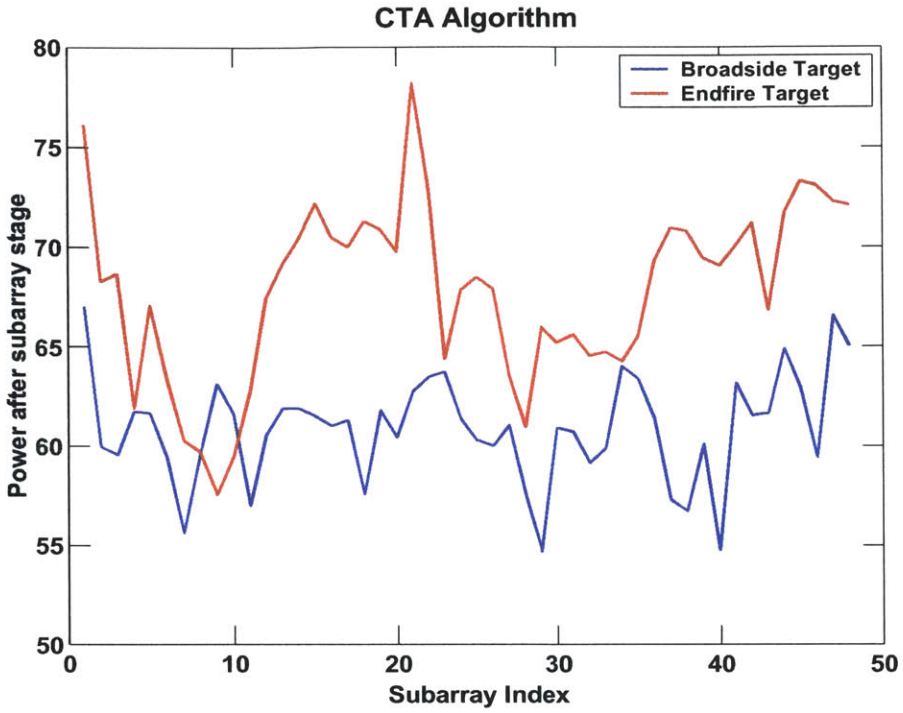

Figure 5-34: Power on each subarray after the first stage of processing for the CTA algorithm, broadside target and endfire target.

efficient use of its adaptivity, leading to more consistent detection performance as a function of subarray partition. It was also shown that the nonlinear sidelobe structure of the plane wave model leads to an interferer's range and depth dictating its impact on detection performance rather than its bearing alone. The third point to recall is that the resolution of the aperture over which the adaptive processing is performed is important as well in preventing high white noise gain of the processor. This led to a trade-off between resolution and adaptivity which added to the trade-off between adaptivity and snapshot support. This section examines the performance of a planar array in the context of MFP.

Recall from Chapter 2 that the full-wave propagation model led to potential resolution of a source in range, depth and bearing. Recall also that the realizable resolution, however, was dependent upon array geometry and orientation. The advantage of the planar array was that it had the potential for range resolution through mode sampling at all target bearings since a planar array always had some projected verti-

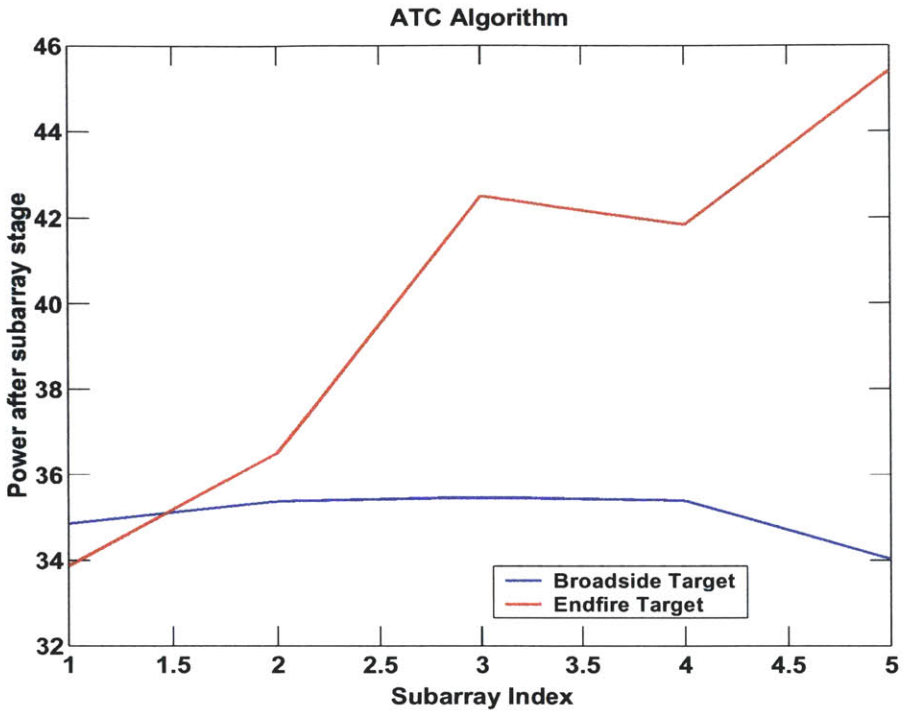

Figure 5-35: Power on each subarray after the first stage of processing for the ATC algorithm, broadside target and endfire target.

cal aperture. While the addition of multiple streamers has the potential to improve detection performance, it also increases the number of sensors hence increasing the requisite snapshot support for adaptive processing.

This section examines the trade-off between resolution, adaptivity, and snapshot support for a 4-streamer planar array and compares the performance to that of the single-line towed array, all using MFP. The addition of a planar array leads to the need for new notation. Up to this point, the number of subarrays has been specified, and all partitions have been along the length of the array, or along the y-direction. With a planar array, there are now two dimensions over which the array may be partitioned. The subarray configuration will now be referred to by the number of subarrays in the x-direction and the number of subarrays in the y-direction. Figure 5.36 shows sample partitions indicating this notation.

Figure 5.37 shows a plots of the detection performance of a single streamer as well as that for 1x, 2x, and 4x configurations as a function of the number of subarrays

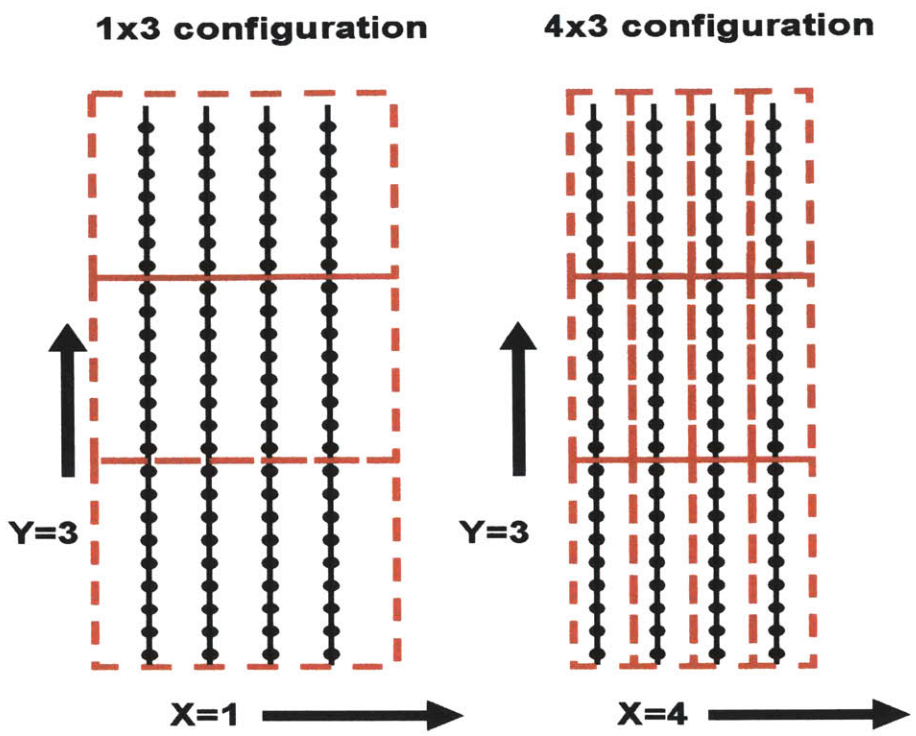

Figure 5-36: Subarray configuration nomenclature.

along the length of the array and number of snapshots for the CTA algorithm.

Recall that one benefit to a planar array, even with plane wave processing, is that the symmetry of the propagation environment is broken and the array response to a source to the right of the array is now different from the response to a source to the left. In this example, the streamers are spaced roughly a quarter-wavelength apart at the operating frequency. The reason for this is that at quarter-wavelength spacing in plane wave processing, a twin-line array has the best left-right rejection as a function of scan angle.

Figure 5.37 shows a few things. First, the improved resolution afforded by a planar array is significant, even with conventional processing as seen by a comparison of the bottom line (single subarray) of the top two plots. Since the single-subarray configuration corresponds to CMFP, one may see that the benefits obtained by averaging many snapshots using a single line is poorer than using fewer snapshots but having the resolution of the larger array.

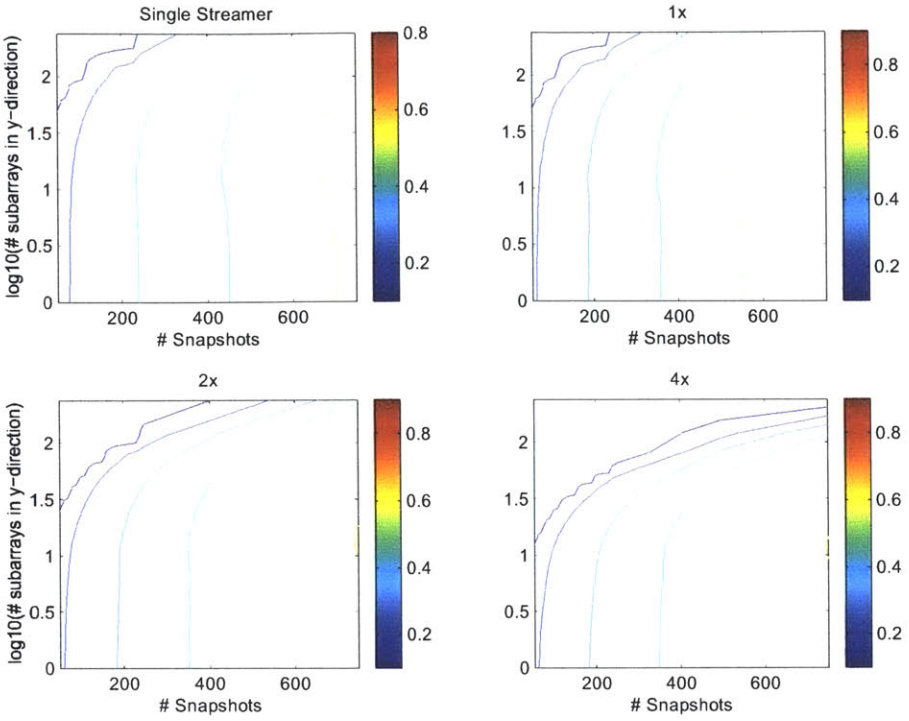

Figure 5-37: Pd vs snapshots for different subarray configurations, CTA algorithm.

Given that even CMFP resolution of a 4-streamer array outperforms the single line array significantly in snapshot-limited environments, it is useful to examine adaptive configurations. Using the CTA algorithm, the adaptive DOFs for the single line and multi-line 1x configuration are identical. Therefore, the performance of the multi-line will always be better since snapshot support is identical.

Now look at the performance comparison of the 1x, 2x, and 4x configurations. Clearly the 4x configuration has the largest trade-off between adaptivity and snapshot support since this configuration has the highest number of subarrays. Except in the very low subarray configurations, the 4x configuration is outperformed by the 1x and 2x configurations, both of which perform similarly. This tells us that with this array geometry, the resolution gained by performing adaptive processing across the subarrays is not enough to compensate for the reduced snapshot support.

Figure 5.38 shows the same plots for the ATC algorithm. In these plots, it is evident that the resolution gained from adaptively processing subarrays containing

elements from each streamer (1x configuration) does not overcome the added snapshot support required, this leading to slightly better performance from the 4x configuration. It should be noted, however, that for this configuration and the ATC algorithm, the performance of a planar array does not significantly improve upon that of a single line array.

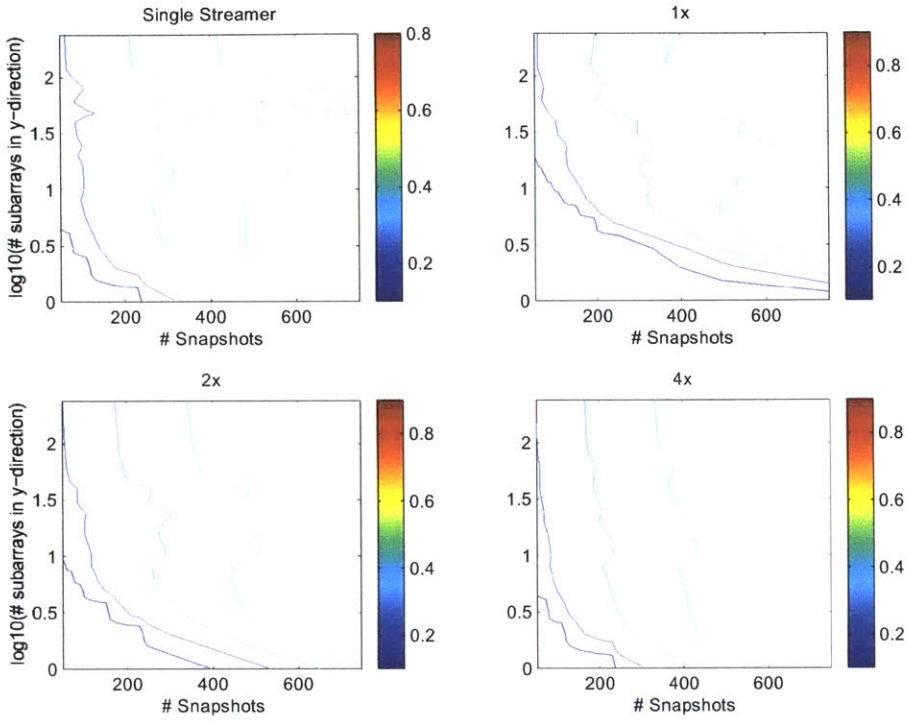

Figure 5-38: Pd vs snapshots for different subarray configurations, CTA algorithm.

This leads to an important insight into array configurations. Recall that the inter-streamer spacing was chosen to mitigate left/right ambiguities, and was designed with a plane-wave propagation model in mind. Recall also that mode sampling leads to range and depth resolution for an array using MFP. Therefore, if an array is designed so as to better sample the modal structure of the propagating field, resolution and hence detection performance should improve. Figure 5.39 shows the performance of the CTA and ATC algorithms for a single line, a 1x and a 4x configuration with an array with inter-streamer spacing set to 25m instead of 6.25. This increases the array aperture and the mode sampling. In this example, the target coherence length is 2500

elements and the interferer coherence length is 20 elements. Clearly the planar array configurations outperform the single line array.

This plot demonstrates a very important point to array design for MFP. The 4x configurations in the CTA algorithm and the 1x configurations in the ATC algorithm both, for a fixed number of subarrays in the y-direction, contain a higher dimensionality at the adaptive stage. Therefore at very low snapshot support, these two algorithms will fail. The important point, however, is that at higher subarray configurations, and moderate snapshot support these configurations are optimum. The reason for this is that for the 4x CTA and the 1x ATC the adaptivity is applied across streamers. It is sampling across streamers which leads to mode sampling of a broadside target, and this larger inter-streamer spacing leads to better mode sampling. The result is greater nulling of interferers and hence better detection performance.

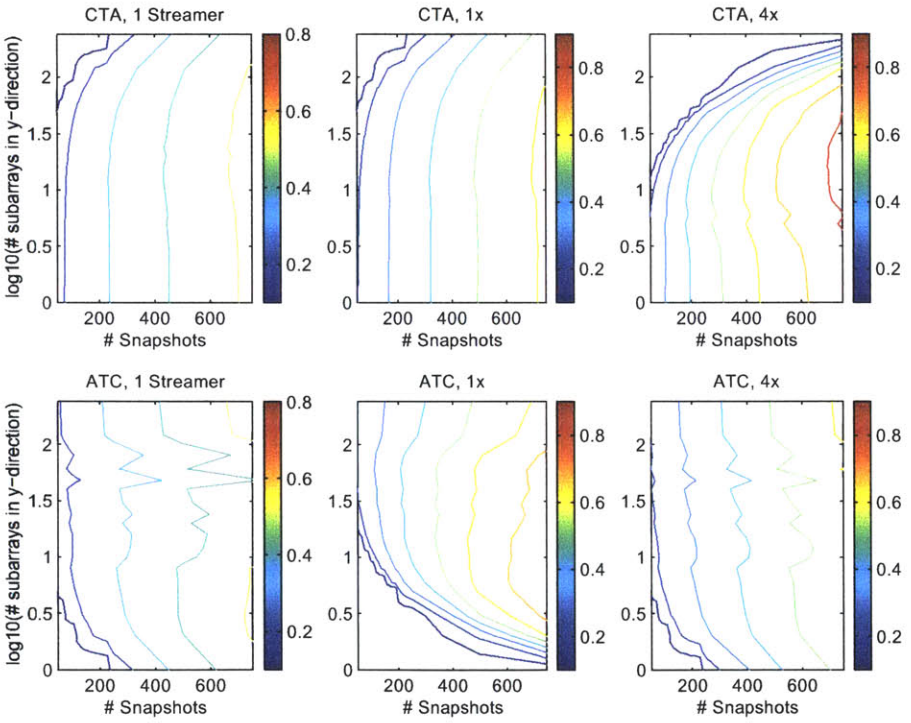

Figure 5-39: Pd vs subarrays and snapshots for a 4-line array at 25m inter-streamer spacing.

The study of planar arrays and MFP has lead to several insights.

1. CMFP range, bearing, and depth resolution of planar arrays leads to better

detection performance than that of a single line.

2. Stronger detection performance is attained when the streamers are separated by more than the standard quarter-wavelength spacing from plane wave design. Larger spacing leads to better modal sampling which in turn leads to better resolution of broadside targets.

3. Adaptive processing should be applied across streamers in order to exploit the mode-sampling resolution for a broadside target. This corresponds to a 4x configuration of the CTA algorithm and a 1x configuration for the ATC algorithm.

This analysis concludes the MFP portion of this thesis. The following section examines the performance of combined subarray-space and beam-space adaptive processing in the context of the CTA algorithm.

5.4 Comparison to Beam-space Processing

This thesis has developed an analytical model for a performance analysis of subarray processing algorithms which includes the effects of finite snapshot support and coherence loss. The model has then been used to gain insight into optimal subarray partitioning and algorithm selection. The CTA and ATC showed the best performance and, in most cases, the CTA outperformed the ATC algorithm. At this time, the subarray processing will be compared to the commonly-used beam-space adaptive algorithm [9].

Beam-space adaptive processing is very similar to the CTA algorithm. In the CTA algorithm, a transformation matrix whose columns are the conventional weight vectors is used to transform element-level data to subarray-level data. Beam-space processing works in exactly the same way. The transformation, however, is from the element-level data to full-array beam data. Therefore the columns of the element-to-beam transformation matrix are the full-array steering vectors for various look-directions. The second stage of both algorithms is then MVDR.

The beam-space algorithm essentially takes the same approach to interference rejection as the CTA algorithm. The resolution of the full array is preserved through first stage, but distant interferers are nulled using a conventional pattern. The second stage then is left to reject nearby interference which is passed through the different steering directions chosen for the beams.

Typically with beam-space processing, beams are chosen to be equally-spaced in wavenumber-space (i.e. cosine space), and centered on the hypothesized target bearing. A subarray variation of this algorithm appeared in a paper by Cox [ref] in which he took this approach to achieve MFP-like performance using plane-wave models and subarrays. This section studies the subarray-space/beam-space adaptive algorithm performance in a coherence-limited snapshot-starved environment using a plane wave model.

The subarray-space/beam-space algorithm will be denoted by CTAB for notational purposed. Recall from section 3.5.1 the algorithm formed a transformation matrix A (equation 3.19). This matrix had dimension NxM where N is the number of sensors and M is the number of subarrays. The CTAB algorithm forms exactly the same sort of matrix, lets call it A_b, which is of dimension Nx(MB) where again N is the number of sensors, M is the number of subarrays, and B is the number of beams. A_b is therefore a block diagonal matrix, each block of which steers a given subarray toward B different directions. Note that the new dimensionality of the adaptive stage has increased by a factor of B. This impacts the statistics and requisite snapshot support.

Recall that the statistics of the CTA algorithm were derived exactly since the first stage was just a linear transformation of complex Gaussian data. The CTAB algorithm is no different. Therefore, the statistics of the CTAB algorithm are identical to those of the CTA algorithm with the matrix A_b substituted for the matrix A in the asymptotic power computation (equations 3.20-3.23) and the resulting dimensionality of the adaptive stage increases from M to MB in equation 4.88.

This analysis will focus on the interference-dominated field described above. A single streamer is used, the signal coherence is 2500 elements, and the interferer

coherence is 50 elements. Figure 5.40 shows the detection performance of the CTA algorithm and the CTAB algorithm with 3, 5, and 7 beams, all as a function of snapshot support and number of subarrays. The single subarray configuration for the CTAB algorithms corresponds to the typically-used beam-space adaptive processing.

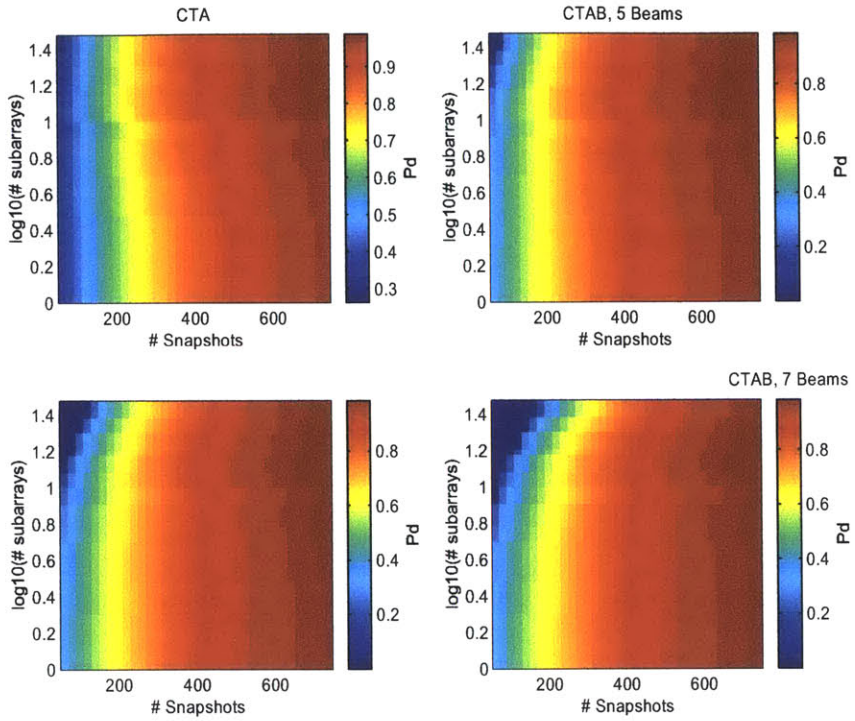

Figure 5-40: Pd vs subarrays and snapshots for CTA and CTAB algorithms.

The most obvious difference between the plots is the performance at the top left of the plots. This corresponds to low snapshot support and high numbers of subarrays. As the number of beams increases, the requisite snapshot support increases, leading to poor performance in low-snapshot regions.

The trade-off in the CTAB algorithm is between first-stage nulling and adaptive DOF. The CTAB algorithm prevents sources within B/2 subarray beamwidths of the hypothesized target direction from being nulled at the first stage. When the subarrays are very large (i.e. few subarrays) this beamwidth is very small, and the spatial filter of the first stage drops off quickly away from the hypothesized target direction. The intent of this algorithm is to remove all "out of beam" interference

conventionally relying on the resolution and low sidelobes of a large subarray. This also passes nearby sources so that at the adaptive stage, they are more likely to be the strongest sources. The adaptive stage therefore nulls the nearby interference. There is a trade-off, however, between the number of beams and the snapshot support. The CTA algorithm works in approximately the same way, but the subarray patterns determine the "width" of the main-lobe, and hence how much attenuation is given to interferers near the main beam. The question remains as to what the peak is of the trade-off.

In the AO environment used in the previous sections, and the CTAB implementations shown in figure 5.37, the CTAB algorithm operates best as a full-array beam-space adaptive processor, i.e. a single subarray configuration. The increase in the dimensionality of the adaptive processing does not outweigh the resolution and snapshot support achieved through the full-array beam-space processing in all cases shown here (i.e. 3, 5, and 7 beams').

The CTA algorithm has an optimum subarray configuration of 16 subarrays for this example. As seen in Figure 5.41, the CTA algorithm with this configuration outperforms the CTAB algorithms in all except the very low snapshot region. Overall the performance is comparable, but the CTA without beam-space outperforms the CTAB algorithm in most regions. In an interference-rich environment, there must be enough adaptive DOFs to mitigate interference. The CTAB algorithm performed best with a single subarray, leaving the number of adaptive DOF equal to the number of beams. If substantial interference leaks through the first stage, more adaptivity is needed. That is provided by the CTA algorithm with the optimal number of subarrays.

At this point several conclusions may be drawn as to the relative performance of the algorithms:

1. In an interference-dominated environment, the CTAB algorithm performs best with a single subarray configuration because the full-array resolution is needed to mitigate out-of-beam interference while maintaining a low requisite snapshot support.

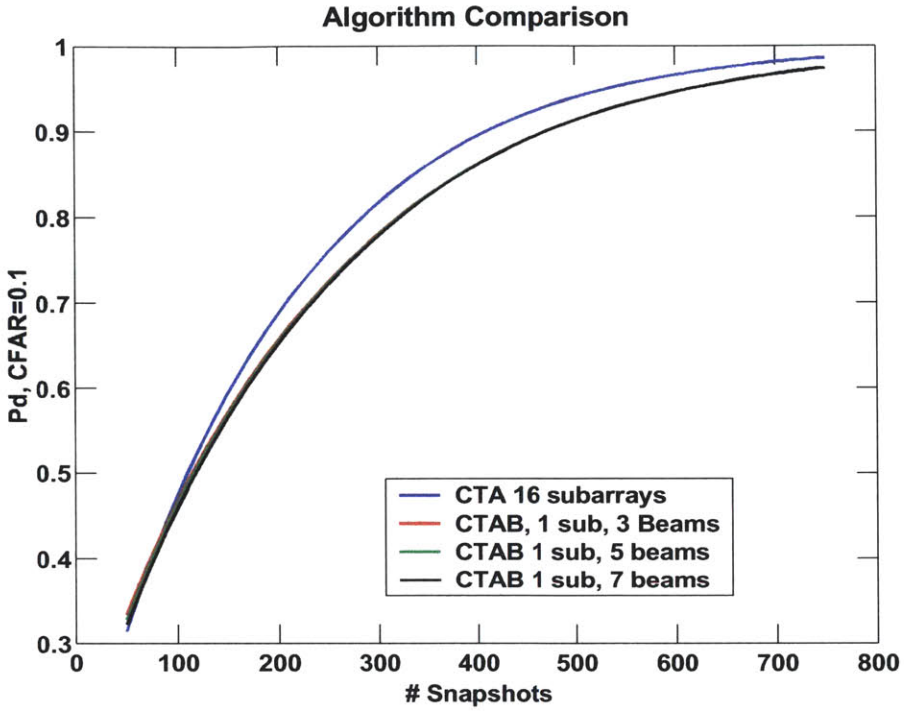

Figure 5-41: Pd vs snapshots for CTA and CTAB algorithms, optimum configurations.

2. The CTA algorithm trades CBF resolution for adaptive DOF more efficiently than the CTAB algorithm, leading to better overall-performance except in extremely-low snapshot scenarios when the detection performance is poor in either case.

This section has presented one comparison between subarray algorithm performance and other commonly-used algorithms. The CTAB algorithm was chosen for comparison because the algorithm lent itself easily to the statistical analysis developed in this thesis. Next, final chapter of this thesis will now provide a summary of the contributions of this work as well as provide an outline for future work and applications of the analysis provided here.

5.5 Partitioning Guidelines

This chapter has shown the relative performance of these subarray algorithms in a variety of interference environments. The scenario of greatest interest in this thesis is the case in which there is a significant density of discrete interference which has decorrelated more than a single target of interest. In this interference dominated environment, the balance between adaptivity needed to suppress the interference and the available snapshots drives teh subarray selection process far more than the coherence issues. The coherence, however, does impact the subarray selection in that it spreads the dimensionality of the interference, changing the number of adaptive degrees of freedom required to suppress it as well as spread the signal spectrum leading to signal gain degradation, and a need for greater suppression of interference. The coherence effects, however, are secondary to snapshot considerations in subarray selection.

A general guideline for subarray partitioning strategy is to choose subarrays such that the resulting number of adaptive degrees of freedom is the minimum of the rank of the interference or 1/2-1/3 of the snapshot support available.

Chapter 6

Summary and Future Work

This thesis has provided a comprehensive performance analysis of several subarray processing algorithms for detection of quiet targets in a littoral ocean environment. Further, the effects of spatial coherence and snapshot support have been studied in the context of multi-stage adaptive algorithms. Finally these principles have been applied to the use of large-aperture planar arrays and Matched Field Processing for the first time.

6.1 Summary and Contributions

The contribution of this thesis is the work presented in Chapters 4 and 5. First, this thesis developed an analytical model to assess the statistical detection performance of three adaptive subarray algorithms as well as the optimum processor. Second this these models were used to study the effects of limited coherence and snapshot support on subarray partitions and algorithm selection.

The statistical models developed in this thesis incorporated the performance-degrading effects of both limited snapshot support and limited spatial coherence for the first time, both of which impact realistic performance of large aperture arrays. This theory leveraged strongly off of the work of Capon and Goodman as well as the work of Steindhardt and that of Richmond. This is the first such statistical performance analysis of subaperture processing designed to mitigate the effects of spatial

coherence and snapshot support.

The statistics of the optimum processor were derived exactly when the signal was coherent and the interference experienced spatial decorrelation. When the signal decorrelated, however, this led to a more complicated expression for the pdf of the likelihood ratio statistic. In this case an approximation was made that the signal was spread equally over an appropriate number of eigenvalues, leading to an approximation of the detection statistic as a complex chi-squared random variable with an effective number of degrees of freedom.

In the case of the CTA algorithm, exact detection statistics were provided. By using the assumption that data snapshots were independent complex Gaussian random vectors, the data covariance had a complex Wishart distribution. Since the first stage of the processor used conventional processing, the data after the first stage remained Gaussian with a complex Wishart-distributed sample covariance matrix. The work of Capon and Goodman was then applied to the adaptive processing at the second stage leading to a detection statistic with a complex chi-squared distribution.

The ATC and AI algorithm statistics were complicated by the non-Gaussianity of the data after the adaptive stage. The detection statistic of the AI algorithm was a sum of correlated complex chi-squared random variable with unknown covariance. The approximation was then taken to approximate the sum as a chi-squared random variable with an effective number of degrees of freedom. A method for determining the degrees of freedom was presented. This examined the degrees of freedom in the clairvoyant covariance matrix which proved to have much better comparison to simulations than an "independent subarray" approximation.

The ATC algorithm statistics proved to be the most difficult to derive. First, the approach was taken to derive the first and second order statistics of a 2-subarray configuration and implementing the Central Limit Theorem. After significant analysis, an independence approximation was made for the two subarrays. While this approximation led to adequate results in a low-energy coherence case, it failed in the interference-dominated environment of interest to this thesis. An alternative approach was taken which again leveraged off of the work of Capon and Goodman. The

first and second moments of the subarray power estimate were computed using the clairvoyant subarray power estimates and the bias and variance expressions based on the snapshot support relative to the subarray size. This approach led to adequate agreement with simulations for the purposed of this thesis.

These analytical models were then used to determine the effects of interference and target signal decorrelation and provide guidelines for appropriate subarray partitioning strategy and algorithm selection. A performance metric of a constant false alarm rate detection probability was used.

It was shown first using the optimum processor (which removed the effects of covariance matrix estimation) that interference and source decorrelation affect detection performance in different ways. As an interferer decorrelates, it gains a broader wavenumber spectrum, or alternatively a larger interference subspace. This results in the need for greater adaptivity to mitigate the interference. When the interference has decorrelated such that its wavenumber spectrum is flat over the region of the target signal's spectrum, detection performance improves. Target decorrelation also leads to a spreading of the target signal, and hence, less of the target power in the direction of the steering vector, and hence poor detection performance.

The performance of the CTA, AI, and ATC algorithms were then studied in a variety of interference environments for non-overlapping subarray configurations. The scenarios were assumed to be stationary over the observation intervals in all examples. It was shown that there is an inherent trade-off between the snapshot support and the adaptive degrees of freedom in the algorithm. The adaptive DOF, (subarray configuration) should be chosen as large as possible until the biases and variances caused by the covariance matrix estimation become too large.

It was shown that the CTA algorithm outperforms the ATC algorithm in scenarios of interest since the CTA algorithm mitigates spatially distant interference at the first, non-adaptive stage, leaving the adaptive stage to null in-beam interferers with the full array aperture resolution. The ATC algorithm uses adaptivity less efficiently, and often is unable to null nearby interference. The choice of subaperture partitioning strategy depends heavily on the interference environment, and may be

easily computed using the analysis tools developed in Chapter 4.

The main contributions of this work are summarized below:

1. Developed a statistical analysis method which includes the effects of finite snapshot support and finite coherence effects of both a target and interference field for the optimum processor and the CTA, ATC and AI algorithms. This analysis was also extended to the CTAB algorithm for completeness.

2. The CTA algorithm outperforms the ATC and AI algorithms because it has a more efficient use of adaptivity. Each adaptive stage attempts to reject the loudest interference. The CTA algorithm mitigates the out-of-beam interference with conventional processing and has the full array aperture to null residual (mostly near-beam) interference at the adaptive stage. The ATC algorithm applies adaptivity over a smaller (subarray) aperture. It sometimes nulls spatially-distant interference which would otherwise be mitigated by the conventional stage. It also lacks the resolution to easily null spatially-proximate interference leading to high white noise gain.

3. Subarray algorithms applied to MFP behave in exactly the same manner. The performance of the ATC algorithm suffers more in the MFP environment because of the high sidelobes inherent in MFP. The ATC algorithm also suffers more from fading across the array leading to far worse performance in scenarios with targets off broadside and planar arrays.

4. Planar arrays drastically improve detection performance of broadside targets when MFP is used and the spatial separation between streamers is adequate for mode sampling. In that case, adaptivity should be applied across streamers in order to best exploit mode sampling resolution.

5. CTA algorithm performance in a coherence-limited, snapshot-starved environment is slightly better than full-array beam-space processing, and significantly better than subarray-space beam-space processing (CTAB). The CTA algo-

rithm provides a better trade-off between resolution, adaptivity, and snapshot support.

6.2 Future Work

This thesis has focused on a hybrid class of subarray algorithms, pieces of which are known to have analytically-derivable statistical properties. Recent work in adaptive array processing has advanced the commonly used algorithms beyond this limited class. The conclusions drawn here in this thesis have been based on full-rank SCMs and classical approaches to processing. In practice, several of the *ad hoc* methods such as diagonal loading, Dominant Mode Rejection, and Principle Components methods are commonly used. A further study of the application of more ad hoc algorithms to subarray processing could lead to performance enhancement. For example, the CTA algorithm may be used with diagonal loading or DMR at the adaptive stage. It may be possible to estimate the detection statistics of these algorithms using the same sort of degree-of-freedom approximations used here. This is an area with great potential for future work.

This thesis has also limited the structure of the subarrays to be non-overlapping and equal in size. The statistics of the AI and ATC algorithms have been derived using approximations for the coherence between subarrays, a more in-depth examination of these approximations is necessary if one were to incorporate overlapping subarray partitions. Overlapping subarrays, however, would reduce the problem of grating lobes in the ATC algorithm. It would not change the problem of limited array resolution, but it would prevent under-nulled interference from leaking through grating lobes of the conventional stage. This is another area for potential performance improvement.

One potential performance degradation mechanism to any sort of adaptive processing, particularly MFP is mismatch between the assumed steering vector and the true steering vector. Any mismatch can lead to target self-nulling and a resulting degradation in detection performance. It is important to assess the impact of these

phenomena as they apply to the performance of more practically used ad hoc algorithms.

The work presented here had the goal of providing an analysis tool which is used to provide insight to array design in the presence of snapshot support limited and coherence limited environments which are particularly problematic for large towed arrays. This thesis has begun with a simple model which ignored several other performance degradation mechanisms such as environmental mismatch, poor array element localization, and target motion among others. This work presents a framework which could be expanded to include such effects for future work.

Bibliography

[1] R. J. Urick. *Principles of Underwater Sound.* McGraw Hill, 1983.

[2] W. M. Carey. The determination of signal coherence length based on signal coherence and gain measurements in deep and shallow water. *J. of the Acoust. Soc. of Am.*, 104(2):831–837, 1998.

[3] H. Cox. Line array performance when the signal coherence is spatially dependent. *J. of the Acoust. Soc. of Am.*, 54(6):1743–1746, 1973.

[4] D. R. Morgan and T. M. Smith. Coherence effects on the detection performance of quadratic array processors with applications to large-array matched-field beamforming. *J. of the Acoust. Soc. of Am.*, 87(2):737–747, 1990.

[5] W. M. Carey, P.G. Cable, W. L. Siegmann, J. F. Lynch, and I. Rozenfeld. Measurement of sound transmission and signal gain in the complex straight of korea. *IEEE Journal of Oceanic Eng.*, 27(4):841–852, 2002.

[6] S. Haykin and A. Steinhardt. *Adaptive Radar Detection and Estimation.* John Wiley and Sons, 1992.

[7] J. Capon and N. Goodman. Probability distributions for estimators of the frequency-wavenumber spectrum. *Proc. IEEE*, 34:1785–1786, 1970.

[8] R. T. Lacoss and G. T. Kuster. Processing a partially coherent large seismic array for discrimination. Technical Report MIT-LIN-TN-1970-30, MIT Lincoln Laboratory, Lexington, MA, 1970.

[9] H. Cox, R. Zeskind, and M. Myers. A subarray approach to matched field processing. *J. of Acoust. Soc. of Am.*, 87(1):168–178, 1990.

[10] Y. P. Lee, H. Freese, J. Hanna, and P. Mikhalevsky. Adaptive matched field processing of a large array in a white noise environment. In *Proc. Oceans '93*, volume 3, pages 75–80, 1993.

[11] M. Hinich and W. Rule. Bearing estimation using a large towed array. *J. of the Acoust. Soc. Am.*, 58(5):1023–1029, 1975.

[12] J. Nuttall. Adaptive adaptive narrowband subarray beamforming. Technical Memorandum TM 941015, Naval Undersea Warfare Center, New London, CT, 1994.

[13] H. W. Briscoe and P.L. Flock. Data recording and processing for the experimental large aperture seismic array. *Proc. of the IEEE*, 53:1852–1859, 1965.

[14] J. Capon, R. J. Greenfield, and R. T. Lacoss. Long period signal processing results for large aperture seismic array. Technical Report 1967-50, MIT Lincoln Laboratory, Lexington, MA, 1967.

[15] J. Wang, H. Israelson, and R.G. North. Optimum subarray configuration using genetic algorithms. *Proc. of the ICASSP*, 4:2129–2132, 1998.

[16] A. B. Baggeroer and H. Cox. Passive sonar limits upon nulling multiple moving ships with large aperture arrays. *Conference Record of the* 33^{rd} *Asilomar Conference on Signals, Systems, and Computing*, pages 103–105, 1999.

[17] S. Tantum and L. Nolte. On array design for matched-field processing. *J. of Acoust. Soc. of Am.*, 107(4):2101–2111, 2000.

[18] E. J. Kelly and K. M. Forsythe. Adaptive detection and parameter estimation for multidimensional signal models. Technical Report 848, MIT Lincoln Laboratory, Lexington, MA, 1989.

[19] A. Steinhardt. The pdf of adaptive beamforming weights. *IEEE Trans. on Signal Processing*, 39(5):1232–1235, 1991.

[20] C. D. Richmond. Pdfs, confidence regions, and relevant statistics for a class of sample covariance-based array processors. *IEEE Trans. on Signal Processing*, 44(7):1779–1793, 1996.

[21] Western geophysical web site. www.westerngeco.com.

[22] Petroleum geo-services web site. www.pgs.com.

[23] Cgg web site. www.cgg.com.

[24] L. J. Ziomek. *Underwater Acoustics: a linear systems theory approach.* Academic Press, 1985.

[25] J. Sutton. Underwater acoustic imaging. *Proc. of the IEEE*, 67(4):554–566, 1979.

[26] A. B. Baggeroer, W. A. Kuperman, and H. Schmidt. Matched field processing: source localization in correlated noise as an optimum parameter estimation problem. *J. of the Acoust. Soc. of Am.*, 83(2):571–587, 1988.

[27] F. B. Jensen, W. A. Kuperman, M. B. Porter, and H. Schmidt. *Computational Ocean Acoustics.* AIP Press, 2000.

[28] A. B. Baggeroer, W. A. Kuperman, and P. N. Mikhalevsky. An overview of matched field methods in ocean acoustics. *IEEE Journal of Oceanic Engineering*, 18(4):401–424, 1993.

[29] L. M. Zurk, N. Lee, and J. Ward. Source motion mitigation for adaptive matched field processing. *J. of the Acoust. Soc. of Am.*, 113(5):2719–2731, 2003.

[30] L. M. Zurk, B. Tracey, and J. A. Munro. Signal degradation mechanisms for passive localization of acoustic sources in shallow water. In *PIERS 2002*, 2002.

[31] D. Johnson and D. Dudgeon. *Array Signal Processing.* Prentice Hall, 1993.

[32] H. Cox. Resolving power and sensitivity to mismatch of optimum array processors. *J. of Acoust. Soc. of Am.*, 54(3):771–785, 1973.

[33] W. M. Carey and W. B. Moseley. Space-time processing, environmental-acoustic effects. *IEEE Journal of Oceanic Engineering*, 16(3):285–301, 1991.

[34] W. A. Kuperman and F. Ingenito. Spatial correlation of surface generated noise in a stratified ocean. *Journ. of the Acoust. Soc. of Am.*, 67:1988–1996, 1980.

[35] H. VanTrees. *Detection, Estimation, and Modulation Theory Part I.* John Wiley and Sons, 2001.

[36] H. VanTrees. *Detection, Estimation, and Modulation Theory Part IV: Optimum Array Processing.* John Wiley and Sons, 2002.

[37] B. D. VanVeen. Minimum variance beamforming with soft response constraints. *IEEE Trans. on Signal Processing*, 39(9):1964–1972, 1991.

[38] H. Cox, R. M. Zeskind, and M. M. Owen. Robust adaptive beamforming. *IEEE Trans. on Acoustics, Speech, and Signal Processing*, 35(10):1365–1375, 1987.

[39] B. D. Carlson. Covariance matrix estimation errors and diagonal loading in adaptive arrays. *IEEE Trans. on Aerospace and Electronic Systems*, 24(4):397–401, 1988.

[40] H. Cox and R. Pitre. Robust dmr and multi-rate adaptive beamforming. *Conference Record of the* 31^{st} *Asilomar Conference on Signals, Systems, and Computing*, pages 920–924, 1997.

[41] H. Cox, R. Pitre, and H. Lai. Robust adaptive matched field processing. *Conference Record of the* 32^{nd} *Asilomar Conference on Signals, Systems, and Computing*, pages 127–131, 1998.

[42] N. R. Goodman. Statistical analysis based on a certain multivariate complex gaussian distribution. *Ann. Math. Stat.*, 34:152–177, 1963.

[43] S. Haykin, J. H. Justice, N. L. Owsley, J. L. Yen, and A. C. Yak. *Array Signal Processing.* Prentice-Hall, 1985.

[44] A. B. Baggeroer. Confidence interval determination for spectral estimates using 'tilted densities'. *IEEE Conference on Acoust., Speech, and Sig. Proc.*, page 1454 1457, 1983.

[45] H. VanTrees. *Detection, Estimation, and Modulation Theory Part III.* John Wiley and Sons, 2001.

[46] James Preisig. Personal Communication.

[47] R. Oba and S. Finette. Acoustic propagation through anisotropic internal wave fields: Transmission loss, cross-range coherence, and horizontal refraction. *J. of the Acoust. Soc. of Am.*, 111(2):769–784, 2002.

[48] Chair J. Zittel and Acoustic Observatory Working Group. Phase IIA final Report Presentation, Feb. 2001.